TECHNISCHE UNIVERSITÄT MÜNCHEN

Physik-Department
Fachgebiet Physik weicher Materie

Cononsolvency of PNIPAM in water/alcohol mixtures - A neutron scattering study

Konstantinos Kyriakos

Vollständiger Abdruck der von der Fakultät für Physik der Technischen Universität München zur Erlangung des akademischen Grades eines

Doktors der Naturwissenschaften (Dr. rer. nat.)

genehmigten Dissertation.

Vorsitzender:	Univ.-Prof. Dr. Martin Zacharias
Prüfer der Dissertation:	1. Univ.-Prof. Christine M. Papadakis, Ph.D.
	2. Univ.-Prof. Dr. Peter Böni

Die Dissertation wurde am 25.02.2015 bei der Technischen Universität München eingereicht und durch die Fakultät für Physik am 20.04.2015 angenommen.

Abstract

Thermoresponsive polymers are possible cornerstones for designing numerous smart materials with applications in a wide range of disciplines. In this dissertation the focus is on the properties of the thermoresponsive poly(N-isopropyl acrylamide), in homopolymers and amphiphilic block copolymers, in solutions of mixed solvents of water and a short chain alcohol (e.g. methanol). By means of time-resolved small angle neutron scattering (TR-SANS) we study the micellar structure and follow the aggregation triggered by the phase transition, at a mesoscopic length scale, by two different pathways. We observe a strong influence of the solvation environment on the the aggregation kinetics and use different models to quantify the findings. By means of quasi-elastic neutron scattering (QENS) we focus on the local polymer-solvent and solvent-solvent interactions and reveal the solvation mechanism at the molecular level. In the appendix of this work some results on the novel thermoresponsive polymer poly(methoxy diethylene glycol) are presented.

Zusammenfassung

Thermoresponsive Polymere sind intelligente Materialien, die als Eckpfeiler in zahlreichen Anwendungen verwendet werden können. Ziel dieser Arbeit ist es, die Eigenschaften von Poly(N-isopropyl acrylamide) und darauf basierenden Blockcopolymeren in gemischten Lösungsmitteln aus Wasser und Alkoholen (z.B. Methanol) zu untersuchen. Mit zeitaufgelöster Neutronenkleinwinkelstreuung (TR-SANS) klären wir den Einfluss des Lösungsmittels auf die sich bildenden Mizellen und auf deren Aggregation, die oberhalb des Phasenüberganges stattfindet. Die Aggregation wird mit Hilfe von theoretischen Modellen beschrieben. Dieses Teil der Arbeit konzentriert sich auf die mesoskopische Skala. Mit temperaturaufgelöster quasielastischer Neutronenstreuung (QENS) untersuchen wir die Wechselwirkungen zwischen allen den Komponenten der Lösung unter einander. Die Methode gibt Aufschluss über die Diffusion der Lösungsmittelmolekulen und den Lösungsprocess. Der Fokus liegt hierher auf der molekularen Längenskala. Im Anhang werden Ergebnisse für das neuartige Polymer Poly(methoxy diethylene glycol) präsentiert.

ἕν οἶδα ὅτι οὐδέν οἶδα*

* one thing I know, that I know nothing (Socrates 470/469 – 399 BC)

Contents

1. Introduction

Soft matter has emerged over the last two decades as a new, promising area in the field of materials science. Looking for a definition, as to which type of materials can be classified under the title "soft matter", we can quote P. G. de Gennes (Nobel prize in Physics 1991): "All physicochemical systems that have large response functions". In other words, any material that exhibits a big response to a mild external trigger or influence, is part of the soft matter family. Attempting a more specific definition, we can refer to the mechanical properties. Soft matter is expected to exhibit both viscous and elastic properties, depending on the time scale over which an external stress is applied (e.g. silly putty). After these definitions, a very wide variety of materials meet the specifications. Indeed, the basic sub-families of the soft matter class are the following: colloids (e.g. foams, paints, aerogels), polymers (e.g. polyelectrolytes, polymer brushes, thermoresponsive polymers), liquid crystals, surfactants (e.g. emulsifiers, lubricants) and several biological systems (e.g. membranes, proteins, DNA, blood). From this classification, it is easily seen that the soft matter physics discipline, which is the core of the work presented here, covers not only many different systems but also a huge range of length and time scales. Therefore, the study of soft matter requires an interdisciplinary effort [Jon02, Ham07]. The spark that ignites the interest of the scientific community on this field is the numerous applications of this class of materials.

This work emphasizes on the study of polymers and in more detail on the behaviour of thermoresponsive polymers in aqueous solutions. These materials are a special category of the soft matter, that change abruptly and significantly their properties as a response to small changes of the temperature. This unique property has been already the cornerstone for many aplications in several fields [NNH$^+$07, BAR09, CSHG$^+$10, GZ11, LHS$^+$12]. As a consequence of their importance for designing applications, the deep understanding of their physical behaviour is of high interest. Among these materials, poly(N isopropyl acrylamide) has a prominent place. It consists one of the most well known and thoroughly studied thermoresponsive systems currently available. In spite of its significance, still some aspects, mainly concerning its hydration mechanism, are under vivid debate in literature. Hence, it offers a prolific field for new studies.

The present work focuses not exclusively on the thermoresponsive character of the

polymer, but also on the influence of the solvation environment on its properties and responsivity. It has been shown in many studies that the solvation environment affects the properties of the system and the origin of this influence still remains an open question [SSB+14]. By studying the behaviour of PNIPAM in a complex solvation environment, we aim to shed light on the local interactions that characterize the system at a molecular level, and also to link them with the behaviour of the system at larger length scales. Therefore we perform two different kinds of experiments. In the first two parts of this work, we emphasize on the aggregation kinetics that characterize the association of thermoresponsive particles in mixed solvents by means of time-resolved small-anlge neutron scattering. In the schematic phase diagram presented in Fig. 1.1 the two different approaches are presented. In the first experiment, an alcohol (i.e. methanol) is added rapidly to an aqueous solution of PNIPAM-based block copolymer and the growth of aggregates is followed. In the second experiment, a different path is followed, i.e. the polymer is pre-dissolved in mixed solvents of water and alcohols, and the phase separation is triggered by the rapid increase of the temperature. Both experiments aim to study the influence of the alcohols on the aggregation kinetics, i.e. at a mesoscopic length scale. In the last part of the thesis, a study of the diffusion dynamics of the solvation species in a ternary mixture PNIPAM/water/methanol is presented. The aim of this part will be to elucidate the local interactions that govern the behaviour of the system, i.e. at the molecular level. By means of quasielastic neutron scattering, we probe the dynamics of the solvating species and clarify the types of interactions that take place.

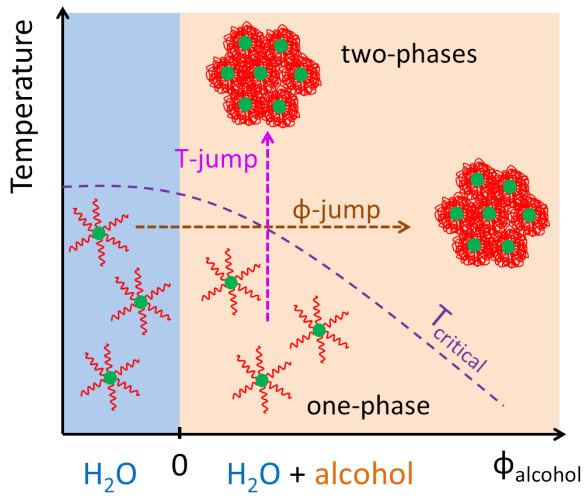

Figure 1.1.: Schematic representation of the experiments aiming to study the aggregation kinetics of micellar solutions of PNIPAM-*b*-PS amphiphilic block copolymers, by alcohol volume fraction jumps and temperature jumps.

2. Background

2.1. Polymers

The word polymer originates from the combination of two greek words: πολύ (=many) and μέρος (=part). Thus, by etymology, as polymer we define a substance that consists of many small, building blocks. These blocks are the monomers and are covalently bound, through various polymerization processes, to create macromolecules (e.g. polymer chains). The chemical properties of the monomers define at a significant degree the ones of the polymers. Fig. 2.1 shows the monomer ethylene glycol and the resulting polymer poly(ethylene glycol) (PEG).

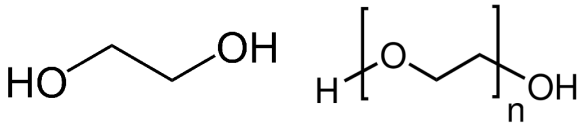

Figure 2.1.: Ethylene glycol and polyethylene glycol.

The number of ethylene glycol molecules that participate in the formation of the polymer is called degree of polymerization. In Figure 2.1 the polymerization number is presented by n and it can also be represented as N. The molar mass of a polymer chain is then given as the product of N and the molar mass of the monomer M_{mono}

$$M_{poly} = N \cdot M_{mono}. \tag{2.1}$$

As a consequence of the polymerization process, all synthetic polymers are polydisperse; they consist of chains of various lengths. In contrast, natural polymers (e.g. DNA) are rather monodisperse. The polydispersity of the polymers is regarded as a vital characteristic and affects strongly many of their properties. To account for this, the polydispersity index PDI (or σ) is introduced and is defined through the different molar mass averages of a polymer. Due to the statistical character of the molecular weight (M_w), we refer to the mean M_w of a polymer. Different approaches are possible. The simplest one is the number average molecular weight M_n defined as

$$M_w = \sum_i n_i \cdot M_i \tag{2.2}$$

where n_i is the number of macromolecules with a molecular weight M_i. M_n can be determined by measurements of the osmotic pressure or any other colligative properties [Ged01, RC03]. The weight average molecular weight M_w on the other hand is given by

$$M_n = \frac{\sum_i n_i \cdot {M_i}^2}{M_i}. \tag{2.3}$$

M_w is experimentally accessible via measurements of sedimentation equilibria and via scattering techniques (i.e. light, x-ray, neutron) [Ged01, RC03]. The polydispersity index can now be expressed as

$$PDI = \frac{M_w}{M_n}. \tag{2.4}$$

In simple words, the PDI expresses the width of the distribution of the molecular weights around the mean value. For monodisperse systems PDI = 1. Values of 1.1 - 1.2 are typically obtained.

In the simplest case, a polymer chain consists of monomers of one type only, resulting in a homopolymer (e.g. PEG). In the case that more than one types of monomers are present in a polymer chain, we speak about copolymers. The copolymers combine the properties of the different monomers into the new macromolecule. Even in the simplest case, when two monomers A and B are combined, a vast range of accessible structures is obtained. Figure 2.2 shows the most important copolymer structures. This work focuses on block copolymers, where the two monomers A and B create first blocks of homopolymer units and then they are covalently bound to create the final macromolecule. In most of the cases the homopolymer units are two or three, thus we have diblock or triblock copolymers, respectively. Star copolymers have also attracted recently the attention of the scientific community due to their unique topology. Under a general scope, the unique ability of these systems to combine properties of the two (or more) components highlights them as extremely important for various modern applications (e.g. templates for nanostructuring, drug delivery systems, smart surfaces and many others).

2.2. Polymers in solution

The behaviour of a polymer in the presence of a solvent has been described by the Flory-Huggins theory, developed independently by Flory [Flo42] and Huggins [Hug42] in the

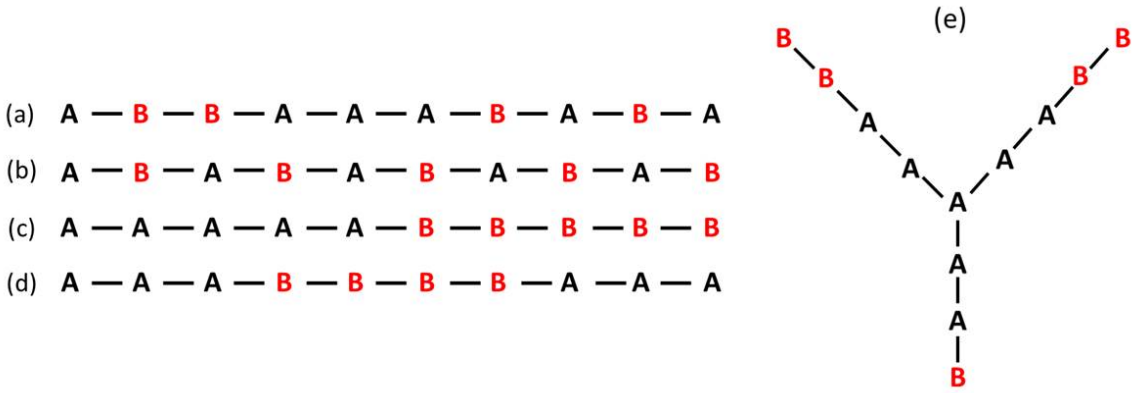

Figure 2.2.: Examples of copolymers consisting of two monomers A and B: (a) statistical, (b) alternating, (c) diblock, (d) triblock copolymer and (e) star-shaped copolymer. Only few monomers of each type are shown for clarity.

early 1940s. According to this model there are two contributions to the Gibbs free energy ΔG_m due to mixing: One coming from the entropy of mixing, which arises from the number of possible configurations of the solutes (e.g. polymer chains), and one of enthalpic origin arising from interactions between the different components of the system (polymer-solvent (p-s), polymer-polymer (p-p), solvent-solvent (s-s)). Under this scope an expression for the ΔG_m is derived as:

$$\Delta G_m = \Delta H_m - T\Delta S_m \tag{2.5}$$

where ΔH_m is the enthalpic and ΔS_m the entropic contribution. The latter is expressed as a function of the degree of polymerization N_i and the or volume fractions ϕ_i of solvent (i=1) and polymer (i=2) (i.e. N_1=1 for monoatomic solvents) as

$$\Delta S_m = RT\left[\phi_1(\ln\phi_1) + \frac{\phi_2}{N_2}(\ln\phi_2)\right] \tag{2.6}$$

whereas, for the former three different interactions (p-p, s-p and s-s) are considered and therefore

$$\Delta H_m = RT\chi\phi_1\phi_2 \tag{2.7}$$

where k_B is Boltzmann's constant, χ the Flory-Huggins interaction parameter and R the gas constant. χ is a dimensionless quantity and describes the excess in pairwise interaction energies between the species. χ is given by

$$\chi = \frac{V_{seg}(\delta_1 - \delta_2)^2}{RT} \tag{2.8}$$

with V_{seg} the volume of a polymer segment and δ_i the respective Hildebrand solubility parameters. χ is experimentally accessible via measurements of the osmotic pressure and, in the regime of infinite solution dilution, by the second viral coefficient A_2 [Orw77]. Thus, the final expression for the Gibbs free energy is

$$\Delta G_m = RT \left[\phi_1 \ln \phi_1 + \frac{\phi_2}{N_2} \ln \phi_2 + \chi \phi_1 \phi_2 \right] \tag{2.9}$$

From Eq 2.8 we can see that $\chi \propto \frac{1}{T}$, a relation that holds true only in the case that purely enthalpic contributions would define the polymer-polymer interaction. However, this is not the complete picture. Entropic contributions come also into play, creating the necessity for empirical corrections, hence the final, complete expression reads

$$\chi = \frac{A}{T} + B. \tag{2.10}$$

The origin of these entropic factors are the presence of excess free volume, the monomer structure, the flexibility of the chain and chain-end effects.

2.3. Self-assembly of amphiphilic block copolymers

A block copolymer in the presence of a selective solvent will spontaneously self-assembly into micellar morphologies [AL00]. For the systems that concern this thesis, we will emphasize on amphiphilic block copolymers (e.g. diblock copolymer) that contain hydrophilic (e.g. poly(ethylene glycol)) and hydrophobic (e.g. polystyrene) blocks dissolved in water. The self-assembly process will drive the system to obtain such a microstructure that the hydrophobic block will reside in the core, whereas towards the water rich regime the hydrophilic block will extend. The physical, driving force behind this spontaneous self-assembly is the natural tendency of the system to minimize the interaction between the hydrophobic and the water, which is energetically unfavourable. Such systems have been proven to be of high interest, since the microenvironment of the core may accommodate particles/molecules that otherwise would be impossible to dissolve in water, hence they can act as enhanced drug delivery systems [LHS+12].

Depending on the characteristics of the system, various morphologies are accessible. The decisive factor that defines the favourable morphology, is the packing of the copolymer chains and how this affects the molecular curvature. Desired morphologies can be targeted by varying the packing parameter p [Isr94]

$$p = \frac{V}{\alpha_e L_c} \tag{2.11}$$

where V is the volume of the hydrophobic chains, α_e the equilibrium area per molecule at the interface and L_c the length of the hydrophobic group. The general rule predicts that for values $p < 1/3$, spherical micelles are favoured, whereas for $1/3 < p < 1/2$ cylindrical micelles.More complex structures, known as polymersomes, are accessible for $1/2 < p < 1$ [Isr11] (see Fig. 2.3). The vast diversity of accessible structures and morphologies of block copolymers, in addition to the possibility to include in such a system a responsive polymer block (e.g. PNIPAM), have created a practically new field of materials that have attracted huge scientific interest over the past few years [BAR09].

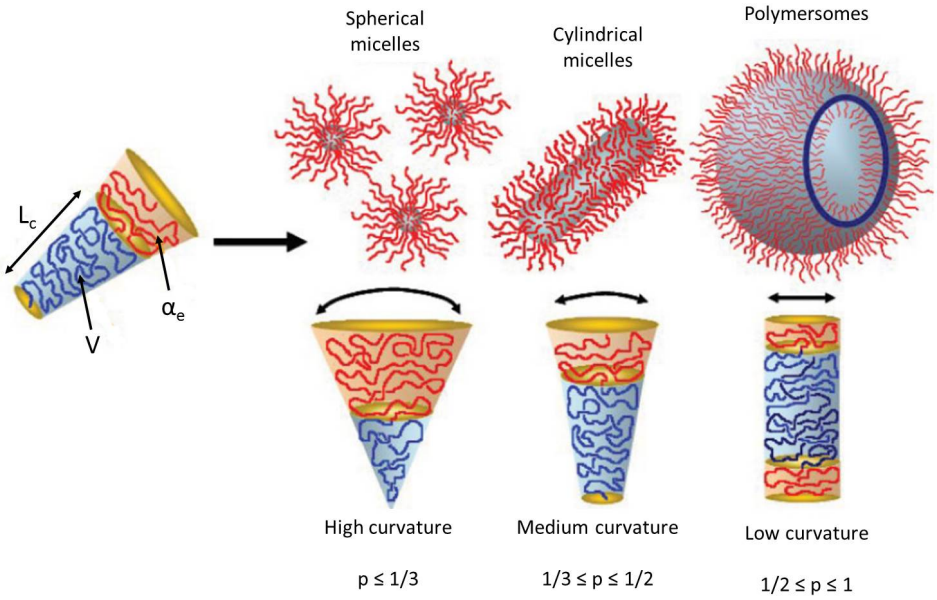

Figure 2.3.: Schematic representation of possible micellar structures for an amphiphilic diblock copolymer in dependence of the packing parameter p. Modified from [BAR09].

Starting from a low polymer concentration in an aqueous solution, we observe single chains, dissolved molecularly termed as *unimers*. At very low concentrations, the surface tension of water is high and does not allow the formation of micelles. As the polymer concentration increases, the surface tension decreases and at a certain concentration, the formation of micelles is favoured. This happens at the so called *critical micelle concentration* (CMC) and it is not a phase transition. Other physical properties of the system are also affected (e.g. osmotic pressure). Typical values for the CMC of nonionic molecules are $\sim 10^{-4}$ M. In general the CMC depends on several factors, such as the nature of the hydrophilic block, the presence or absence of charged groups on the chain and/or the pH

of the environment of hydrophilic block and the type of the hydrophobic block. Regarding the latter, as a general rule, increased hydrophobicity leads to lower CMC values, whereas a similar reduction of the CMC is obtained also by increasing the length of the hydrophobic block. In some special cases, i.e. in ionic surfactants, the CMC depends on the temperature (Krafft point), since the solubility becomes an important factor and changes significantly with temperature. Some non-ionic systems, i.e. PEO/PPO, show also a temperature dependence.

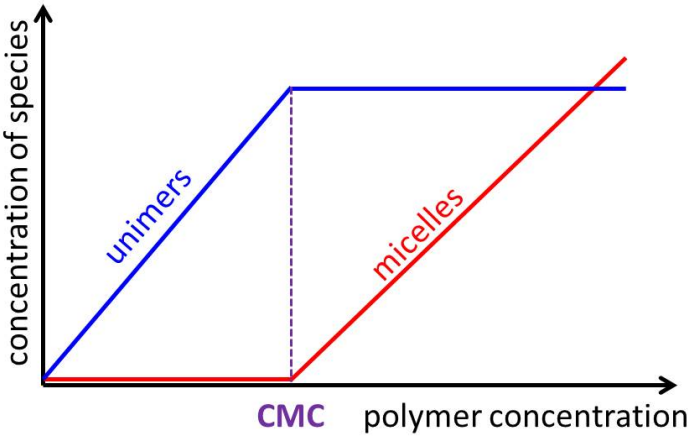

Figure 2.4.: Qualitative representation of the dependence of unimer and micelle concentration on the polymer concentration in the solution.

From a thermodynamic point of view, micellization is well described by the closed association model, which describes a dynamic equilibrium between unimers and micelles. A constant exchange between unimers and chains that participate in micelles is assumed and the process is characterized by an equilibrium constant $K = c_p/c_u$, where c_p is the concentration of the micelles containing p chains and c_u is the concentration of unimers. So the process can be described by the Gibbs free energy per mole of micelles. Thus

$$\Delta\tilde{G}_{mic} = -\frac{RT}{p}\ln K = -\frac{RT}{p}\ln\frac{c_p}{c_u} = -\frac{RT}{p}\ln c_p + RT\ln c_u \tag{2.12}$$

which can be simplified for large p values in

$$\Delta\tilde{G}_{mic} = RT\ln CMC. \tag{2.13}$$

From Eq 2.13 we can derive the enthalpy ΔH_{mic} as

$$\Delta H_{mic} = R\frac{d\ln CMC}{d(1/T)} \tag{2.14}$$

which offers the opportunity to access the enthalpy of micellization by studying the $\ln CMC$ vs $1/T$ dependence. CMC can be determined by fluorescence correlation spectroscopy (FCS) measurements [PKRW14, WÏ14]. Fig. 2.4 summarizes the dependence of the concentration of unimers and micelles as a function of the polymer concentration in the solution. We should mention that Eq. 2.14 is an approximate expression, since it does not consider any dependence of the association number on temperature [AL00].

2.4. Thermoresponsive Polymers

All polymers in solution exhibit thermal sensitivity, since their solubility depends on temperature. Therefore, according to the Hoffman criterion [Hof87], we define as stimuli-responsive polymers only those polymers that exhibit a strong response to a small, external stimulus with severe alteration of their physical properties; i.e. light, pH, temperature. A typical example is the coil-to-globule transition. In the framework of the mean-field theory, the coil-to-globule transition of a polymer in organic medium upon cooling can be predicted: in the ideal case of $M_w \to \infty$ is expected to occur below T_Θ (at the Θ - temperature, the polymer chain adopts an ideal Gaussian coil conformation, and its monomers can be modelled by non-interacting beads on a chain). For a real chain, the transition happens at $T < T_\Theta$ [YAE94]. Below this temperature the solvent becomes a poor one and the monomers condensate. Short-range van der Waals interactions prevail at this stage. An upper critical solution temperature (UCST) behaviour is hence observed here.

In aqueous solutions of non-ionic polymers, a coil-to-globule transition can also occur, but, in that case, different factors determine the transition. Now hydrophilic and hydrophobic interactions define the solubility of the a polymer, rather than the short range van der Waals interactions. The majority of these systems exhibit lower critical solution temperature (LCST) behaviour; the transition occurs upon heating. At a molecular level, the phase transition is accompanied by a disruption of the structure of water molecules that surround specific parts of the polymer chain. As before, the transition here is expected for the ideal case at $T < T_\Theta$. We will elucidate further in the LCST transition in the next paragraphs. Fig. 2.5 shows a schematic representation of the possible phase diagrams, where the transition temperature is presented as a function of the polymer concentration. In most cases the transition is not abrupt, from one- to two-phases region, but a metastable region, which can be found in the phase diagram between the binodal and the spinodal line, is also observed. More information on the details of the phase diagrams and their interpretation will be given in the next paragraph.

In addition to the extremely useful responsive behaviour of these systems, the diver-

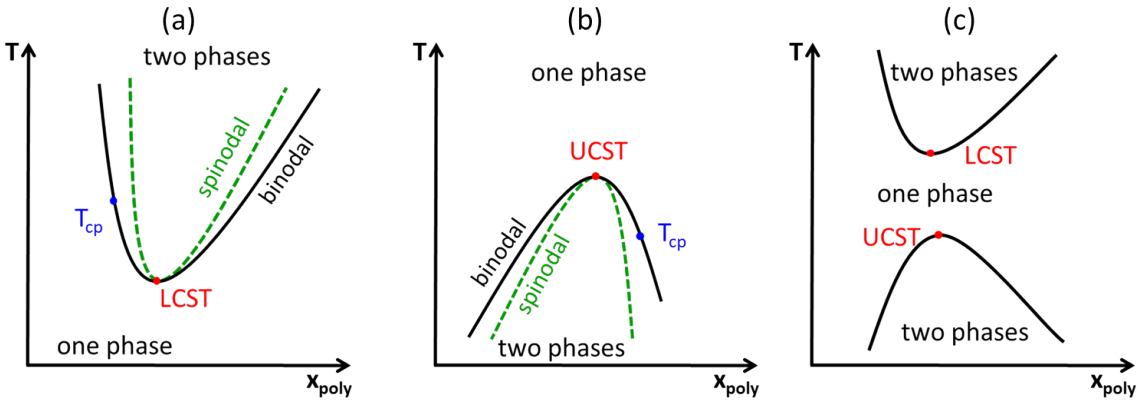

Figure 2.5.: Schematic representation of possible phase diagrams of a polymer that exhibits (a) LCST behaviour, (b) UCST behaviour and (c) both LCST and UCST behaviour. In the first two cases the spinodal lines are also presented in a qualitative manner. The region between the binodal and the spinodal lines is the *metastable region*. In (c) the spinodal lines are not presented.

sity of accessible architectures is another strong advantage [CSHG+10]. The development on the field is lead by the thermoresponsive polymers in aqueous media [RBS13], since here the advantages of the versatility of the these polymer systems are combined with the ubiquitous advantages of water, which is a vital substance for life in earth. The scientific interest in these systems has increased dramatically over the last years, mainly due to the numerous possible applications (e.g. controlled drug delivery systems [NC02, NOM+06], biomedical applications [GZ11, Hof02, TdlHAC+04], filtration [NNH+07], flow controlling [ADA00], biomimetic intelligent surfaces [TKY+06] and many more [DZK06, CSHG+10]). Moreover, they can serve as model systems for understanding the behaviour of biomolecules in aqueous media (e.g. proteins). Thus, a deeper understanding of their responsive mechanism is highly desired, not only under static conditions, but also regarding their kinetic and dynamic behaviour.

2.5. LCST Behavior

As discussed in the previous paragraphs, the majority of non-ionic polymers in water exhibit lower critical solution temperature (LCST) behavior; i.e. their solubility decreases upon heating. Few systems exhibit UCST behaviour and even fewer both USCT and LSCT. From a thermodynamic point of view, the stability of a polymer solution is defined by the behaviour of ΔG_m. As long as the free energy of the mixing is lower than the sum of the respective phases, the phase separation will not occur. As soon as the situation

is reversed, the system phase separates. In other words, in order to allow for phase separation, the shape of the ΔG_m as a function of the volume fraction of the polymer, must be concave. Furthermore, as it can be seen from Eq. 2.9, ΔG_m depends also on the temperature. Therefore, in order to study the phase separation of a polymer solution and create the phase diagram, the Gibbs free energy must be defined as function of the volume fraction ϕ of the polymer at various temperatures. From the shape of the curve (i.e. from the second derivative $\partial^2 G/\partial\phi^2$), stable and instable regions can be marked and transferred to a temperature vs ϕ representation. In a real system, metastable regions can also occur, where small fluctuations of ϕ can lead to different states of the system. The separation between the one and the two phase regions is marked by the *binodal line*, whereas the separation between the metastable and the two phase region is marked by the *spinodal line*. Both can be found from the free Gibbs energy.

Fig.2.5 presents schematic representations of the phase diagrams expected for each of these cases. In this work we will focus on the LCST transition. For sake of clarity we should define here the terminology describing the transition temperature. As it can be seen in Fig. 2.5 the lowest point of the binodal line, which is also the point at which the binodal and the spinodal line meet, is termed as LCST. Hence, for each given system, one LCST value is expected. Any other point on the binodal term is called cloud point (T_{cp}), a term originating from the transition from a transparent solution below T_{cp} to a turbid (cloudy) one above T_{cp}. Depending on the method of detection, T_{cp} can also be expressed as demixing temperature T_{dem}. Through the rest of this work, we will exclusively use the term T_{cp}. Often, the term LCST is incorrectly used instead of T_{cp}, especially in the case of PNIPAM where the phase diagram is relatively flat as a function of polymer concentration (ϕ) (see Fig. 2.7).

According to a more phenomenological description, polymers consist normally of hydrophilic (e.g. ether, amide) and hydrophobic (e.g. amino, isopropyl) groups. When dissolved in water, the former build H-bonds with water molecules, while the latter induce around them a structural organization of water molecules, termed as hydrophobic hydration. The latter may be entropically unfavourable, but the enthalpy gain prevails [BCDLR$^+$14]. As a result, a clathrate-like structure of water molecules is formed and shields the hydrophobic interaction between the hydrophobic groups of neighbouring monomers. A constant interplay, between the hydrophilic and the hydrophobic parts of the polymer chain, is thus present. This interplay defines the change of the solubility upon changing the temperature: as the temperature increases, the hydrophobic character becomes dominant and triggers the phase transition.

Different approaches have attempted to explain the origin of this phenomenon. The most plausible scenario involves the destabilization of the hydration clathrate, which

eventually is disturbed and hence hydrophobicity dominates. As a result the neighbouring monomers associate and the chain collapses. Consequently some of the direct H-bonds break and thus the portion of the water molecules that interact strongly with the polymer decreases. Several studies have shown though, that even above T_{cp}, aggregates of thermoresponsive polymers contain significant amount of water, hence not all of the associated water molecules are liberated at or even above T_{cp} [KNM$^+$05, PKS$^+$14]. Recently a cooperative model, motivated by the transition behaviour of PNIPAM (see below in section 2.6) has been able to capture successfully significant aspects of the phenomenon [OT05, KT10, TKKW11]. In few words, this model predicts the formation of sequences of hydrating water molecules on the polymer chain, which are formed as a consequence of the cooperative character of the hydration mechanism (see Fig. 2.6). The possibility for a successful formation of a H-bond is higher to occur next to an already occupied hydration site. As a consequence, the dehydration process takes place as soon as these hydration sequences are destroyed and is a fast process. In general, the organization of water molecules on, close and around the polymer chain has inspired many experiments and discussion in the literature [Sti80, HW80, MFEM04], since represents this a common ground for linking the phenomena observed in synthetic polymers and biologic systems (e.g. protein folding). For the functionality of the latter, the water organization plays a vital role [HRB14, MM14] and, under this scope, the study of synthetic polymers, that are by far less complex structures than biologic soft matter systems (e.g. proteins), may serve as a basis to gain a deeper understanding of the latter.

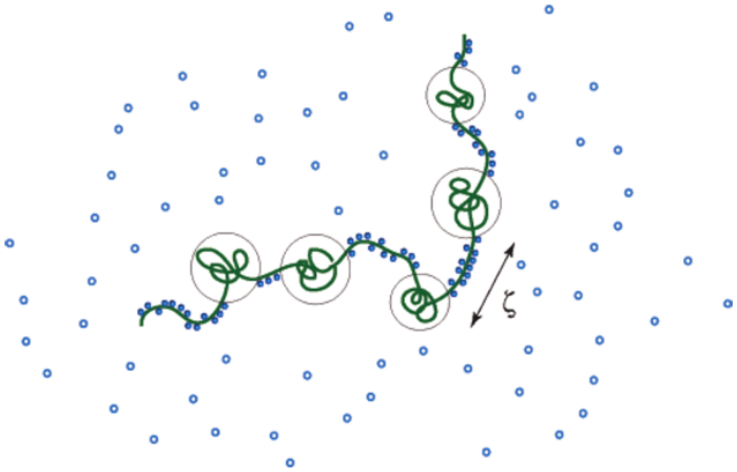

Figure 2.6.: Schematic representation of the cooperative hydration model, inspired from PNIPAM. The hydration process occurs via sequential hydrogen bonds formed along the polymer chain. A cooperative mechanism is postulated to be at the origin [OT05].

2.6. Poly (N-isopropylacrylamide)

Poly (N-isopropylacrylamide) (PNIPAM) (Fig. 2.7) is at present one of the most well known and thoroughly studied thermoresponsive polymers currently existing. Since the first report of its LCST behaviour by Heskins and Guillet in their seminal work [HG68], PNIPAM has attracted strong interest, mainly due to its nominal LCST value that lies at ~ 32 °C [Sch92]. The T_{cp} of PNIPAM is almost independent of the M_w and of polymer concentration (Fig. 2.7). In addition, the diversity of the accessible PNIPAM systems includes single chains, brushes, nanogels, microparticles etc. Moreover, the possibility to tune T_{cp} in a convenient range increases the flexibility of the PNIPAM-based systems. The above mentioned advantages make this system a very promising candidate for a vast range of possible applications.

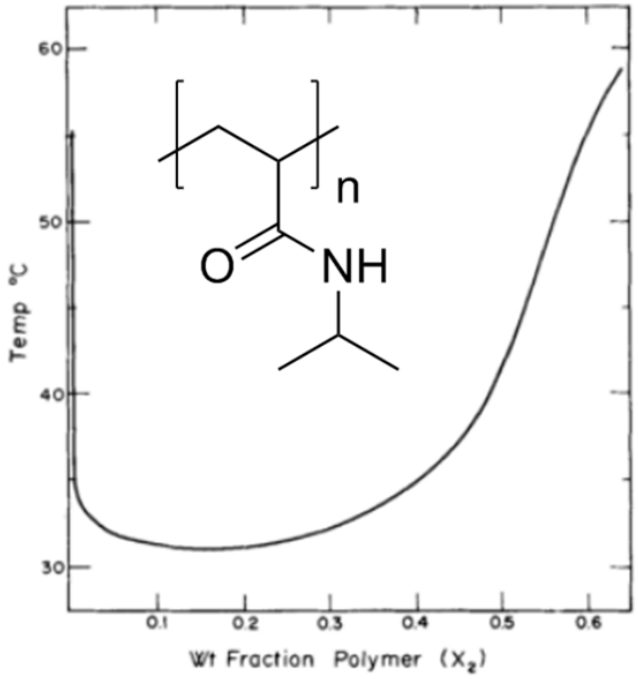

Figure 2.7.: The chemical structure of PNIPAM (inset) and the first ever reported phase diagram of aqueous solution of PNIPAM [HG68].

Each NIPAM monomer bears one hydrophilic group, which offers two H-bond sites (amide group), and one hydrophobic (isopropyl group) (Fig. 2.7). Below T_{cp}, the hydrophilic moieties are hydrated by water molecules, while around the hydrophobic group, a clathrate-like water structure is formed. As the critical temperature is approached, the layer of the structured water fluctuates strongly, resulting in an unstable system. Moreover, the H-bonds break down and, as a result, the system demixes; the polymer

chains expel most of the hydrating water molecules. Above T_{cp} the whole chain is hydrophobic and the segment - segment interaction is now more favourable. The presence of both H-donor and H-acceptor groups on each monomer leads to intrachain bonds between neighbouring segments. In principle, the phenomenon is reversible, but hysteresis is observed [WQW98]. For a linear polymer chain this transition is also regarded as a coil-to-globule transition [YLS+07, IKK13]. Above T_{cp}, the hydrophobic chains tend to associate and to form aggregates, which, in some cases, are stable. Their size is in the range of 50 - 200 nm and they are termed *mesoglobules* [GDCD97, AHL+05, KATW06]. The heating rate has been proposed as possible factor that influences the final size of the aggregates. The origin of this stability is still under investigation and various models have been proposed to explain it. For example, some works propose the presence of hydrophilic groups on their surface [AHL+05]. Another approach postulates an arrest of the initial decomposition by accumulation of charges on the surface of these small aggregates [BDG+07]. Of course, the presence of charges is not required to be only surficial, but probably even the presence of charged groups on the polymer chain could increase the charge per volume ratio during the aggregation and thus act in a similar way. A model focusing on the chain dynamics of the collapsed micellar shell has also been proposed [CGT00]. According to this, the so called *viscoelastic effect* steps in and, due to reduced chain dynamics, the aggregation process is stabilised. In more detail, here the reptation time of the chains on the surface is short compared to the characteristic time between consecutive collisions. Hence, the probability that a collision will lead to a coalescence event decreases dramatically. The physical reason for this is an entanglement force that prevents the free evolution of the aggregation.

2.6.1. Aggregation pathway above T_{cp}

Besides the final state of the system, the kinetics governing the aggregation of thermoresponsive chains or particles (e.g. amphiphilic micellar structures based on PNIPAM) above T_{cp} is of great interest. In fact, dispersions of such materials can be regarded as dispersions of colloidal particles. Different models have been employed over the past 30 years to describe aggregation processes of colloidal particles. Among them, two are the most prominent: the diffusion-limited colloidal aggregation (DLCA) [WHLS84] and the reaction-limited colloidal aggregation (RLCA) [LLW+89] model. Despite the fact that these models have been developed for the aggregation of hard matter colloidal particles (e.g. Au nanoparticles), leading to fractal aggregates [Sor11], in previous studies, also the aggregation of soft matter colloidal particles has been described by these two models [KKCR97]. Nevertheless, in some cases deviations from these models have been

observed [ZCBB11, SLS+12, AGK+13, KPA+14], which may be due to the soft nature of the polymeric particles.

Recent experiments have shown that, even above T_{cp}, the PNIPAM chains contain a significant amount of water (20-60%) [WZ95,KNM+05], and thus the mesoglobules/aggregates are expected to be rather soft than rigid. The picture seems to be even more complicated regarding the response of these systems above T_{cp}, which is not abrupt but rather occurs over a larger temperature range; at least on a molecular length scale [PKS+14]. The experimental evidence of residual hydrophilicity above T_{cp} allows the extension of describing PNIPAM, and in general any soft matter system, not as glassy but rather as soft glassy matter [Sol98], even above the macroscopic phase separation. This has also been highlighted by studies of the elastic modulus of PNIPAM in solution [PMA+12, PMJR+13] and of PNIPAM gels [Hir04].This may be the physical reason that drives such systems to deviate from the universal DLCA and RLCA laws: their aggregation may be governed by the change of their viscosity, which depends strongly on the experimental conditions. Additionally, such aggregates may be able to undergo internal structural reorganization in parallel to their growth, resulting in spherical aggregates; i.e. compact globules, instead of fractals. Inevitably the kinetics of such processes shows unique characteristics and sometimes complex.

In order to account for these deviations, several approaches have recently been developed. For instance, Zaccone et al. postulate that the aggregation of soft matter colloidal particles can be approached by a colloidal gelation mechanism [ZCBB11, ZCB13]. According to this model, the change of the viscosity plays a vital role in the evolution of the process. A model has been developed that links the properties of the system at the molecular level with the macroscopic behaviour. In another approach, Stepanyan et al. follow the previously introduced diffusion-limited coalescence (DLC) model [bA98] to describe the aggregation of polymer particles in solution upon the addition of a poor solvent in the presence of a surfactant [SLS+12, LSS+13]. Even more recently, inspired by data emerging from the project described in this thesis, a logarithmic coalescence model was also created, which includes an energy barrier that hinders the aggregation at the later stages [KPA+14]. Hence, the process enters a kinetically frozen regime where the aggregation is arrested and stable, mesoglobules of typical sized of 40-70 nm are created. These models are employed in results presented in this work, and therefore will be in detail presented in the chapters that they will used in.

2.6.2. Cononsolvency in PNIPAM

The behaviour of PNIPAM in mixed solvents of water and a short-chain alcohol (e.g. methanol, ethanol, isopropanol etc.) has recently attracted strong scientific interest [SSB+14]. Both components, water and e.g. methanol, act separately as good solvents for PNIPAM. Interestingly, in mixed solvents of these two molecules the polymer precipitates for a certain composition range. Starting from a purely aqueous solution of PNIPAM homopolymer, the addition of methanol induces phase separation at ambient conditions in certain range of mixing ratios (Fig. 2.8a). Further addition of methanol results in reswelling and redissolution of the polymer chain [SMT91, OWT01]. Moreover, the LCST decreases strongly upon adding methanol [TKXW11], manifesting an enhanced tendency for phase separation. This phenomenon is named *cononsolvency* and has been reported for various PNIPAM systems: single chains (dilute and semi-dilute conditions) [ZW01, SW10, WSL+12, BCT14], microgels [SLKR10, SHRR12, HPS+12], cross-linked systems [KT12], amphiphilic diblock copolymers [KPA+14] and polymer brushes [LBS05]. The universality of this behaviour is an evidence that the origin of this phenomenon lies in the local interaction between the polymer and the solvent molecules, leaving aside any strong influence of the chain architecture. Most of the studies in the literature emphasize on the behaviour of PNIPAM in mixed solvents of water and methanol, but the phenomenon is also observed upon the addition of other alcohols. Furthermore, it has been observed that the critical composition at which the phase separation occurs, as well as the depression of the LCST, depend strongly on the used alcohol [CF02].

We should stress here that the aim of this work is to study the phenomenon kinetically. The majority of the previous studies done in the field until now concerns static measurements [SSB+14]. This dissertation compiles, especially in the first two chapters, an emphasized, kinetic study of the phenomenon. To the best of our knowledge, this is the first attempt for such an approach and especially by means of time-resolved neutron scattering. The aim is to quantify the effect of the solvation environment on the phase separation and the subsequent aggregation.

Different approaches have been developed to explain the origin of cononsolvency, each focusing on a different component of the ternary system polymer/water/alcohol. The first model puts forward the formation of water-methanol (or an other alcohol) complexes as the main reason for the dehydration of the polymer [ZW01]. According to this model, the solvent-solvent interaction is more preferable than the one solvent and polymer; thus water molecules forsake the polymer chain, which collapses, and prefer to form complexes with methanol molecules via H-bonding. The existence of such complexes (see Fig. 2.9a) in the absence of polymers has been undoubtedly proven by various experimental methods [DCP+02, SF93, MTV+96, NMYM09] and is termed *kosmotropic effect*, but still the link

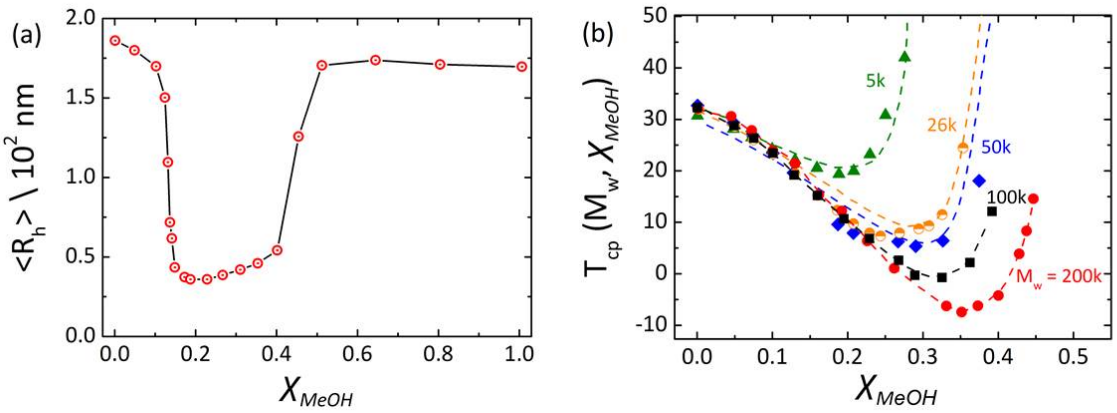

Figure 2.8.: (a) The dependence of the average radius of gyration $\langle R_h \rangle$ on the methanol molar fraction (χ_{MeOH}). The symbols represent DLS measurements on a solution of a linear PNIPAM homopolymer ($M_w = 2 \times 10^7$ g/mol) at a concentration of 10^{-4} g/mL. The line is a guide for the eye. Data from [ZW01]. (b) T_{cp} dependence on M_w and on χ_{MeOH}. The symbols present experimental data obtained by turbidity measurements on PNIPAM solutions at a concentration of 10^{-3} g/mL. The dashed lines show the theoretical predictions of the cooperative model. Data from [TKXW11].

with cononsolvency is missing. In a more recent work, Tanaka et al. have proposed a model, which puts forward the cooperative model for the hydration of the PNIPAM chain [OT05,TKXW11] (Fig. 2.9). Starting from PNIPAM in pure aqueous solution, this model suggests that the hydration of the chain is not a random process but is characterised by cooperativity; the water molecules prefer to occupy free hydration sites that reside next to already occupied hydration sites (Fig. 2.6b). Thus the so-called pearl-necklace conformation of the chain is predicted. The methanol molecules forms also hydrating sequences on the chain, thus both solvent molecules tend to hydrate the chain via a cooperative mechanism. The simultaneous presence of two solvating species leads to a competitive hydration, which manifests itself to a significant decrease of the possibility that any of the two species will achieve to form an H-bond with the polymer. The competition is enhanced by the cooperativity, since the latter can amplify small differences in the composition of the mixed solvent mixture [TKW08a, TKXW11]. As a result the tendency for phase separation increases. Consequently, the ratio of the molar volumes of the two solvating species is expected to play a role, since the formation of sequences along the chain goes along with the spatial displacement of the isopropyl group of PNIPAM; the larger the volume of the hydrating molecule, the stronger the displacement. The latter can act as explanation of the dependence of the strength of the phenomenon on the type of cononsolvent (i.e. alcohol) used [CF02]. This model predicts the flat LCST behaviour of

PNIPAM in pure aqueous solutions (i.e. relatively weak dependence of the LCST on the M_w) and the sharp transition at T_{cp} [OT05]. In the case of cononsolvency, it predicts the dependence of the LCST on the M_w [TKXW11], as it can be seen in Fig. 2.8b. Hao et al. proposed another mechanism, according to which the interaction between chain segments, similar to the screened Coulomb interaction, increases resulting to the enhancement of the phase separation [HCB+10]. The presence of the methanol molecules, disrupts the clathrate-like structures of water that shield the segment-segment interactions and thus the hydrophobic interactions prevail and trigger the collapse of the chain. By increasing the methanol volume fraction, the stronger the phenomenon is.

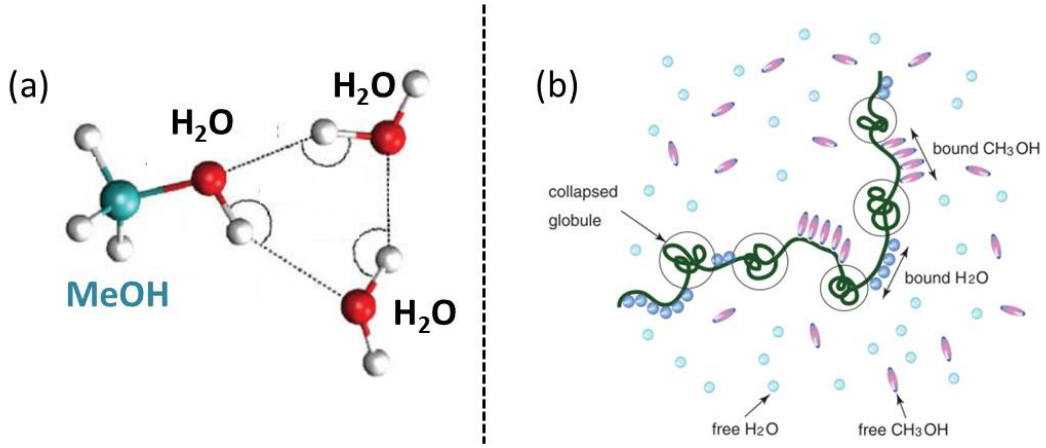

Figure 2.9.: (a) A molecular sketch of the interaction between water and methanol. Modified from [MHRR10]; (b) The schematic representation of the competitive adsorption postulated to take place in PNIPAM solutions in mixed solvents of water and methanol [TKW08a].

By comparing the above mentioned models, it is worth pointing out that both the model by Zhang et al. [ZW01] and by Tanaka et al. [TKXW11] take into account, in different ways, the molar volume of the cononsolvent molecule. In the first case, it is expected that molecules with different molar volumes will affect the water network differently. It has been predicted and confirmed experimentally that alcohol solutes with larger molar volumes leads to an increase of the number of four-coordinated water molecules, whereas the numbers of the three- or two-coordinated ones decrease. In favour of this approach, some recent studies have focused on the alteration of the energetic state of the bulk water by the alcohol. This is expected to influence the the stability of the water molecules that participate in the hydration shell around the hydrophobic isopropyl group [BCDLR+14, BCT14]. In the approach by Tanaka et al., the competitive adsorption is associated strongly with the ratios between the molar volumes of the different solvent species in the solvent mixtures. Generally, it is expected that larger ratios will increase the competition between them, resulting in a enhancement of the tendency for phase separation. Indeed this has

been observed experimentally [CF02]. The larger the molar volume of the solvent species, the higher the entropic gain from the cooperative binding is. So, both approaches acknowledge the importance of the molar volumes of the cononsolvents and predict stronger tendency for phase separation as the molar volume increases. As a concluding point even if cononsolvency has been thoroughly studied by various experimental techniques, still the origin of the phenomenon is unclear. In this work we offer experimental proofs that the phenomenon affects significantly also the behaviour of various PNIPAM systems on a mesoscopic length scale, despite its molecular origin. Moreover, by probing the dynamics of the solvation species at a molecular level, we offer an insight into the interactions that govern the behaviour of the complex system PNIPAM/water/methanol.

3. Characterization methods

In the context of this thesis, neutron scattering is the method of choice. As it will be elucidated in the forthcoming paragraphs, neutrons are an excellent probe to study not only the structure of polymer materials but also their kinetic and dynamic behaviour. By covering a wide range of accessible length scales and energy resolutions neutrons are a useful tool that comprises many important advantages. Neutrons are extremely sensitive to the isotope composition of each substance, therefore it is possible to highlight selectively components of the investigated sample. Based on this unique characteristic, detailed structural information can be obtained. In the special case of polymer solutions, which is the topic of this dissertation, the above mentioned property of neutrons is of vital importance and elevates neutron scattering to the most powerful technique in the field. In addition to that, kinetic measurements with a fine time resolution allows us to follow the aggregation of thermoresponsive polymers upon phase separation and characterize the underlying thermodynamics. Furthermore, measurements with fine energy resolution, allow the study of the dynamics of the different solvation components in the case of cononsolvency, allowing us to enlighten further the molecular picture that governs the phenomenon.

3.1. Neutron Scattering

In the following sections, a detailed introduction to the basics of neutron scattering will be presented. The structure of the chapter and the information given within it are mainly following the references [Pyn90, Ham95, Jac08]. The neutron (n) was discovered by Chadwick in 1932. It is a neutral particle with a mass of 1.0087 atomic mass unit, a spin of 1/2 and a magnetic moment of -1.9132 nuclear magnetons. The absence of charge and the presence of magnetic moment define the interaction of neutrons with matter: it is scattered by atomic nuclei in non-magnetic and magnetic samples or by magnetic moments associated with unpaired electron spins (dipoles) in magnetic samples. In the present work, scattering events from magnetic moments are not considered due to the dielectric nature of the samples; all scattering events are due to short-range nuclear interactions. The interaction probability is usually small, thus the penetration depth in the matter is

high, making neutrons a very powerful tool for investigating the structure of condensed matter. Moreover, their wavelengths are comparable to atomic sizes and inter-distance spacings. Also their energies are comparable to normal modes of energetic states in materials. Hence, neutron scattering is also an excellent tool to probe the dynamics of solid state and liquid materials. Of importance for this work is also the unique property of neutrons to interact with deuterium and hydrogen quite differently, making the deuteration labeling method an advantage, especially in the study of soft matter. The latter leads to the strong advantage of neutrons over x-rays in the case of polymer materials (see Fig. 3.1). The importance of neutron scattering in the study of condensed matter has been highlighted by the Nobel Prize in Physics 1994, which was awarded to B. N. Brockhouse and C. G. Shull for "pioneering contributions to the development of neutron scattering techniques for studies of condensed matter" [nob].

The interaction of neutrons with matter can be classified in different types. In the simplest case we consider the elastic scattering, where no energy transfer between neutron and scatterer takes place. Naturally the complete picture contains also the quasi-elastic and inelastic scattering events, which are in some cases of importance. Moreover, the coherence of the scattered wave has to be taken into account, since the incoherent part may carry important information, e.g. on self-diffusion, depending on the asked experimental questions.

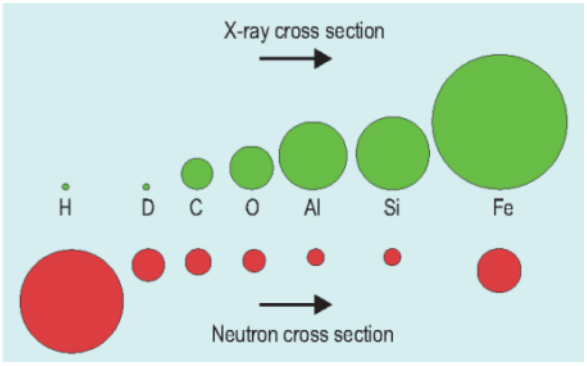

Figure 3.1.: Neutron and x-ray scattering cross-sections compared for several elements [Cro03].

3.1.1. Elastic neutron scattering

Let us consider here the interaction of an incoming neutron beam with a single nucleus, which is assumed to be rigidly fixed and not to exchange any energy with the scattered particle. Under these conditions the interaction can be modelled by a potential $V(\vec{r})$, where $\vec{r}$ is the distance between the neutron and the scattering center (i.e. nucleus).

The comparison of the wavelength ($\lambda \sim 10^{-10}$ m) with the $\vec{r}$ ($\sim 10^{-15}$ m) justifies the assumption that a nucleus acts as a point scatterer.

A collimated monochromatic neutron beam can be regarded case as an assembly of particles flying in parallel directions at the same velocity. Thus it can be described by a plane wave with wavefunction

$$\phi_i = e^{ikz} \tag{3.1}$$

where z is the distance from the nucleus in the propagation direction and k is the wavenumber $k = 2\pi/\lambda$ with λ the wavelength. The assumption of a point scatterer leads to a scattered wave which is spherically symmetrical with wavefunction

$$\phi_s = -\frac{b}{r}e^{ikr} \tag{3.2}$$

where b is the nuclear scattering length of the nucleus and represents the possibility of interaction between neutron and nucleus. The scattering length is a complex number, but the imaginary part becomes only important for materials with high absorption coefficients (e.g. boron). The values of b vary randomly across the periodic table and also vary for isotopes of the same element (see Fig. 3.1). Of importance for the study of bulk polymer materials in general, and polymer solutions specifically, are the values of b for hydrogen (^1H) and deuterium (^2H) which are -3.74 $\times$ 10^{-4} nm^{-1} and 6.67 $\times$ 10^{-4} nm^{-1} respectively. This large difference in neutron scattering between ^1H and ^2H allows the strong variation of the scattering length density of specific components of the system in order to achieve the so called *contrast variation*. This is achieved by substituting components of the investigated system by their deuterated homologues. This ability is one of the key advantages of neutron scattering in polymer science.

The consideration of an assembly of scatterers (i.e. nuclei) will give a scattered wave that can be expressed by the following wavefunction

$$\phi_s = \sum_i (-\frac{b}{r})e^{ikr}e^{i\,\vec{q}\cdot\vec{r}} \tag{3.3}$$

where $\vec{q} = \vec{k}_i - \vec{k}_s$ is the scattering vector with $\vec{k}_i$ and $\vec{k}_s$ the wavevectors of the incoming and the scattered neutrons, respectively. In the special case of elastic scattering, $|\vec{k}_i| = |\vec{k}_s|$, and from the momentum conservation, as depicted by the scattering triangle, (see Fig. 3.2) it can be easily seen that

$$q = \frac{4\pi}{\lambda}\sin\theta \tag{3.4}$$

where 2θ is the angle between $\vec{k}_i$ and $\vec{k}_s$. In an elastic scattering experiment the intensity I of the scattered neutrons is measured as a function of q. By averaging over all directions, the $I(q)$ is obtained, which represents the number of neutrons scattered at a certain angle θ.

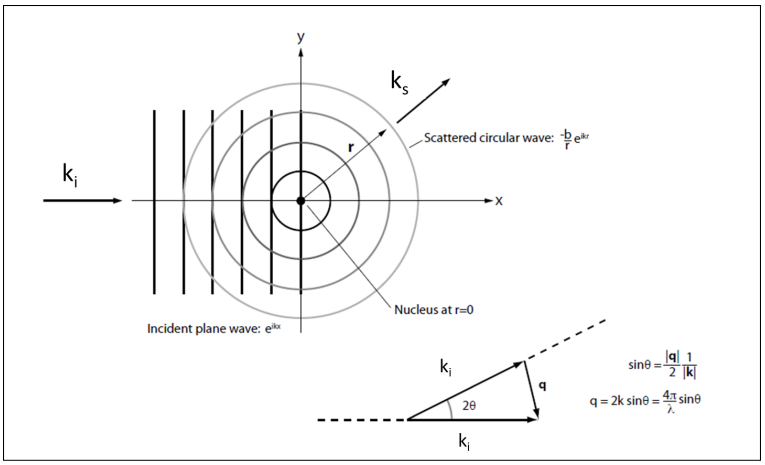

Figure 3.2.: Schematic representation of an elastic scattering event (modified from [Pyn90]).

3.1.2. Scattering cross section

In order to express the probability for a scattering event to occur between an incoming neutron and a scatterer a scatterer (i.e. nucleus), the scattering cross section is used; it expresses the strength of the interaction. The differential cross section describes the probability that a neutron detector will "read" a neutron scattered into the solid angle $d\Omega$ in the direction θ, ϕ, if a total flux of incoming neutrons Φ is assumed, and it is defined as,

$$\frac{d\sigma}{d\Omega} = \frac{\text{number of neutrons scattered into } d\Omega \text{ at angles } \theta, \phi}{\Phi d\Omega}. \tag{3.5}$$

The integration of the differential cross section by the entire solid angle Ω ($\sigma_{tot} = \int \frac{d\sigma}{d\Omega} d\Omega$) leads to the total scattering cross section

$$\sigma_{tot} = \frac{\text{number of neutrons scattered per second}}{\Phi} \tag{3.6}$$

and can be related to the nuclear scattering length of the nucleus over $\sigma_{tot} = 4\pi b^2$. In a typical scattering experiment, the cross section is the quantity that is measured and the challenge is to derive the appropriate theoretical expressions that describe the scattering behaviour of a given system. For more convenience, the values of the cross section are given per atom or per molecule. From Eq. 3.5 and by denoting the velocity of the neutrons with v, we can derive

$$\frac{d\sigma}{d\Omega} = \frac{vb^2 d\Omega}{\Phi d\Omega} = b^2 \tag{3.7}$$

by using $\Phi = v$. If we consider an assembly of N scatterers and integrate over all space, then

$$\frac{d\sigma}{d\Omega}(\vec{q}) = \frac{1}{N}|\sum_{i}^{N} b_i e^{i\vec{q}\cdot\vec{r}}|^2 \tag{3.8}$$

an expression that shows the characteristic q dependence of an elastic scattering experiment. Under the assumption that all scatterers are identical (i.e. are of the same isotope and have the same spin orientation), the material specific property $\rho(\vec{r})$ can be taken outside the sum and the remaining term

$$S(\vec{q}) = \frac{1}{N}|\sum_{i}^{N} e^{i\vec{q}\cdot\vec{r}}|^2 \tag{3.9}$$

depends only on the statistics of the positions of the scatterers and it is called structure factor.

In a real system (i.e. continuous medium) the focus is rather on material properties than on atomic properties. Therefore, it is useful to introduce the scattering length density ρ

$$\rho(\vec{r}) = b_i \delta(\vec{r} - \vec{r_i}) \tag{3.10}$$

or

$$\rho = \frac{\sum_{i}^{N} b_i}{V} \tag{3.11}$$

where b_i is the scattering length density of the relevant atom and V the volume containing the N atoms. By replacing the sum in Eq. 3.8 with an integral across the whole sample and by normalising by the sample volume we arrive at the macroscopic cross section

$$\frac{d\Sigma}{d\Omega}(\vec{q}) = \frac{N}{V}\frac{d\sigma}{d\Omega}(\vec{q}) = \frac{1}{V}|\int \rho(\vec{r}) e^{i\vec{q}\,\vec{r}}\, d\vec{r}|^2 \tag{3.12}$$

which is the quantity measured in any small-angle neutron scattering (SANS) experiment. Even if the integral term in Eq 3.12 is the Fourier transform of the scattering length density distribution, it is not possible inverse recover it unambiguously from the experimentally probed macroscopic cross section. The reason is that the differential cross section is proportional to the square of its amplitude; i.e. all phase information is lost. Nonetheless, different tools can be used in order to quantify the observations. Some of them will be discussed later in this thesis.

3.1.3. Structure factor and form factor

In real systems the assumption of only point scatterers does not always hold. Even in these cases, the density is not just some irregular function of coordinate. The spatial, long range ordered distribution of scattering centres (i.e. spatial correlation) that have a finite size can be captured by the convolution

$$\rho(\vec{r}) = \rho_{centres}(\vec{r}) \bigotimes \rho_{scatterer}(\vec{r}) = \int_V d\vec{r}\, \rho_{centres}(\vec{r}) \rho_{scatterer}(\vec{r} - \vec{r'}) \tag{3.13}$$

where $\rho_{centres}(\vec{r}) = \sum_j \delta(\vec{r} - \vec{r}_j^{centres})$. Following the convolution theorem, the Fourier transform of the density (Eq 3.13) can be expressed as the product of the Fourier transforms of the underlying densities

$$F[\rho(\vec{r})] = F[\rho_{centres}(\vec{r})] F[\rho_{scatterer}(\vec{r})]. \tag{3.14}$$

Hence, the scattering of the whole system $I(q)$ can be expressed as

$$I(q) = S(q)P(q) \tag{3.15}$$

where $S(q)$ carries the information of the relative position of the scatterers (structure factor) and $P(q)$ the information about the ensemble-averaged density within a single scatterer and thus is termed as form factor. The former represents the interference of neutrons scattered from different objects, and the the latter the interference from different parts of the same object. The form factor describes the size and shape of the scattering objects and various analytical models have been developed for many common shapes (e.g. spheres, cylinders etc.). Some of them will be discussed in the next chapter.

3.1.4. Coherent and incoherent scattering

Another point worth discussing here is the coherence of the scattered neutron wave. In the ideal case, the scattered wave would be coherent. However, in real experiments this is not the case; the scattered wave is not fully coherent. The incoherence originates mainly from two sources. Firstly, even in homonuclear systems different components (i.e. different isotopes) coexist, according to their natural abundances. Therefore, the scattering length density of any material contains contributions from all components; an average scattering length must be considered. Secondly, nuclei with non-zero spins contribute to spin incoherence since they create different neutron-nucleus spin states during the scattering process. As a result, the neutron spin of 1/2 couples with the nuclear spin to give states corresponding to parallel and antiparallel spins. In both cases, the mean value of the scattering length, $\langle b_i \rangle$, expresses the coherent scattering, while the "defects" of spin or composition create a fluctuating part that expresses the incoherent scattering, $b_i - \langle b_i \rangle$.

As a result the total cross section, σ_{tot}, can be written as a sum of two components: a coherent, σ_{coh}, and an incoherent one, σ_{inc}).

$$\sigma_{tot} = \sigma_{coh} + \sigma_{inc}. \tag{3.16}$$

While σ_{coh} carries structural information, σ_{inc} yields additional information of the atom-atom self-correlation (i.e. dynamic information). In order to deduce the respective type of information in each case different experimental set-ups have to be used; e.g. SANS focuses on the coherent part of the scattering thus being one of the most powerful tools to investigate the structure of matter, whereas a quasielastic neutron scattering experiment (QENS) uses the incoherently scattered neutrons, in order to probe the dynamics of matter. In all cases, the scattered intensity consists of a coherent and an incoherent part which are weighted by the respective cross sections. Depending on the experimental set-up, the information of interest is probed. In the case of the elastic scattering the scattering signal consists of two contributions and thus, in accordance to Eq. 3.12, it can be expressed as

$$\frac{d\Sigma}{d\Omega}(\vec{q}) = \frac{d\Sigma_{coh}}{d\Omega}(\vec{q}) + \frac{d\Sigma_{incoh}}{d\Omega}. \tag{3.17}$$

In the case of SANS the coherent signal is the one that carries all the information while the incoherent part is q-independent and contributes to the background. The full expression contains also an absorption term, which can be neglected in our case since it only reduces the overall signal [Jac08].

3.1.5. Quasielastic neutron scattering

In a more realistic approach the scatterers are not rigidly fixed but rather free to move around their equilibrium position in solids. Many different mechanisms contribute to this: rotational motions, vibrational motions, phonon excitation etc. As a result, an exchange of energy between the incoming neutron and the nucleus is possible. In terms of the wave picture the frequency is changed by the Doppler effect. Thus a transfer of energy occurs

$$\Delta E = E_i - E_s = \frac{\hbar k_i^2}{2m_n} - \frac{\hbar k_s^2}{2m_n} = \hbar\omega \tag{3.18}$$

where $\omega = (k_i^2 - k_s^2)/2m_n$ and m_n is the rest mass of the neutron. In other words, the scattering triangle in Fig. 3.2 is not anymore isosceles. The application of the cosine theorem will give the following expression for q in the inelastic situation

$$q = \sqrt{k_i^2 + k_s^2 - 2k_i k_s \cos(\theta)} = \sqrt{\frac{8\pi^2}{\lambda^2} + \frac{2m_n\omega}{\hbar} - \frac{4\pi}{\lambda}\sqrt{\frac{4\pi^2}{\lambda^2} + \frac{2m_n\omega}{\hbar}}\cos(2\theta)} \tag{3.19}$$

for non-relativistic particles with rest mass $m > 0$, e.g. neutrons. Eq. 3.19 shows that it can be seen that q is not only a function of λ and θ at a given angle, but also depends strongly on $\hbar\omega$. This is nicely depicted on Figure 3.3 where the dependence of the q on the energy exchange is presented. So, in the case of neutrons this effect has to be taken into account. In comparison, for cases where $|\hbar\omega| \ll E_s$ the above mentioned complication is not of importance. Such examples are x-ray scattering, Brillouin light scattering and dynamic light scattering.

Now the double differential cross section must include an energetic part and, in accordance with Eq. 3.5 it can be expressed as

$$\frac{\partial^2\sigma}{\partial\Omega\partial E'} = \frac{\text{neutrons scattered into } d\Omega \text{ with final energy between E' and E'+dE}}{\Phi d\Omega dE'} \tag{3.20}$$

and under the scope of the previous chapters, the full expression, taking into account also the coherent and incoherent scattering contributions, reads

$$\frac{\partial^2\sigma}{\partial\Omega\partial E'} = \frac{1}{\hbar}\frac{k_s}{k_i}N((b^2 - \langle b\rangle^2)S_{inc}(\vec{q},\omega) + \langle b\rangle^2 S_{coh}(\vec{q},\omega)) \tag{3.21}$$

where S_{coh} is the coherent scattering function that correlates different atoms at different times and S_{inc} the incoherent scattering function that correlates the same atom at different times. These scattering functions are defined as [Zor12]

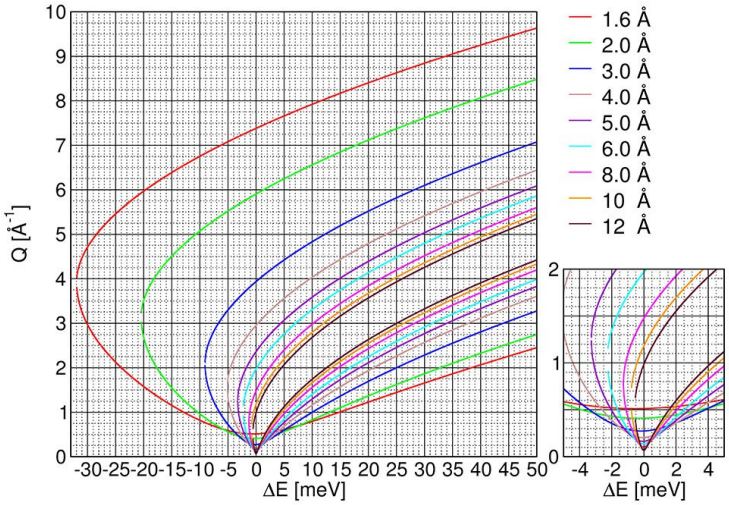

Figure 3.3.: Dynamic range of the TOFTOF spectrometer at the Heinz Maier-Leibnitz Zentrum (MLZ) in Garching for different incident wavelengths [SL], showing the strong dependence of q on ΔE (i.e. $\hbar\omega$) as a function of the selected wavelength can be seen.

$$S_{coh}(\vec{q},\omega) = \frac{1}{2\pi N}\int_{-\infty}^{\infty} dt e^{-i\omega t}\sum_{j,k=1}^{N}\langle e^{(-i\,\vec{q}\cdot\vec{r_j}(0))}e^{(i\,\vec{q}\cdot\vec{r_k}(t)}\rangle \tag{3.22}$$

$$S_{inc}(\vec{q},\omega) = \frac{1}{2\pi N}\int_{-\infty}^{\infty} dt e^{-i\omega t}\sum_{j=1}^{N}\langle e^{(-i\,\vec{q}\cdot\vec{r_j}(0))}e^{(i\,\vec{q}\cdot\vec{r_j}(t)}\rangle. \tag{3.23}$$

In the framework of this thesis, the focus will be on the study of self correlations of tagged particles. Thus, the incoherent part of the inelastic scattering will be studied in order to deduce information regarding the diffusive motion of molecules. In the case where both inelastic and quasielastic scattering events occur, the scattering function $S(\vec{q},\omega)$ can be approximated by

$$S_{inc}(\vec{q},\omega) \simeq f_{\vec{q}}S_{QENS}(\vec{q},\omega) + (1-f_{\vec{q}})S_{inelast}(\vec{q},\omega) \tag{3.24}$$

under the assumption that the two modes, the QENS and the inelastic one, are well separated in the time regime. If this is not the case the most appropriate way to combine the two parts is through a convolution $S_{QENS} \otimes S_{inelast}$. This will not be required here, thus the Eq 3.24 holds. The quasielastic scattering term has the form

$$S_{QENS}(\vec{q},\omega) = \alpha_{\vec{q}}\delta(\omega) + B(\vec{q},\omega). \tag{3.25}$$

The first term $\delta(\omega)$ describes the elastic line and ensures that the intermediate scattering function reaches a non-zero value at the long time limit; i.e $I(\vec{q}, t \to \infty) = f_{\vec{q}}\alpha_{\vec{q}}$. This value is called Debye-Waller factor or elastic incoherent structure factor (EISF). It holds information on the vibrational density of states, which in our case describe vibrational modes of the polymer chains, since the translation diffusion of the chain is too slow to be captured by QENS, at least in the energy resolution window employed in the experiments concerning this work. Additionally, it is related to the mean square displacement (MSD) $\langle u^2 \rangle$ of the polymer chain via the [Wut12]

$$\frac{\langle u^2 \rangle}{3} = \frac{-\ln f_q}{q^2}. \tag{3.26}$$

3.1.6. Intermediate scattering functions

In some cases, it is of interest to use the part of Eq. 3.22 and Eq. 3.23 before the time-frequency Fourier transformation, which is called intermediate scattering function. In the case of the former

$$I_{coh}(\vec{q}, t) = \frac{1}{N} \sum_{j,k=1}^{N} \langle e^{-i\,\vec{q}\cdot\vec{r_j}(0)} e^{i\,\vec{q}\cdot\vec{r_k}(t)} \rangle \tag{3.27}$$

which is equivalent to the integral of the scattering function over all energy transfers

$$I_{coh}(\vec{q}, t) = \int_{-\infty}^{\infty} S_{coh}(\vec{q}, \omega) d\omega. \tag{3.28}$$

The latter is the static structure factor (Eq. 3.9) since at equal t the exponentials can be merged and therefore

$$I_{coh}(\vec{q}, 0) = \int_{-\infty}^{\infty} S_{coh}(\vec{q}, \omega) d\omega = S(\vec{q}). \tag{3.29}$$

From the last expression it is seen that the structure factor in the static case shows the instantaneous correlation of the atoms; the structure of the sample. The dynamic information is lost in the integration process. Following a similar approach the incoherent intermediate scattering function is

$$I_{inc}(\vec{q}, t) = \frac{1}{N} \sum_{j=1}^{N} \langle e^{-i\,\vec{q}\,\vec{r_j}(0)} e^{i\,\vec{q}\,\vec{r_j}(t)} \rangle \tag{3.30}$$

with the sum rule

$$I_{inc}(\vec{q},0) = \frac{1}{N}\sum_{j,k=1}^{N}\langle e^{i\vec{q}\cdot(\vec{r_j}-\vec{r_j})}\rangle = 1 = \int_{-\infty}^{\infty} S_{inc}(\vec{q},\omega)d\omega. \tag{3.31}$$

The incoherent intermediate scattering function is normalized to one for each q and the result is independent of the actual structure of the sample.

3.2. Techniques

3.2.1. Small-angle neutron scattering (SANS)

In a SANS experiment the intensity of the elastically and coherently scattered neutrons as a function of the scattering angle 2θ (i.e. the scattering vector $\vec{q}$) is probed, whereas the incoherent scattering contributes only as flat background. Thus, the small angle is equivalent to the low-q. The realization of a SANS experiment requires small angles and/or high wavelengths (see Eq. 3.4). The achievement of small angles depends on the quality of the collimation and the area detector resolution. A typical sketch of a SANS instrument is depicted in Fig. 3.4. The monochromator is in principle a velocity selector and selects the desired λ. Afterwards, the collimation system, consisting of a set of pinholes, defines the size and the shape of the beam. The neutron beam interacts then with the sample and the scattered neutrons are gathered by a detector as a function of q. The transmitted neutrons are blocked by a beamstop (e.g. made by boron carbide) for sake of durability of the detector. The most accurate type of detectors consist of several modules containing ^3He, but recently other alternatives have been developed due to depletion of ^3He (e.g. solid state detectors). Both the collimation system and the detector lye in vacuum to reduce air scattering and absorption.

3.2.1.1. D22 SANS Instrument, ILL

The SANS experiments presented in this work were performed at the high neutron flux instrument D22 at the Institut Laue-Langevin (Fig. 3.5), in Grenoble, France. Accessible wavelengths vary from 0.46 to 4 nm, depending on the velocity selector set up. The collimation system consists of a several guides that focus the neutron beam. The choice of the free neutron paths occurring depends on the selected sample-to-detector distance (SDD) and vary from 1.4-17.6 m. Normally, the collimation distance and the SDD are chosen symmetrically. The detector used is a gas detector (^3He) that consists of an array of 128 tubes, whereas CF_4 is used as stopping gas. A total sensitive area of 1 m^2 with a pixel size of 0.8 x 0.8 mm^2 is provided. In particular, in our case, the detector was slightly

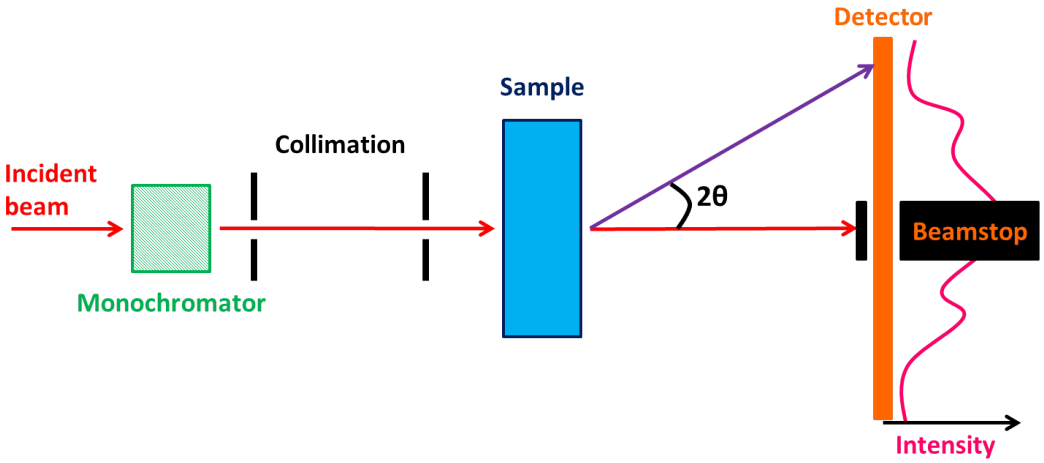

Figure 3.4.: Scheme of a SANS instrument. The neutrons travel through the monochromator and the collimation system, resulting in a neutron beam with a well defined wavelength and size. The transmitted neutrons are absorbed by the beamstop, whereas the scattered by the sample neutrons are gathered by the detector as a function of the scattering angle 2θ. Modified from [Fri12]

asymmetrically placed in order to increase the accessible q-range. The beamstop is made by boron carbide and cadmium and is placed in front of the detector in order to prevent its damage by the direct beam.

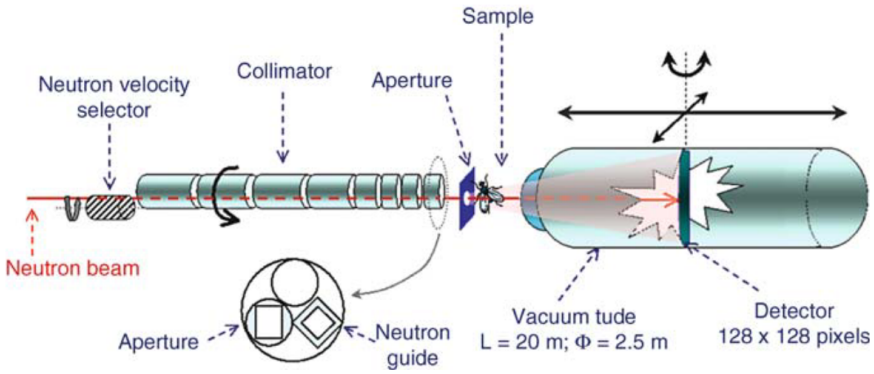

Figure 3.5.: Schematic representation of the high flux, steady SANS instrument D22 located at ILL, Grenoble [Gri08].

For our experiments the selected wavelength was $\lambda = 0.8$ nm with a spread $\Delta\lambda/\lambda = 10$ %. The SDD's chosen were 4.0 and 14.4 m and the collimation lengths at 5.6 and 14.4 m, respectively. These settings together with the asymmetrically placed detector resulted in

a q-range of 0.025 - 2.0 nm^{-1}. The aperture size, which defines the beam size, was 6 mm x 9 mm. The cuvettes used in all experiments had a light path of 1 mm; the illuminated volume (i.e. scattering volume) from the neutron beam was 54 mm^2. In order to focus on the early stages of the aggregation process of the colloidal, thermoresponsive particles, a logarithmic time profile was chosen in the time-resolved measurements: the accumulation time was increasing logarithmically. Slightly different protocols were used in the two different experiments that will be discussed in chapter 5 and 6, therefore more detail will be given in the respective chapters. At the end of each experiment, the transmission was measured by the attenuated flux by the sample in the same way and conditions, as for the direct beam. Corrections regarding the background scattering from the solvent and from any parasitic artefacts were performed. The dark current of the detector was measured using a boron carbide piece to block the neutron beam. The calibration of the detector sensitivity was done by measuring H_2O. The latter was used to convert scattered intensity to absolute units. The obtained 2D images were azimuthally integrated. For all reductions and for averaging the software LAMP, provided by ILL, was used [LAM].

3.2.2. Quasi-elastic neutron scattering (QENS)

In a QENS experiment, on the incoherent inelastic scattering of the studied system is measured. In comparison to three-axes spectrometers, that require single crystals and focus mainly on metal phonon modes, in QENS isotropic/unoriented samples can also be measured. Typical cases, where QENS can be an advantage, are molecular reorientations, certain slow oscillations and jump diffusive or relaxation processes. As discussed before (see paragraph 3.1.4) QENS is a technique that resolves energy exchange between neutrons and matter. Typical values are in the order of μeV to meV depending on the experimental set up. Typically such experiments are performed at time-of-flight (TOF) and backscattering instruments [Wut12]. In the presence of hydrogen the incoherent scattering is expected to dominate the scattering signal and thus can reveal information on the self-correlation of the hydrogen molecules (i.e. molecular diffusion). In the case of a TOF instrument the time of flight for a given neutron can be determined along a certain distance. Thus, by setting the initial velocity (i.e. wavelength) of the neutrons before a scattering event, and by measuring the final velocity (or energy), any occurred transfer exchange can be resolved. By keeping the positions of the detector(s) fixed, the angle is also predefined. The key advantage of this technique is the simultaneous capture of a wide range of momentum and energy transfers [BMS+12].

3.2.2.1. TOFTOF spectrometer

All QENS experiments presented in this work were performed at the TOFTOF direct spectrometer at the Heinz Maier-Leibniz Zentrum (MLZ) in Garching, Germany [UNP07]. Fig. 3.6 shows a schematic representation of the instrument. The double chopper system (seven choppers in total) ensures that all incoming neutrons have, more or less, the same energy (velocity). After the scattering events, the neutrons that interact inelastically with the sample will either lose or gain energy. A wide variety of accessible wavelenghts (1.4 Å - 16 Å) together with the possible chopper set ups (frequency range: 400 min^{-1} - 22000 min^{-1}) allow an energy resolution between 2 μeV and 3 meV. The energy transfer range that can be probed is between -30 meV and 50 meV. The detector consists of an array of 1000 ^3He tubes that cover an angular range from -15° to 140° at a distance of 4 m from the sample.

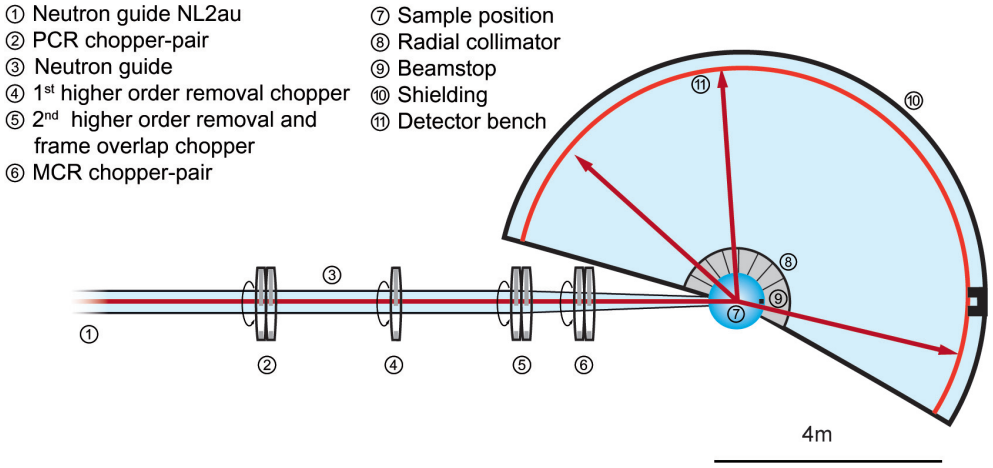

Figure 3.6.: Schematic representation of the TOFTOF spectrometer located at MLZ, Garching, Germany. The time the neutrons need to get from the sample to the detectors encodes their energy loss or gain. The different parts of the instrument are explained in the legend [SL].

For our experiments the wavelength was 6 Å and the chopper frequency was 14000 rpm for the mainframe chopper. This selection leads to an energy resolution of 0.0048 meV and to a q-range of 0.2 - 4 $Å^{-1}$. The samples were mounted in cylindrical, aluminium sample holders with a slit size of 0.1 and 0.2 mm, depending on the sample composition. More details will be given in the respective experimental chapter.

4. Neutron Scattering Data Analysis

4.1. Analysis of SANS data

As discussed also in paragraph 3.1.2, in an elastic scattering experiment all the phase information is lost, due to the fact that the measured intensity is proportional to the squared amplitude. Therefore, in order to extract structural information, one of the possible pathways is the use of analytical models is required [FS87, GK82]. The ones employed in this work will be presented in this chapter.

4.1.1. Guinier-Porod model

Hammouda introduced a new, generalized Guinier-Porod model [Ham10]. It is an empirical model that can describe the shape of diverse particles (e.g. cylinders, spheres etc.). It contains two contributions: a Guinier term at low q-values describing the size and shape of them and a Porod term at higher q values describing surface properties. The formula reads

$$I_{Guinier}(q) = I_G^0 exp\left(\frac{-q^2 R_g^2}{3-s}\right), \text{for } q \leq q_1 \tag{4.1}$$

$$I_{Porod}(q) = \frac{I_P^0}{q^a}, \text{for } q \geq q_1 \tag{4.2}$$

where R_g is the radius of gyration, α the Porod exponent, $3-s$ the dimensionality parameter and I_P^0 and I_G^0 the scaling factors of the two parts. The requirement that both, the values of the two terms and their slopes coincide at q_1, ensures the continuity. Fig. 4.1 shows a example of a scattering curve produced by this model. The parameter s describes the shape of the particles, and it is expected to be 0 for spheres, 1 for rods and 2 for platelets.

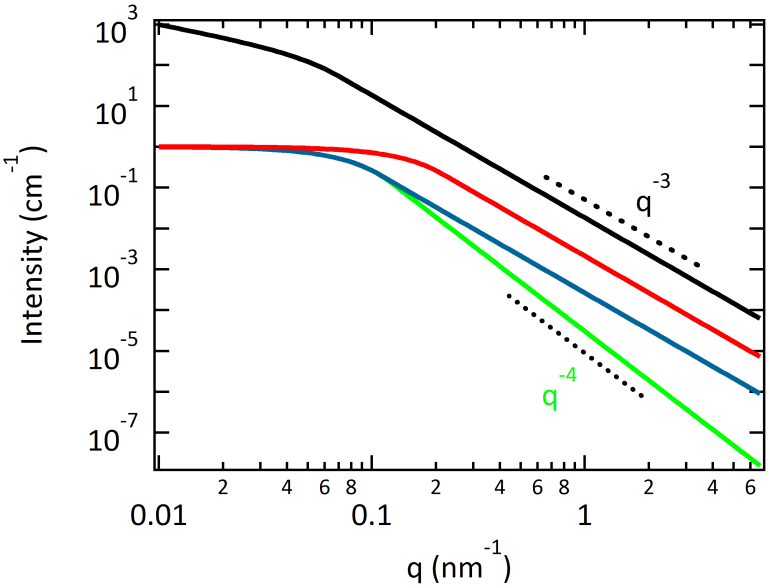

Figure 4.1.: The Guinier-Porod model. The different lines represent the curve for different values of the coefficients. Black line: $s = 1$ (rods), R_g=20 nm, α=3, red line: $s = 0$ (spheres), R_g=10 nm, α=3, blue line: $s = 0$ (spheres), R_g=20 nm, α=3, green line: $s = 0$ (spheres), R_g=20 nm, α=4.

4.1.2. Form factor of spheres with a Gaussian size distribution

This model describes homogeneous spheres with a Gaussian size distribution. It is the result of coupling a form factor for spheres together with an approximation for a statistical distribution of the sizes. The resulting form factor is

$$P_{sph}(q) = \left(\frac{4\pi}{3}\right)^2 N_0(\Delta\rho)^2 \int_0^\infty f(R_{sph}) R_{sph}^6 F^2(qR_{sph}) dR_{sph} \tag{4.3}$$

where

$$f(R_{sph}) = \frac{1}{\sigma\sqrt{2\pi}} exp\left[\frac{1}{2\sigma^2}(R_{sph} - R_{avg})^2\right] \tag{4.4}$$

is the normalized Gaussian distribution and R_{avg} is the average radius. Also

$$F(x) = \frac{\sin(x) - x\cos(x)}{x^3} \tag{4.5}$$

is the scattering amplitude of a homogeneous sphere. N_0 is the total number of spheres per unit volume and $\Delta\rho$ stands for the SLD difference between the spheres and the surrounding solvent, and σ is the polydispersity of the sizes around the mean value. The effect of the polydispersity on the form of the curve can be seen in Fig. 4.2: higher polydispersity values smear out the fringes of the form factor. In the same figure the form of the curve is presented for various values of the coefficients. The volume fraction of the spheres in the solution would alter only the $I(q \to 0)$ value of the curve.

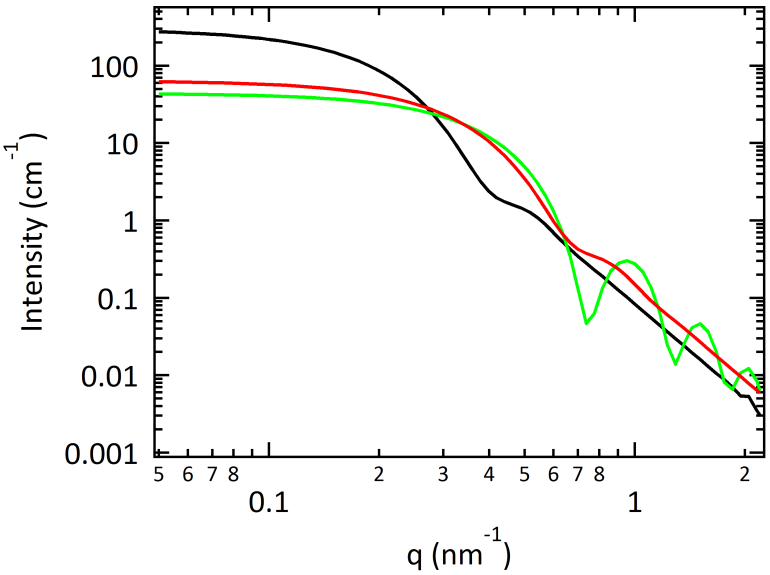

Figure 4.2.: Form factor of spheres with a Gaussian size distribution. The different lines present the resulting curve for different values of the coefficients, in all three cases the volume fraction of the spheres is ϕ=0.02 and the SLD values of the spheres and the solvent are ρ_{sphere}=1.5 $\times$ 10^{-4} nm^{-2} and $\rho_{solvent}$=6.36 $\times$ 10^{-4} nm^{-2}, respectively. Black line: R_{avg}=10 nm, σ = 0.2; red line: R_{avg}=6 nm, σ = 0.2; green line: R_{avg}=6 nm, σ = 0.05.

4.1.3. Form factor for core-shell micelles

In the case of amphiphilic block copolymers that self-assemble in solution into micellar structures, a form factor that describes spherical core-shell micelles is used. This model is especially powerful in the case that one of the components of the micelles is deuterated, in other words when the contrast between the core and the shell is strong enough. In this work this model will be used for describing star-like micelles with a swollen shell, consisting of thermoresponsive PNIPAM shell and fully deuterated polystyrene core (i.e. P(S-d_8)). The form factor that accounts for a micelle with a core and a shell of constant densities is [BO92]

$$P(q) = \frac{1}{3V_{mic}} \left[\frac{3V_{core}(\rho_{core} - \rho_{shell}) j(qr_{core})}{qr_c} + \frac{3V_{mic}(\rho_{shell} - \rho_{solvent}) j(qr_{mic})}{qr_{mic}} \right]^2 \quad (4.6)$$

where r_{core} and r_{mic} are the radii of the core and the entire micelles. The latter is the sum of both the core and the shell. By V_{core} and V_{mic} the respective volumes are denoted. The contrast between the shell and the core are taken into account by the $\rho_{shell} - \rho_{core}$ and between the shell and the solvent by $\rho_{shell} - \rho_{solvent}$. The formula accounts for a micelle with a core and a shell of constant densities. The Bessel function is

$$j(x) = \frac{\sin x - x \cos x}{x^2}. \quad (4.7)$$

Here also the polydispersity of the radius of the micellar radius is taken into account. As it was discussed in the background chapter (chapter 2.1), the polydispersity is an intrinsic property of the polymers. Here a Schulz-Zimm distribution is used for the radius of the core. Using the same expression for the shell would lead to unphysically many fitting parameters, thus r_{mic}will be assumed to be of constant density. The expression describing the possibility that a micelle will have a core radius between r_{core} and $r_{core} + dr_{core}$ is [Ade12]

$$G(r_{core}) = \frac{r_{core}^z}{\Gamma(z+1)} \left(\frac{z+1}{r_{core,avg}} \right)^{z+1} \exp \left[-\frac{r_{core}}{r_{core,avg}} (z+1) \right] \quad (4.8)$$

where $r_{core,avg}$ is the mean value of the core radius r_{core}. The help function Γ is the so-called Gamma Function which is given by

$$\Gamma(x) = \int_0^\infty t^{x-1} e^{-t} dt. \quad (4.9)$$

The variable z is related to the polydispersity σ_{core} by

$$\sigma_{core}^2 = \left(\frac{r_{core,avg}^2}{r_{core}^2} - 1 \right) = \frac{1}{z+1}. \quad (4.10)$$

The full expression that convolutes the form factor with the polydispersity reads

$$P'(q, r_{core,avg}) = \int_0^\infty G(r_{core}) P(q, r_{core}) dr_{core} \quad (4.11)$$

and gives a complex expression that can be found in [BO92].

Fig. 4.3 presents the form factor of a core-shell micelle for different values of the radii of the core and the shell. The effect of the polydispersity is shown as well. For the radii, the position and the height of the local maxima shift as a function of r_{core} and r_{shell}, whereas the polydispersity, as before, smears out the fringes. We should point out that the assumption of constant densities for the core and the shell is obsolete. It has been shown that the density profile of a micellar shell is better approximated by the Daoud-Cotton model [DC82], which uses a power law to describe the density profile of the micellar shell. Moreover, in the literature exist different form factors for core-shell micelles have been proposed that assume an exponential drop of the density with the radius [DHF91,LCH98,SRPL04,LHL$^+$10] or other approaches [FWL96,FB98]. Nevertheless, the approximation of a constant density in the shell used in Eq. 4.6 is considered sufficient within the framework of this thesis and is will be used. The driving force for that is, on one hand, that swollen micelles are only observed for short periods of time in our experiments and due to short accumulation times during that period, the statistics are not sufficient for detailed characterization of the micellar structure.

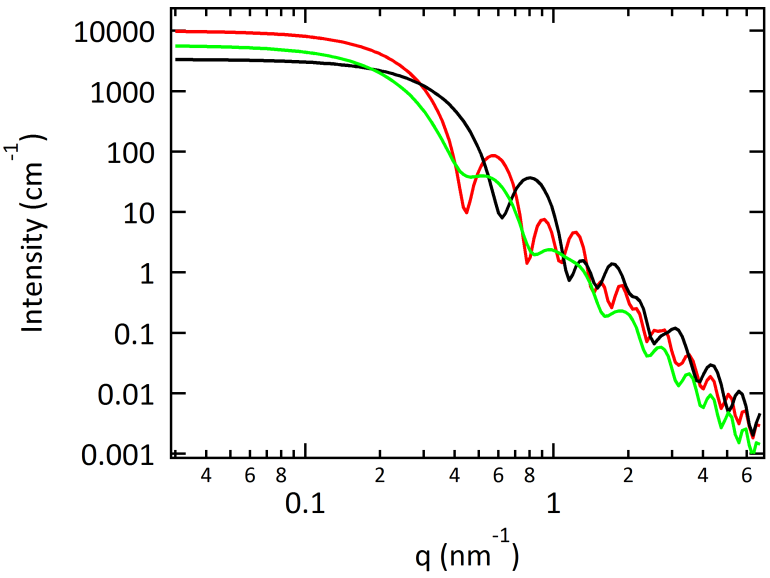

Figure 4.3.: Form factor of core-shell micelles with a polydisperse core. The densities are assumed to be constant for both core and shell. The shape of the curve is presented for various values of the parameters. In all cases ρ_{core}=6.52 $\times$ 10^{-4} nm^{-2}, ρ_{shell}=1.2 $\times$ 10^{-4} nm^{-2} and $\rho_{solvent}$=6.36 $\times$ 10^{-4} nm^{-2}. Black line: r_{core}=2 nm, σ=0.2, r_{shell}=8 nm; red line: r_{core}=2 nm, σ=0.2, r_{shell}=6 nm; green line: r_{core}=2 nm, σ=0.6, r_{shell}=8 nm

4.1.4. Porod law

In the special case, when large particles are present in the solution, their scattering signal dominates the scattering curve. Here, this is the case for large polymer-rich aggregates formed above T_{cp}. This characteristic type of scattering is called Porod-like scattering. Strong, forward scattering dominates the signal and the direct estimation of the radius is not possible. This behaviour is described by the Porod law [Por51]

$$I_{Porod}(q) = \frac{I_P^0}{q^4} = \frac{2\pi(\Delta\rho)^2(S/V)}{q^4} \tag{4.12}$$

that gives the characteristic q^{-4} behaviour at higher q values. $\Delta\rho$ is the contrast between the two phases (i.e. aggregates and solvent) and S/V is the specific surface of the particles. The scaling factor I_P^0 is proportional to the specific surface S/V of the particles, thus the evolution of the radius can be followed indirectly. An increase of the particle size means a decrease of the S/V, i.e. I_P^0 decreases. The expression in Eq 4.12 has been introduced for particles with a smooth surface. In the case of particles with a rough surface or surface with an SLD gradient along the surface normal, deviations from the general q^{-4} behaviour are observed. The former case leads to positive deviations, whereas the latter to negative ones [Sch82]. Therefore in the present work, a free variable α was used instead of 4, in order to account for the properties of the surface (e.g. formation of diffuse boundaries [KMS82]). Thus, the used expression reads

$$I_{Porod}(q) = \frac{I_P^0}{q^\alpha}. \tag{4.13}$$

This generalization of the classical Porod law has the disadvantage that the direct proportionality of I_P^0 to S/V is lost. Nevertheless, I_P^0 as a function of time describes qualitatively the evolution of the size. Fig. 4.4 presents the resulting curve. The influence of the scaling factor I_P^0 and the exponent α is presented.

4.1.5. Ornstein-Zernicke model for density fluctuations

The description of swollen micelles requires also an additional term of model that accounts for concentration fluctuations in the micellar shell. These fluctuations are normally in the range of $\sim$ 2-3 nm, therefore, the respective contribution appears as a shoulder in the high q regime. The expression, originating from the Ornstein-Zernicke model [OZ14], reads

$$I_{OZ}(q) = \frac{I_{OZ}^0}{1 + q^2\xi^2} \tag{4.14}$$

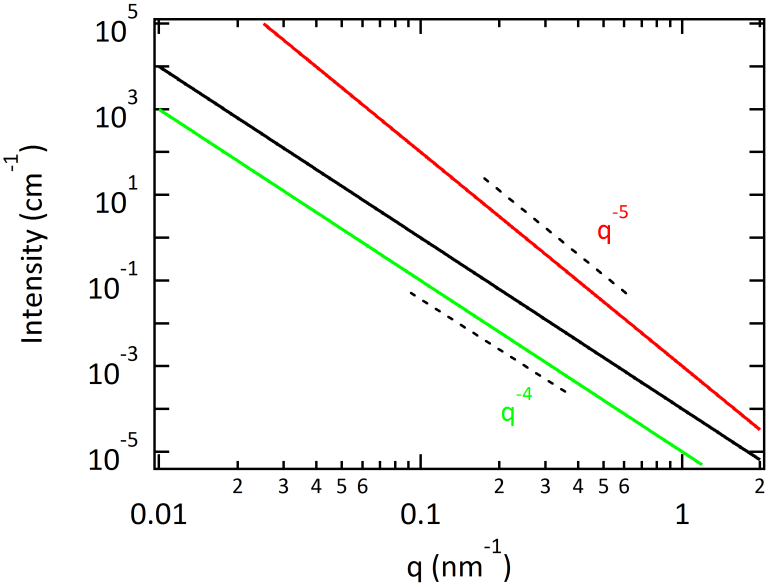

Figure 4.4.: The Porod law describing large particles (e.g. large aggregates). Black line: I_P^0=1x10^{-8}, α=4; red line: I_P^0=1x10^{-8}, α=5; green line: I_P^0=1x10^{-9}, $\alpha = 4$.

where I_{OZ}^0 is the amplitude of the contribution and ξ the characteristic length of the density fluctuations. Moreover in this work, this model was added also in the case of very big aggregates, in order to account for a small contribution at high q values. These contribution may arise from trapped solvent molecules that reside inside these large aggregates, even far above T_{cp}. The idea of partially hydrated PNIPAM chains even above the T_{cp} has recently been demonstrated, as discussed in chapter 2.6.1. Hence, this model is used here for describing both the density fluctuations within the micellar shell, in the swollen state, and those within the big aggregates formed by hydrophobic chains or micelles at temperatures above the T_{cp}. Fig. 4.5 presents the shape of this contribution for different values of the coefficients.

4.1.6. Resolution function

An important factor that has to be taken into account here is the instrumental resolution. Besides the polydispersity, which was discussed briefly in section 4.1.3, the instrumental resolution results also in additional smearing of the experimental data [SSSI74, WCR88]. The main contributions to this smearing of the ideal scattered intensity are three: the finite size of the incident beam, the wavelength resolution and the pixel size on the detector [PPM90]. The first two effects contribute significantly, whereas the effect of the pixel size (0.8 x 0.8 mm^2) can be neglected.

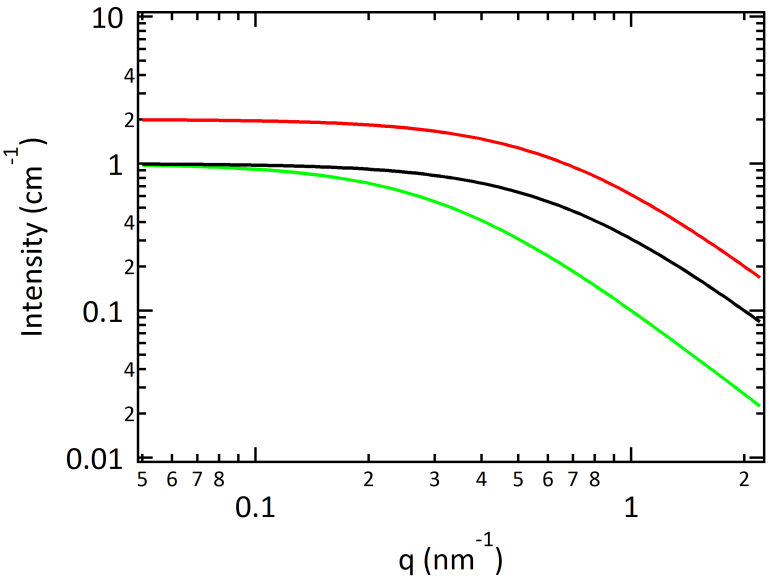

Figure 4.5.: The Ornstein-Zernicke (OZ) contribution describing density fluctuations in swollen micelles or in very large aggregates. Black line: I^0_{OZ}=1 cm^{-1}, ξ=1.5 nm; red line: I^0_{OZ}=2 cm^{-1}, ξ=1.5 nm; green line: I^0_{OZ}=1 cm^{-1}, ξ=3 nm.

The resolution at a given q can be written as [Gri01]

$$\Delta q = -q\left(\frac{\delta\lambda}{\lambda}\right) + \left(\frac{4\pi}{\lambda}\right) \tag{4.15}$$

and thus

$$(\Delta q)^2 = q^2\left[\left(\frac{1}{2\sqrt{2\ln 2}}\frac{\Delta\lambda}{\lambda}\right)^2\right] + \left[\left(\frac{4\pi}{\lambda}\right)^2 - q^2\right](\Delta\theta)^2 \tag{4.16}$$

where $\Delta\lambda/\lambda$ is related to the full width at half maximum value of the triangular function describing the wavelength distribution and $\Delta\theta$ is related to the divergence of the direct beam. These two values depend on the experimental set up. For the SANS instrument D22, where the experiments of this work have been performed, the values were taken from [Gri01]. The resolution function is defined as

$$R(q, q', \Delta q) = \frac{1}{\Delta q\sqrt{2\pi}}\exp\left(-\frac{(q'-q)^2}{2(\Delta q)^2}\right) \tag{4.17}$$

and finally the experimentally measured intensity is modelled by the convolution of the fitting function with the resolution function

$$I_{exp}(q) = \int_{-\infty}^{\infty} R(q, q', \Delta q) I(q') dq'. \tag{4.18}$$

The resolution function is a Gaussian form with a width of Δq. To reduce the computational time during the convolution, the real range of the integration is $\pm 3\ \Delta q$, since within this range the 99.73 % of the values is considered. The effect of the resolution on the shape of the curve is presented in Fig. 4.6. Here, as an example, the case of the core-shell micelle form factor. Similar observations have been made also for other fitting functions. Partially, the effect is similar to the one of the polydispersity; the local minima of the curve are smeared out. Moreover, an influence at the lower q regime is observed. Thus it is difficult in some cases to distinguish the contribution of the two factors. A detailed discussion is presented in [Gri01].

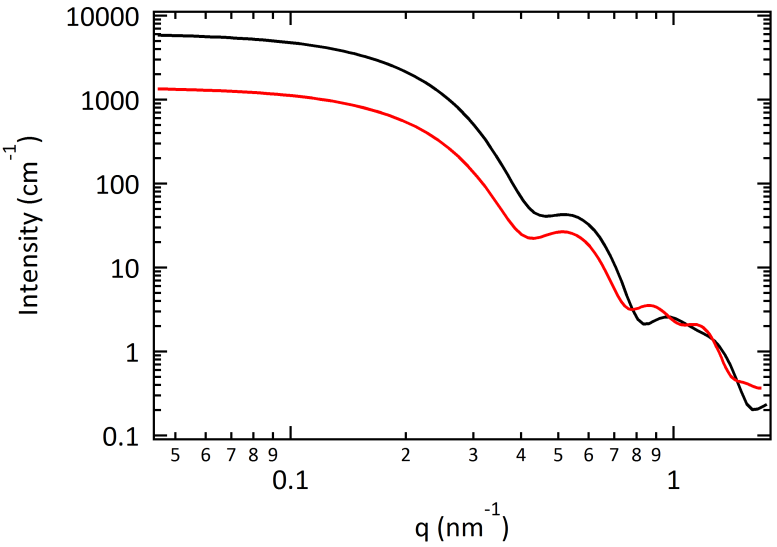

Figure 4.6.: The effect of the resolution function on the form factor of spherical core-shell micelles. The values of the coefficients are the same in both cases: ρ_{core}=6.52 $\times$ 10^{-4} nm^{-2}, ρ_{shell}=1.2 $\times$ 10^{-4} nm^{-2} and ρ_{solv}=6.36 $\times$ 10^{-4} nm^{-2}, r_c=2 nm, σ=0.2, r_s=8 nm. Black line: non-smeared function, red line: smeared function.

4.1.7. Incoherent background

As discussed also in the previous chapter, in a SANS experiment the coherent part of the scattering is carrying all the interesting information, whereas the incoherent part contributes as a flat background (see Eq. 3.17). Therefore, it must be taken into account

during the data analysis. This is done sby adding a q-independent term to the analytical model, thus the final fitting expression is always

$$I(q) = P(q) + I_{inc} \tag{4.19}$$

and the value of I_{inc} can be calculated in dependence on the composition of the sample. The incoherent scattering cross section of the respective atoms are retrieved from [Sea92] and then, by using the molar mass and the mass density of the molecules are converted into an incoherent background. The calculated value was always compared to the experimental one, and found to be similar within the uncertainties. Thus, the incoherent background was kept as constant to the value defined experimentally from the experimental curves at the later stages of the time-resolved experiments.

4.2. Analysis of QENS data

In the case of QENS, the focus is on resolving information on the diffusive behaviour of molecules. Whereas the elastic scattering here is not of interest, we focus on the quasi-elastic part of the scattering. This is done by analysing the shape of the curve around the zero energy transfer peak (i.e. elastic line). In the more general and simple case case is the use of a Gaussian fit function, which holds for an ideal gas. Here a Gaussian is used to describe the elastic line

$$G(\omega, \Gamma) = \frac{1}{\sqrt{2\pi}\Gamma} exp\left(\frac{-\omega^2}{2\Gamma^2}\right) \tag{4.20}$$

where Γ is the width of the function or relaxation rate. For describing diffusion of real particles in any environment, the use of a Lorentzian scattering function is appropriate. The normalized Lorentzian has the form

$$L(\omega, \Gamma) = \frac{1}{\pi} \frac{\Gamma}{\Gamma^2 + \omega^2}. \tag{4.21}$$

Again Γ is the width (relaxation rate) of the diffusion mechanism that creates it. The behaviour of Γ as a function of the scattering vector reveals not only the type of the diffusion mechanism, but also offers access to the diffusion coefficient (D). Depending on the type of diffusion, different models are used. In the case of the jump diffusion model the width of the Lorentzian (Γ) is given as a function of the diffusion coefficient D_{jump} and the residence time τ_{res}:

$$\Gamma(q) = \frac{D_{jump} q^2}{1 + D_{jump} \tau_{res} q^2}. \tag{4.22}$$

The translational diffusion of water molecules obeys such a jump-like diffusive process. This has been shown in many studies and holds not only for free water, but also for water with reduced dynamics (e.g. in the case of hydration of macromolecules) [QSH11, PKS+14]. Moreover it has been shown that similar behaviour is expected for other small molecules forming a network via H-bonds (e.g. methanol). When more than one solvent population exist, i.e. with different mobilities, the use of more than one Lorentzians is required. In that case the total fitting function is

$$S(q,\omega) = \alpha_{el}(q)\delta(\omega) + \sum_i \alpha_i(q)\frac{1}{\pi}\frac{\Gamma_i(q)}{\Gamma_i^2(q)+\omega^2} \tag{4.23}$$

where i is the respective solvent molecule population.

As it was discussed in paragraph 3.1.5, from QENS it is possible to extract information on the mean square displacement $\langle u^2 \rangle$ of the polymer chain, which is slower than the diffusion dynamics of the solvation molecules and is thus included in the elastic line. By assuming a harmonic oscillator for the vibrational modes of the polymer, the elastic line can be written as

$$I_{el} = I_0 \exp(-\langle u^2 \rangle q^2) \tag{4.24}$$

with I_0 constant [OSKY09]. It is expected that the contribution of the elastic component from PNIPAM will be more pronounced when the solvent contains more deuterated species. This is due to fact that the incoherent scattering from H atoms in PNIPAM is much larger that the coherent part from D and incoherent part from O atoms in the solvating molecules.

4.2.1. Instrumental resolution

The resolution in a QENS experiment have a finite resolution. This defines in principle the energy resolution accessible under the given conditions. Consequently, the measured spectrum $S_{meas}(q,\omega)$ is the convolution of the model scattering function $S(q,\omega)$ with the resolution function $R(q,\omega)$

$$S_{meas}(q,\omega) = R(q,\omega) \otimes S(q,\omega) + bkg \tag{4.25}$$

where bkg is the constant background. Experimentally the resolution is determined in a measurement of a purely elastic scatterer (e.g. vanadium), that defines the width of the elastic line.

5. Methanol volume fraction jumps

In this chapter the aim is to study the collapse transition and the subsequent aggregation induced upon the rapid addition of a cononsolvent (i.e. *d*-MeOD) in aqueous (in D_2O) solutions of PNIPAM homopolymers and amphiphilic PS-*b*-PNIPAM block copolymers. As was mentioned before, the special interest in this work lies with the employemnt of time-resolved measurements. This will allow to study kinetically the phase separation induced upon the addition of methanol. The latter expected to lead to a collapse of the PNIPAM chain in the former case and to the collapse of the micellar shell in the latter. In both cases the hydrophobic entities will form large aggregates with time. Fig. 5.1 shows a schematic representation of how the two systems are expected to respond to the addition of methanol.

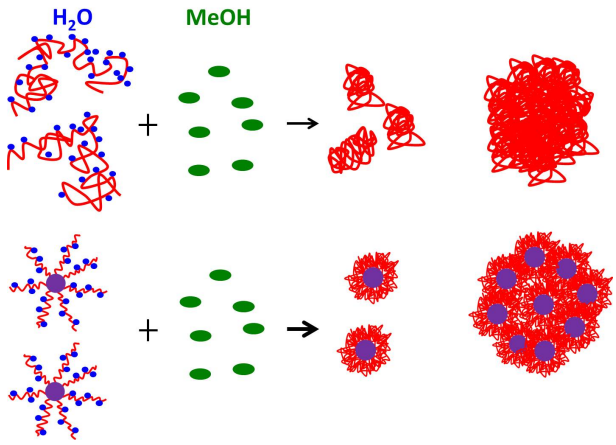

Figure 5.1.: A schematic representation of how the two solutions, i.e. homopolymer and micelle forming diblock copolymer in pure D_2O, are expected to respond to the addition of *d*-MeOD. Large aggregates will be formed in both cases. The aim in this part of the work is to unravel the pathway that leads to the respective final state.

The collapse transition and the subsequent aggregation are probed by means of TR-SANS coupled with a stopped-flow device to realize the methanol content jump. The first question to be addressed is the influence of the amount of the *d*-MeOD added. Therefore we chose three different volume fractions of *d*-MeOD. The second question

regards the comparison between the two polymer system and in detail how the different chain conformations will affect the behaviour of the respective systems. In the case of the diblock copolymer we employ theoretical models to quantify the aggregation process above T_{cp}. We observe that the different solvation environments modify the aggregation pathway even at a mesoscopic length scale. The chapter is structured as follows: First an overview of the experimental set-up is given, then the results for the homopolymer follow and afterwards the results for the diblock copolymer. Then, a discussion regarding the aggregation pathway followed by the PS-*b*-PNIPAM is presented. A summary of the results and a short comparison between the two systems is given at the end.

5.1. Strategy

This part of the present work focuses on the influence of the addition of different methanol volume fractions on the collapse behaviour and the subsequent aggregation of PNIPAM aqueous solutions. Moreover the question arises whether the architecture of the PNIPAM chain will play a role during the cononsolvency phenomenon. To address these two points, the following strategy was chosen. Two different PNIPAM systems were selected: a PNIPAM homopolymer ($M_w = 22500$ g/mol, purchased from Sigma Aldrich) and an amphiphilic diblock copolymer PS_{14}-*b*-$PNIPAM_{310}$ ($M_{w,PS}$=1700 g/mol, $M_{w,PNIPAM}$=35000 g/mol, synthesized by RAFT polymerization [BKGL$^+$10]). The intrinsic difference between the two systems is that, when dissolved in D_2O, the latter forms star-like micelles; the PNIPAM chains are tethered onto the hydrophobic PS core. Therefore the two systems are expected to exhibit different PNIPAM chain dynamics. Both polymers were predissolved in D_2O at a concentration of 20 mg/ml. Then three different methanol volume fractions (i.e. fully deuterated methanol *d*-MeOD) were added rapidly to these solutions in order to induce the phase separation; 10 v/v (i.e. 90:10 % v/v D_2O:*d*-MeOD), 15 v/v and 20 v/v are chosen as mixing ratios. The induced phase separation was characterised by means of TR-SANS, whereas the phase diagram was constructed by turbidimetry prior to the neutron beamtime. The use of deuterated solvents ensures the strengthen on the good contrast between the polymer and the surrounding solvent taking advantage of the increased contrast between protonated and deuterated species. The time-resolved character of the SANS experiment will allow us to resolve the aggregation process that follows the phase transition with a fine time resolution and reveal any influence of the chain architecture and/or the methanol volume fraction.

5.2. Experimental set-up

The TR-SANS experiment presented here were performed at the high-flux SANS instrument D22 at ILL, in Grenoble, France. For the rapid addition of the *d*-MeOD to the PNIPAM or PS-*b*-PNIPAM solutions in D_2O a stopped-flow instrument Biologic SFM-300 was used. Fig. 5.2a shows a picture of the instrument and Fig. 5.2b a schematic representation of its interior. Three syringes were used; in the first the initial polymer solution (always at an initial concentration of 20 mg/ml) was kept, in the second *d*-MeOD for mixing with the polymer solution and in the third one MeOH for cleaning the sample cell. All syringes and also the sample cell were kept at a temperature 3 K above the respective T_{cp} of the final mixture. The presence of a mixing chamber and a delay line ensured the proper mixing of the two components and the homogeneous flow of the sample in the cuvette (see Fig. 5.2b). The latter was a quartz glass cell of nominal thickness (neutron light path) of 1 mm. The mixing ratio of the polymer solution with *d*-MeOD was controlled by choosing the appropriate flow rates for the appropriate syringes. Before starting a new measurement, a fresh amount of 1 ml polymer solution was injected in the first syringe and was left to equilibrate thermally for 10 min. The sample cell was homogeneously filled by injecting remotely an overall amount of $\sim$ 1 ml of the mixed solution. The system was controlled by a computer and a transistor-transistor logic (TTL) signal started the detector data acquisition at the end of the sample injection. Hence a good reproducibility of the measurements was ensured. In all cases visual inspection at the end of each run revealed that the solution had become turbid in the sample cell. After the end of the experiment, the MeOH from the third syringe was used to clean the sample cell. In the next step, *d*-MeOD was used to rinse the sample cell until the counts on the detector dropped to a sufficiently low value ($\sim$150 counts/sec). This way, it was ensured that no contamination from MeOH would spoil the next measurement.

In order to focus on the first steps of the process the following time profile was chosen: the first image was taken with an acquisition time of 0.1 s, and then, the time was increased by a factor of 1.1 for the first 60 images; the overall time of this first part was $\sim$5 min. For the remaining 30 min the measuring time was 30 s per frame. In total, each run lasted 35 min. Each run/jump was repeated twice for the SDD of 4.0 m and thrice for the SDD of 14.4 m; thus the statistics was improved. In all cases, the azimuthally averaged intensity curves did not show systematic differences and were averaged.

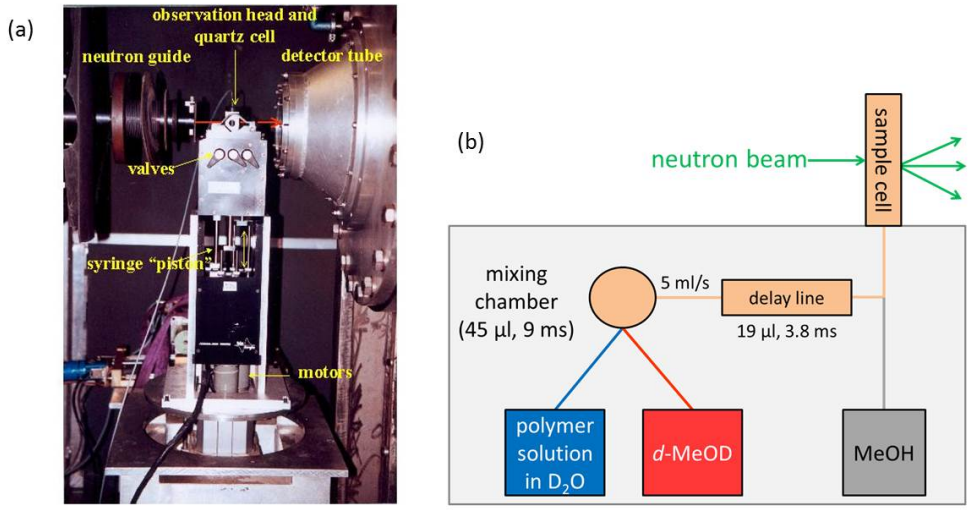

Figure 5.2.: The stopped-flow instrument SFM-300 by Biologic. (a) A photograph of the actual device mounted on the beamline together with some explanatory notes [Gri] and (b) a schematic representation of how the instrument was used in the presented in this chapter experiment. The times shown on the sketch are the respective residence times and their calculation was made based on the selected flow rates.

5.3. Phase diagram

The phase transition was studied at first by means of temperature-dependent light transmittance (Fig. 5.3a) in order to create the phase diagram. The latter is vital in order to design correctly the SANS experiment. The resulted T_{cp} of all samples are presented in Fig. 5.3b. The concentration chosen here and throughout the whole experiment lies far above the CMC of PS-*b*-PNIPAM in D_2O and therefore the majority of the chains is expected to reside in micelles [AMKBK$^+$11]. The PS is hydrophobic and not soluble in MeOH, thus forms the core, while the PNIPAM chains extend from it below the T_{cp} forming star-like micelles. The same polymer concentration was used also for PNIPAM homopolymer for sake of consistency between the two systems. In case of the diblock copolymer, the micellar shell collapses and the collapsed micelles form large aggregates. For the homopolymer, the chains become hydrophobic above the T_{cp} and also associate into big aggregates. The difference observed in the T_{cp} of the two systems in pure D_2O (32.3 ± 0.5 °C for PNIPAM and 29.5 ± 0.5 °C for PS-*b*-PNIPAM) may originate from steric hindrances due to the presence of the hydrophobic PS blocks. A decrease of the solubility in water and subsequently of T_{cp} is observed. Upon the addition of *d*-MeOD, the T_{cp} decreases for both systems, as expected. The absolute values obtained here are in good agreement with previous studies [TKW08a, CF02, WRV90].

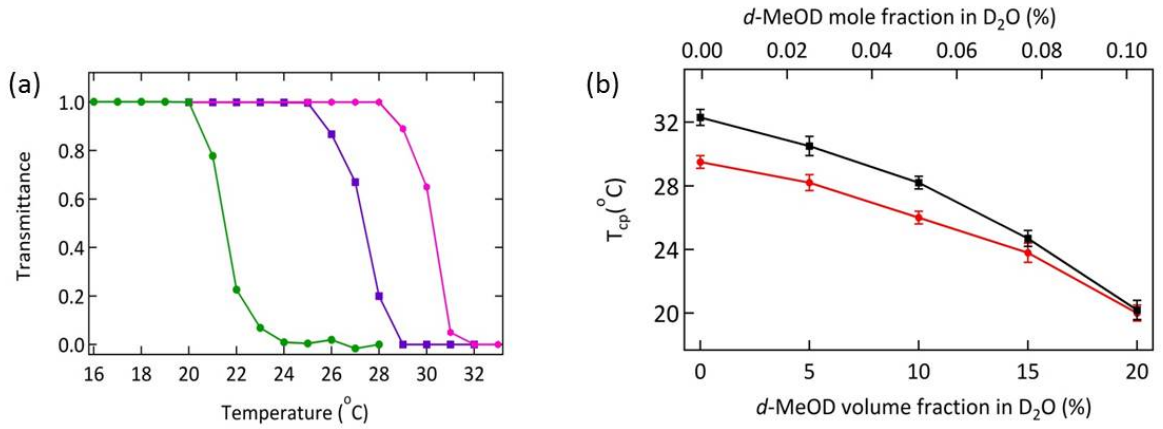

Figure 5.3.: (a) Temperature-resolved light transmittance of solutions of PNIPAM in 90:10 v/v (magenta circles), 85:15 v/v (violet squares) and 80:20 v/v (green circles) D_2O/*d*-MeOD. (b) Cloud points of PNIPAM (black squares) and PS-*b*-PNIPAM (red circles).

5.4. PNIPAM homopolymer

Firstly, the results obtained for the PNIPAM homopolymer are discussed. Fig. 5.4 shows all the measurements performed for this system. The scattering intensity $I(q)$ is presented as a function of the scattering vector (q) for the whole time range probed in this experiment. Each curve, represents one measurement, and thus the evolution of the aggregation process can be followed with the help of this representation. A qualitatively analysis shows that all systems exhibit strong forward scattering throughout the whole probed time range. Due to short measurement times at the beginning, the statistics are low; thus the curves do not show any prominent features. Later on, when the measuring time is longer, the curves are smooth and show small changes only slightly with time. The featured forward scattering (i.e. Porod-like scattering) is an evidence of large aggregates ($\geq$ 150 nm) in the solution. The fact that it is present right from the first curves acts as evidence that the collapse transition occurred before the first measurement; the demixing process occurred in the mixing chamber and/or the delay line of the stopped-flow device (i.e. it is faster than the dead time of the set-up which is 0.1 s). Despite this, we are able to follow and characterise the aggregation process in the later stages.

In order to obtain quantitative results, we proceed with the fitting analysis. The model of choice here is the Porod law (Eq. 4.13), summed with an Ornstein-Zernicke term (Eq 4.14). While the first term is used to describe the strong forward scattering, the latter accounts for a small contribution at high q-values. The full fitting expression, after the addition of the term accounting for the incoherent background, reads

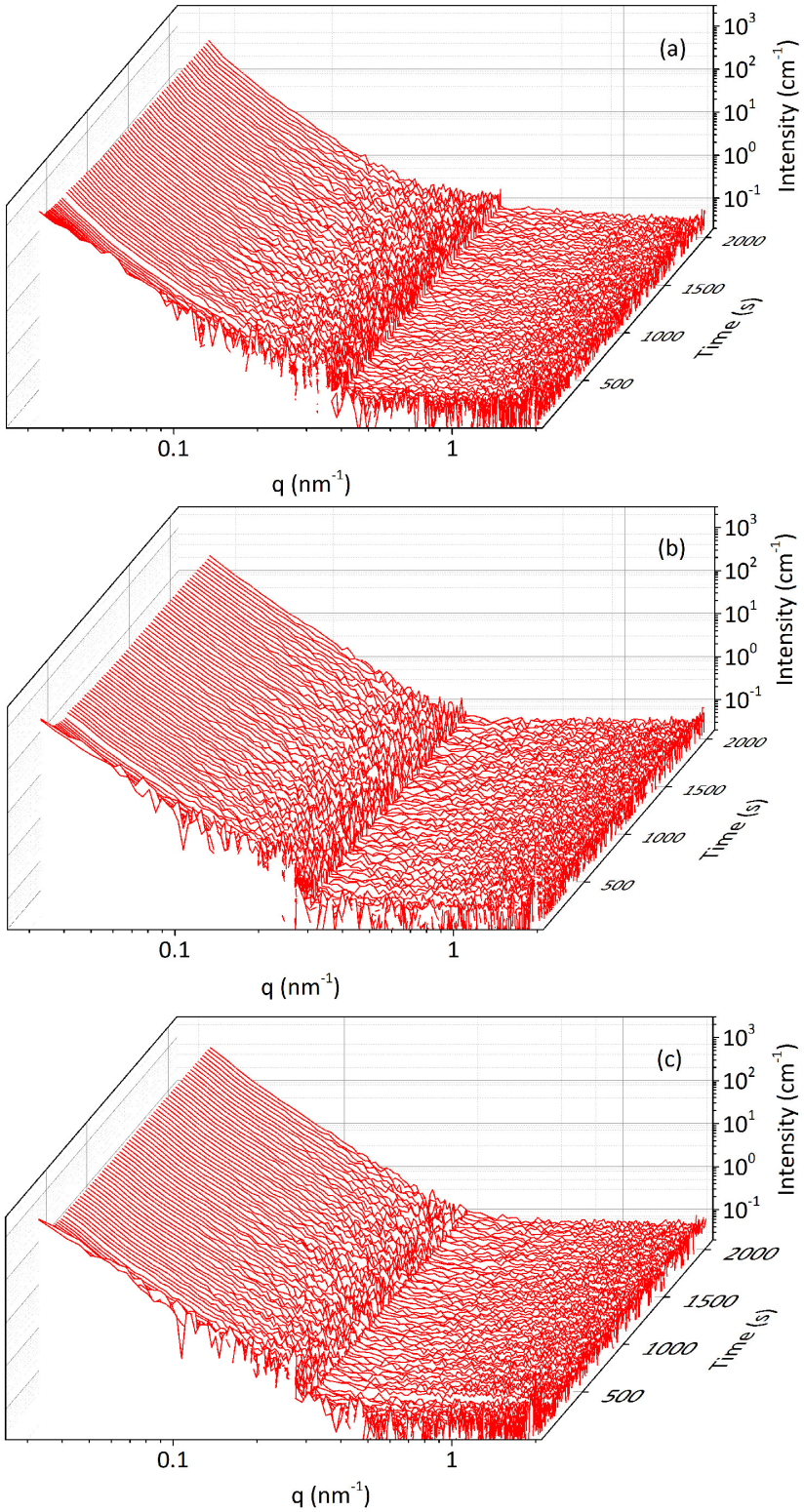

Figure 5.4.: TR-SANS curves of the PNIPAM homopolymer for all *d*-MeOD contents in dependence on time after the injection (a) 80:20 v/v D_2O:*d*MeOD at 23 °C (b) 85:15 v/v at 28 °C and (c) 90:10 v/v at 31 °C.

$$I(q) = I_{Porod}(q) + I_{OZ}(q) + I_{inc} \tag{5.1}$$

Fig. 5.5 shows representative model fits for two selected time frames (0.7 s and 2103 s after the injection). The observed deviations of the fitting curves in the intermediate region are due to the different resolutions for the two data sets (SDD 4.0 and 14.4 m). Fig. 5.6 summarizes the fitting parameters from the Porod contribution. The Porod amplitude I_P^0, (Fig. 5.6a), decreases with time for all d-MeOD contents, starting from the same initial value of 8 x 10^{-11}. The absence of units for the I_P^0 is due to the deviation of α from the nominal value of 4. In more detail, I_P^0 stays constant during the first second for all d-MeOD contents. Then it decreases during the first 6 s with the rate of this decrease being the same for all d-MeOD volume fractions, but later the rate depends on the amount of d-MeOD that is present; the more d-MeOD is present the faster the decrease. The final value is reached after ca. 200-500 s after the injection and depends on the system.

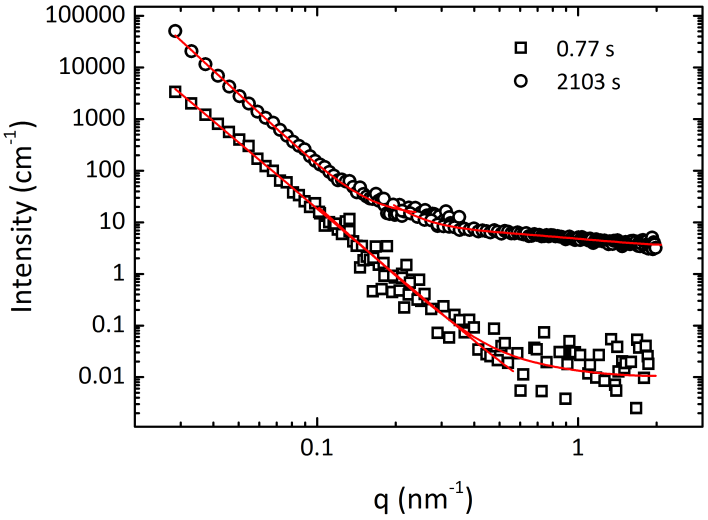

Figure 5.5.: TR-SANS on the PNIPAM solution with a mixing ratio of 80:20 v/v. Symbols: experimental data poins at the times given. Full lines: Representative model fits for the two resolutions. For clarity the curve at 2103 s after the injection is shifted by a factor of 100.

In the case of the Porod exponent α, it increases with time for all d-MeOD volume fractions (Fig. 5.6b). Initially the value is $\sim$ 4.8 and then it increases until 30 s after the injection, reaching a final value of $\sim$ 5.8 for all methanol content jumps. These values are larger than expected for spheres with a smooth surface, $\alpha = 4$ [Por51]. The origin of this observation may be a gradient of the SLD along the surface normal of the aggregates [KMS82, Rul71]. Hence, the observed increase of α means that the interfaces

become smoother; in the beginning, the aggregates still contain entrapped solvent which is expelled with time. It is safe to postulate that this happens mainly from the outer part of the aggregates. Consequently, a dense polymer layer is formed on the surface which eventually acts as a diffusive barrier for the remaining solvent molecules that reside still in the interior of the formed particles.

The fact that the exponent α is higher than the 4 makes it difficult to interpret the behaviour of I_P^0. A short discussion was presented in section 4.1.4. Unfortunately here the deviations of α make it impossible to use Eq. 4.12. A way to overcome this obstacle is to implement in the analysis model the approach by Koberstein et al. [KMS82]. According to this approach these deviations of α can be assigned to the presence of diffusion boundary layers. In detail, a modified Porod expression was used, where the unperturbed Porod law was multiplied by a factor accounting for the diffusion layer width. Nevertheless, this attempt did not give any acceptable values, not even for qualitatively good fits. Therefore it was not pursued further. Thus the behaviour of I_P^0 is only discussed qualitatively in the following.

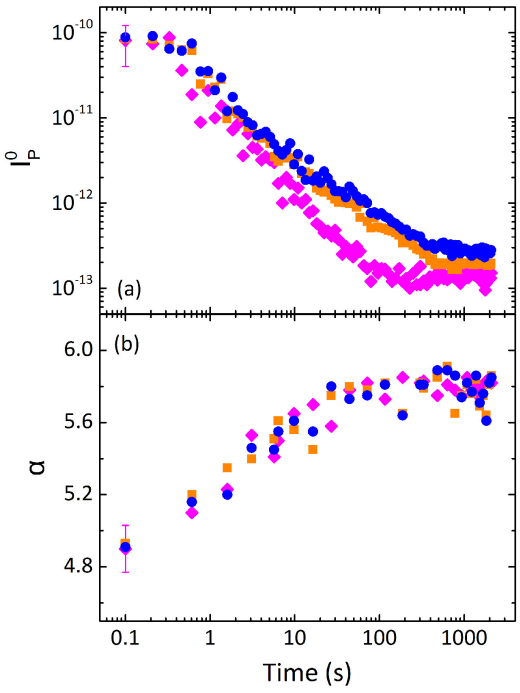

Figure 5.6.: Fitting results from the generalized Porod term: (a) the Porod intensity I_P^0 and (b) and the Porod exponent α as a function of time after injection for the mixing ratios of 90:10 v/v at 31 °C (blue circles), 85:15 v/v at 28 °C (orange squares) and 80:20 v/v at 23 °C (magenta diamonds).

The decrease of I_P^0 reflects the decrease of the specific surface of the aggregates with

time, i.e. their increase in size. Under this scope, the evolution of I_P^0 with time can be assigned to different phases of the aggregation process: In the first stage, all three samples are in a similar state, as expected, which remains stable for the first second; moreover for the following 6 s the process evolves with the same rate for all three volume fractions. Thus we can assume that in all cases the aggregation evolves similarly. Interestingly afterwards the path followed depends strongly on the content of *d*-MeOD. The aggregation process in the case of 80:20 v/v follows the same rate until 100 s after the injection and then stops growing. After the 100 s also α remains constant. Thus, during the last regime, all processes seem to have reached their final state. In contrary, the samples with 85:15 v/v and 90:10 v/v grow at a lower rate. Thus, we conclude that the higher the *d*-MeOD volume fraction, the faster the growth process. It is worth mentioning here that the observed arrest of the decrease of I_P^0 does not mean necessarily an arrest of the aggreation; it can be the result of the resolution limit of the TR-SANS set-up. We point out this fact, since there have been previous studies reporting aggregates a few hundred nm large [BDG+07] or even larger [MKPB+12] which continue growing over longer times ($\sim$5000 s) than probed here.

The results of the fits of the Ornstein-Zernicke term are presented in Fig. 5.7; the correlation length ξ and the scaling factor I_{OZ} are given as a function of time. During the first $\sim$20 s, the curves suffer from poor statistics due to the low accumulation times. Therefore no values for this time regime are given. At later times, the statistics are good enough to allow the fitting of the small contribution (i.e. shoulder-like) in the high q-region reliably. Starting from ξ, we observe a decrease from 15 nm to 1-2 nm for all three *d*-MeOD volume fractions and then, after the first $\sim$100 s, remains constant at this value (5.7b). The absolute value is in consistency with the expected values for collapsed chains in the semidilute regime. From the fact that I_{OZ} (5.7a) is finite above T_{cp}, we can conclue that the aggregates formed by collapsed PNIPAM still contain some solvent; thus inhomogeneities on the length scale of ξ are expected. The subject of PNIPAM chains partially hydrated even above the T_{cp} has found recently experimental evidence [PKS+14]. Moreover, the subsequent decrease of I_{OZ} with time means that the osmotic modulus increases; i.e. the aggregates become more compact with time. We observe that the large, polymer-rich aggregates not only increase in size, presumably by coagulation, but at the same time expel the entrapped solvent molecults, mainly from their outer part.

5.5. PS-*b*-PNIPAM diblock copolymer

The SANS curves obtained during the measurements of the PS-*b*-PNIPAM diblock copolymer are presented in Fig. 5.8. The same behaviour is observed for all three mixing ratios;

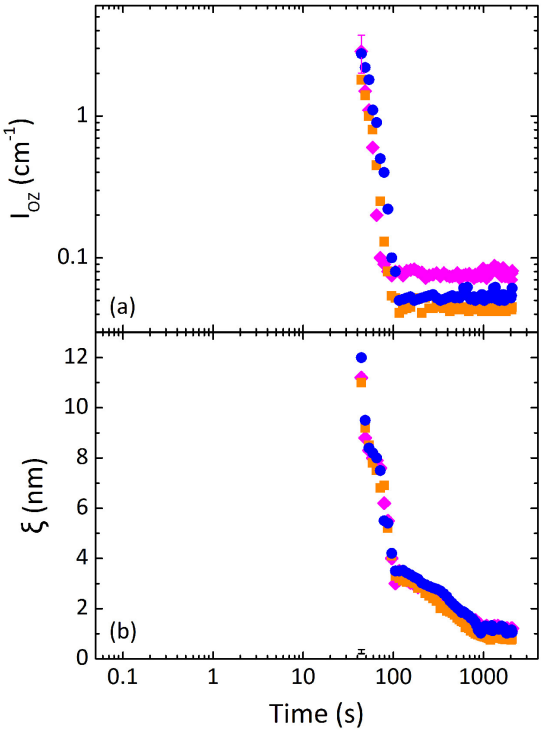

Figure 5.7.: Fitting results from the Ornstein-Zernicke term: (a) the OZ intensity I_{OZ} and (b) and the correlation length ξ as a function of time after injection for the mixing ratios of 90:10 v/v at 31 °C (blue circles), 85:15 v/v at 28 °C (orange squares) and 80:20 v/v at 23 °C (magenta diamonds).

first, the curves decay smoothly, whereas, after ∼15 s a minimum appears at $q \cong 0.15$ nm^{-1} which moves with time to lower q-values. Making an approximation based on the well known relation for monodisperse homogeneous spheres (i.e. $R \cong 4.5/q_{min}$, where q_{min} is the position of the first minimum of the sphere form factor) we obtain R ≅ 25 nm. This value is much higher than the micellar radius known from similar PS-*b*-PNIPAM diblock copolymers in the collapsed state (∼5-7 nm) [AMKBK$^+$11, TKW$^+$08b] we therefore attribute the spheres to aggregates formed by a large number of collapsed micelles.

At the end of each run, the minimum in the SANS curves is still present and has moved to q ∼0.1 nm^{-1}. Thus, the aggregate radii are of the order of R = 45-50 nm; i.e. larger than in the beginning. Nevertheless, this picture is different than the one obtained in previous SANS measurements in D_2O, where a Porod-like scattering from very large aggregates above the T_{cp} was observed [TKW$^+$08b]. Similarly,very large aggregates were also formed in solutions of PS-*b*-PNIPAM-*b*-PS in D_2O above T_{cp} [AKA$^+$10]. Hence, in the present case, the aggregates growth seems to be limited and moreover the addition of *d*-MeOD alters the aggregation path significantly compared to a temperature increase

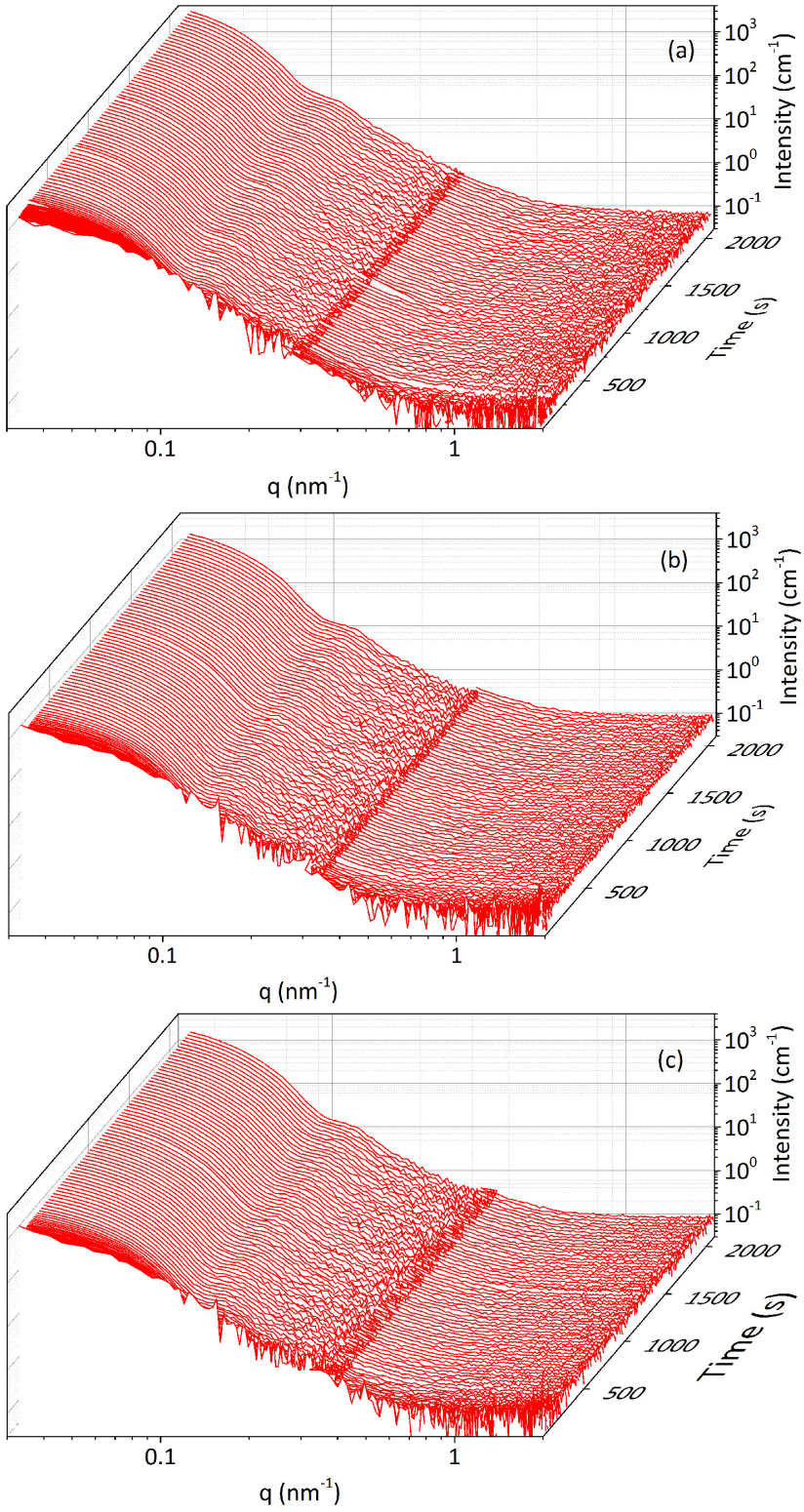

Figure 5.8.: SANS curves as a function of time for all *d*-MeOD studied: (a) 80:20 v/v D_2O/*d*-MeOD at 23 °C (b) 85:15 v/v at 27 °C and (c) 90:10 v/v at 29 °C.

above the T_{cp}. In the next step structural models were fitted to the TR-SANS curves was performed in order to extract quantitative results. Here we use two different models to account for the different states of the system. During the first regime, that extends over the first ≈50 s, we use the Guinier-Porod model (Eqs. 4.1, 4.2) together with the incoherent background. At the later stages the model describing spheres with a Gaussian size distribution (Eq. 4.3) is used, again together with the incoherent background. Here the total fitting function reads

$$I(q) = P_{sph}(q) + I_{inc}. \tag{5.2}$$

Some representative fits of the two models used here are presented for three selected time frames (at 0.7 s and 2103 s after the injections) for the 80:20 v/v mixing ratio are presented in Fig. 5.9.

Fig. 5.10 compiles the results of both fitting models for all three runs. The fitting was carried out in two steps: the first curves (until 30 s after the injection) were fitted with the Guinier-Porod model while later on the model for spheres with a Gaussian size distribution was used. To verify the validity of our approach we used both models in the intermediate regime and obtained similar values (see Fig. 5.10a). The first curves give a radius of R_g ∼15.0 ± 3.5 nm for all three runs. This value is much higher than a single collapsed micelle, therefore we assume that very soon after the mixing already some aggregates have been formed; i.e. the phase transition has occured before the first measurement. A reason for this could be the excess heat emitted upon mixing D_2O and *d*-MeOD [BMWH66]. By comparing the value of the initial aggregate radius with the radius of collapsed micelles from similar systems from the literature, the aggregation number can be estimated to be ∼15 micelles/aggregate.

Naturally, the question arises whether the micellar structure of PS-*b*-PNIPAM is sustained after the addition of the *d*-MeOD into the system. From the SANS curves on this experiment it is not possible to deduce whether the micelles stay intact upon the change of the environment. But as it will be seen in the next experimental chapter, SANS experiments on similar systems prove that the diblock copolymers indeed accommodate themselves in micelles even in a mixed solvent of D_2O/*d*-MeOD. The fact that the first stages captured in this experiment are al Nevertheless, the presence of a different solvation environment than pure D_2O is expected to influence the micellar exchange dynamics (i.e. by softening the PS core) as has been reported recently [SKZ+14]. Any influence on the exchange dynamics would be outside the observation window of the presented here experiment. The values of the Hildebrand parameters for all the components of the system studied here imply also that the PS core is not expected to dissolve in the mixed solvent of water and methanol: $\delta_{MeOH} = 14.5$ cal$^{(1/2)}$cm$^{(-3/2)}$, $\delta_{PS} = 9.13$ cal$^{(1/2)}$cm$^{(-3/2)}$ and δ_{H2O}

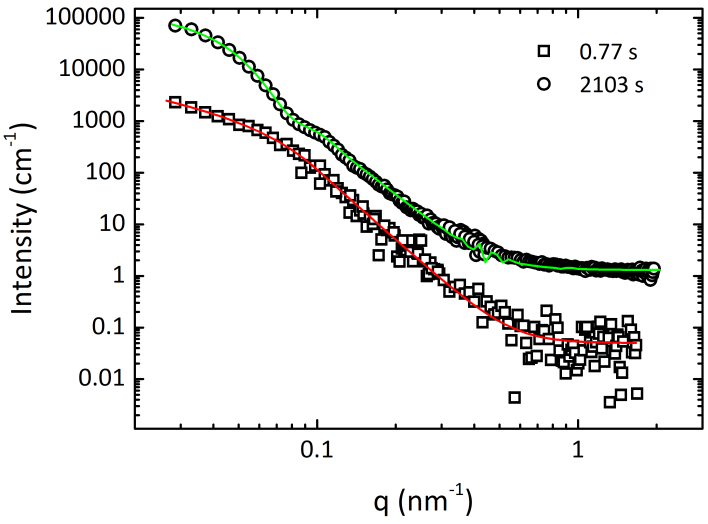

Figure 5.9.: Representative fits of the structural models to the experimental curves. The measured data points are presented with symbols while the fits with lines. The curve at 2103 s has been shifted by a factor of 20 for clarity. The red line corresponds to the Guinier-Porod model and the green line to the model describing spheres with a Gaussian size distribution.

$= 23.15\ \mathrm{cal}^{(1/2)}\mathrm{cm}^{(-3/2)}$. Apparently the Hildebrand parameter for methanol is closer to the one for PS than the one of water, still PS is not soluble in the former [Bur84].

Fig. 5.10 gives the evolution of the fitting coefficients as a function of time. The aggregate radii increase in all three cases, reaching final values of 44.14 ± 1.40 nm, 44.70 ± 1.20 nm and 49.20 ± 1.50 nm for the three respective cases of 90:10 v/v, 85:15 v/v and 80:20 v/v. Interestingly the aggregates final size depends on the methanol content; the higher the content of methanol, the larger is the final radius. Moreover, a survey over the behaviour of the three systems as a function of methanol volume fraction at the first stages shows that in the case of 80:20 v/v the aggregate growth starts earlier at ∼1 s after the injection, whereas for the two other samples after ∼5 s. The radii obtained from the two models coincide very well in the intermediate regime. Even if the Guinier-Porod model gives the R_g while the model for spheres with a Gaussian size distribution gives the average geometric radius R_{sph}, the two values are strikingly similar. For homogeneous spheres the R_g would differ from R_{sph} by a factor of $(3/5)^{1/2}$. For hollow sphere on the other hand the radius of gyration would be given through

$$R_g = \sqrt{\frac{3}{5} \times \frac{R_1^5 - R_2^5}{R_1^3 - R_2^3}} \tag{5.3}$$

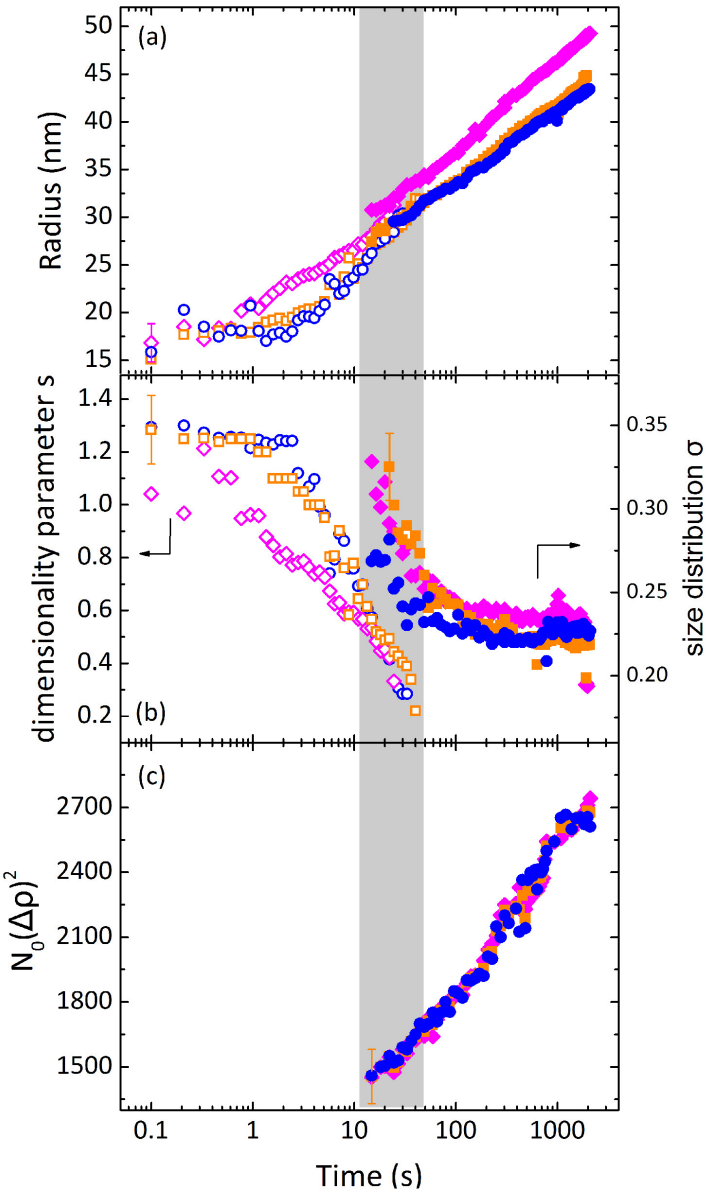

Figure 5.10.: Fitting results from the PS-*b*-PNIPAM solutions. The results are presented as a function of time after injection for all mixing ratios: 90:10 v/v at 29 °C (blue circles), 85:15 v/v at 26 °C (orange squares) and 80:20 v/v at 23 °C (magenta diamonds). With open symbols the results from the Guinier-Porod model are presented, whereas with filled symbols the results from the model for spheres with a Gaussian size distribution. The grey box indicates the time range in which both models were used. The following coefficients are presented as a function of time: (a) the radii R_g and R_{sph} from both models, (b) the dimensional parameter s from the Guinier-Porod model and the polydispersity σ of the sizes of the spheres from the Gaussian distribution, (c) the prefactor $N_0(\Delta\rho)^2$ of the Gaussian size distribution.

where R_1 and R_2 are the inner and the outer radius respectively. Thus, the more of the polymer mass is located close to the outer part of the aggregate, the closer the value of R_g to the one of R_{sph} is. Therefore it is safe to assume that the polymer mass distribution is radially inhomogeneous; i.e. the concentration of the polymer is higher closer to the surface than in the center. Similar results have been reported already in previous studies for PNIPAM [AHL$^+$05, WLZ04, MT88, JLS$^+$11] and microgels [FNFBVdlN01].

5.5.1. Aggregation pathway

As it was discussed in the Theory chapter 2.6.1, the aggregation path followed above T_{cp} is of importance in many systems of soft matter particles that become hydrophobic. Mainly regarding the deviations observed from the universal aggregation laws of RLCA and DLCA. These deviations from these laws have been observed here, and thus the need emerged to seek for the proper models to describe our results.

Recently, Stepanyan et al. [SLS$^+$12, LSS$^+$13] have developed a model for describing the aggregation of polymer particles in solution upon the rapid addition of a poor solvent. The process is termed as diffusion limited coalescence (DLC). In short, this model describes polymer particles that are solvophobic and coalesce to form compact aggregates. We employ this model to our data. The following mass conservation law is applicable

$$c_p(t)R_p^3(t) = c_{p0}R_{p0}^3 \tag{5.4}$$

where $R_p(t)$ is the time dependent particle radius and $c_p(t)$ the time dependent number concentration of aggregates; R_{p0} and c_{p0} are the initial values immediately after mixing. The following growth law is derived

$$R_p^3(t) = R_{p0}^3\left(1 + \frac{t}{\tau_D}\right) \tag{5.5}$$

where τ_D is the average life time of an aggregate during DLC, introduced initially as coalescence time τ_{cls} by Stepanyan et al. [SLS$^+$12]. It is related to c_{p0} and the viscosity of the solvent η by

$$\tau_D = \frac{3}{8}\frac{\eta}{c_{p0}k_BT} \tag{5.6}$$

where k_B is Boltzmann's constant and T the temperature. By applying Eq. 5.5 to the time-dependent radius (Fig. 5.10a) we observe that the model reproduces adequately but qualitatively the data; for all three *d*-MeOD contents the model describes first 30-40 s very well. The model captures the constant value of the radius of the aggregates at the beginning and the initial stage of the growth (Fig. 5.11); thus we can assume that the initial growth process is adequately described by the DLC of soft mesoglobules. The quantitative evaluation of the data nevertheless gives values for τ_D between 2.5 and 7.1 s. Apparently these values are orders of magnitude larger than the expected for a characteristic time of an aggregation process. Furthermore, the calculation of c_{p0} from Eq. 5.6 and taking into account the viscosities of the D_2O/*d*-MeOD mixtures [MK61] and the temperature for each mixing ratio we obtain values for c_{p0}=1.37, 1.26 and 1.13×10^{10} cm^{-3} for 90:10, 85:15 and 80:20 v/v respectively. In the next step we can use the values for the c_{p0} together with the final polymer concentrations after mixing (i.e. 19 mg/ml, 18.5 mg/ml and 18 mg/ml respectively) and the molar mass of PS-*b*-PNIPAM we can estimate the initial aggregation number to be 25×10^6, 26×10^6 and 29×10^6 chains per aggregate for the three mixing ratios respectively. In another approach we can estimate the aggregation number by using the initial aggregate volumes from their initial radii and dividing these by the molar volume of the PS-*b*-PNIPAM chain. This gives values on average of a few hundred chains/aggregate; thus much smaller than the one produced by the DLC model. A reason for this discrepancy may be seek in the fact that the first stages of the phase transition occured already inside the stopped-flow device; during the passage through the mixing chamber and the delay line. Thus a fraction of the polymer chains may have been "trapped" there, maybe by adhesion to the larger inner surface, resulting hence to a lower c_{p0} in the probed volume. To this end points also the fact that the initial aggregate radii are larger than the ones expected for single collapsed micelles.

After the first stage of the relatively fast growth, a second regime is encountered in where the aggregation process evolves slower. The same behaviour is observed also for all three mixing ratios. This kind of logarithmic kinetics has been observed previously in cases where structural transformations involve an activation energy that grows with time. Examples of such systems are glasses, granular materials etc. [BP01]. In a colloidal system, like the one discussed here, the activation energy of coagulation, in other words the height of the energy barrier, is assumed be $R(t)$ dependent. In the special case of short range repulsion, this dependence is linear according to the "chord theorem", according to which the area of short-range contact between two spheres is proportional to Rt [Isr11]. The same dependence is expected also for the potential energy as well. According to this approach the dimensionless energy can be written

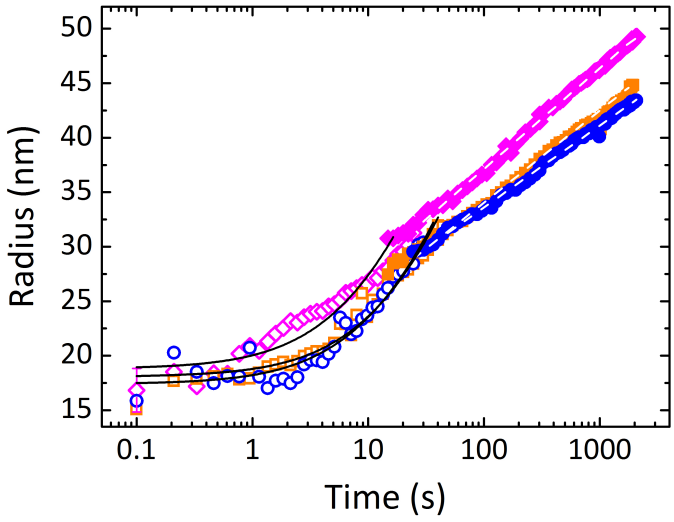

Figure 5.11.: Fits of the theoretical models on the time dependence of the aggregates size for all samples. The data for 80:20 v/v (magenta diamonds), 85:15 v/v (orange squares) and 90:10 v/v (blue circles) are presented together with the respective fits: black, full lines present the DLC model (eq. 5.5) and white, dashed lines the hindered aggregation model 5.9.

$$E_A(t) \propto R(t) = u\frac{R(t)}{R_0} \tag{5.7}$$

where $u = \epsilon/k_BT$ is the reduced activation energy of aggregation for two aggregates of size R_{p0}. What is in principle reflected in Fig. 5.7 is the collective interaction between aggregates, which requires that the aggregates are soft enough to obtain nearly spherical shape between the collisions. The transition from diffusion-limited to logarithmic aggregation takes place when the activation energy of aggregation exceeds the energy of thermal fluctuations k_BT and the aggregation probability can thus be expressed as $p_A \sim exp(-E_A)$ which drops significantly below unity. To derive the time dependence of the aggregate radius, we assume that the rate of aggregation is given by the relationship

$$\frac{\partial c_p}{\partial t} \propto -p_A c_p^2 \tag{5.8}$$

according to which the probability of aggregation decays exponentially with the aggregate radius $R(t)$; the bigger the aggregates the lower the probability that a coalescence event will happen. In the case of large aggregates the integration of Eq 5.8 gives the logarithmic time dependence as expected:

$$\frac{R(t)}{R_0} \approx \frac{1}{u} ln \left(\frac{u}{3} \frac{t}{\tau_{log}} \right) \tag{5.9}$$

where now the τ_{log} is the average time between collisions of aggregates of radius R_0 at the concentration c_{p0} in absence of coagulation and $\tau_{log} \ll \tau_D$. The whole derivation of Eq. 5.9 was made in the concept of a collaboration with Dr. Anatoly Berezkin. Detailed analysis can be found in the Appendix of [KPA+14]. By fitting Eq. 5.9 to the radii given in Fig. 5.10a for times after the initial stage growth (i.e. $>$ 15-20 s) the kinetic constants that characterise this regime can be obtained. Fitting parameters are u and τ_{log}; the values of R_0 were taken from the initial values as can be seen in Fig. 5.10a; i.e. 14.5 nm, 14.8 nm and 16.0 nm for 90:10 v/v, 85:15 v/v and 80:20 v/v respectively. The resulting parameters are presented in Table 5.1. It is observed that in all cases the energy barrier is notably higher than the thermal energy.

The comparison of the values for the different cases shows that the aggregation pathway depends on the amount of methanol present. Especially in the case of the later, logarithmic coalescence regime the characteristic logarithmic time τ_{log} decreases with increasing content of *d*-MeOD which in addition to the lower energy barrier allows the formation of aggregates with larger radii.

mixing ratio	$\tau_{\mathrm{D}}(s)$	$\tau_{\log}(ms)$	u
90 : 10	7.1 ± 0.5	5.1 ± 0.2	3.5 ± 0.2
85 : 15	6.5 ± 0.6	5.7 ± 0.2	3.3 ± 0.2
80 : 20	2.5 ± 0.4	10.1 ± 0.5	2.7 ± 0.2

Table 5.1.: The resulting kinetic constants from the two models: τ_D from the DLC model (Eq. 5.5), τ_{log} and u from the logarithmic coalescence model (Eq. 5.9)

5.6. Comparison of the two polymer systems

At this point, where the analysis of both the homopolymer and the diblock copolymer is complete, it is worth comparing the two systems. We have to mention here that the fact that the two systems have different M_w, but this does not cancel the strikingly different behaviour in the two cases.

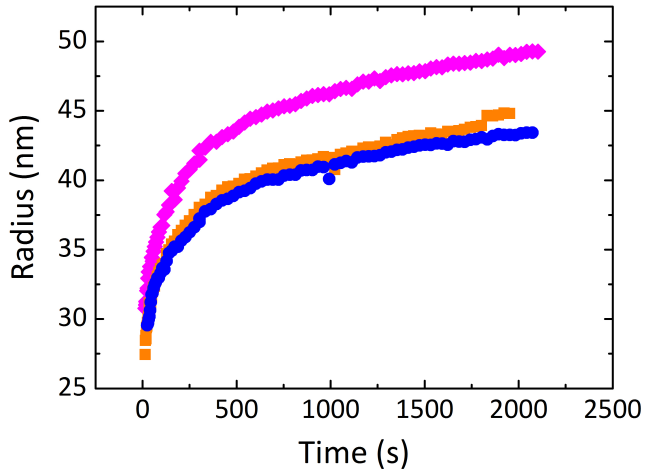

Figure 5.12.: The radius of the aggregates as a function of time on a linear scale. The data for all mixing ratios are presented: 90:10 v/v at 29 °C (blue circles), 85:15 v/v at 26 ° (orange squares) and 80:20 v/v at 23 °C (magenta diamonds).

The first point that has to be stressed is the significant difference in the sizes of the formed aggregates. For the homopolymer, already after some seconds very large aggregates are formed. They even exceed the resolution limit of the set-up. In contrary, the aggregates formed from the collapsed micelles in the solutions of the diblock copolymer are much smaller. The reason for this may be sought in the different polymer dynamics. In the case of the homopolymer the single PNIPAM chains feel no steric restrictions and thus they can more easily associate and form big aggregates. Moreover, a large aggregate can absorb a single, collapsed chain, which is still diffusing unassociated. In the case of the diblock copolymer the picture is different. Now the chains are tethered on the PS core and hence steric hindrances are present. This leads to reduced mobility of the PNIPAM chains and can be a factor that hinders the aggregation process.

The above mentioned discussion is supported also from the comparison of the final states in the two systems. Whereas the homopolymer forms very large aggregates, and relatively fast, the diblock copolymer reaches at the end a kinetically frozen state. During this stage, the radius of the aggregates is almost constant with time, as it can be seen in Fig. 5.12. The formation of mesoglobules with radius 40-50 nm is observed and is strikingly different than for the homopolymer solution. The possible factors that can create this stability have been discussed previously in this work. In order to decide here the origin of this behaviour would require further experiments (e.g. ζ-potential), which would be outside the scope of this work. Nevertheless, our results can be compared with other systems and experiments, and create the spark for future studies.

5.7. Conclusions

In this part of the work the collapse transition and the subsequent aggregation process induced upon addition by the rapid addition of *d*-MeOD to aqueous solutions (in D_2O) of PNIPAM homopolymer and of an amphiphilic PS-*b*-PNIPAM diblock copolymer are studied on a mesoscopic length scale. By means of TR-SANS, the influence of the addition of different volume fractions of *d*-MeOD on the phase separation mechanism and the subsequent mechanism of aqueous solutions of the above mentioned systems is studied. The first conclusion to be drawn is that the addition of the methanol results in a very fast collapse of the PNIPAM chains and the micellar PNIPAM shell, respectively. In both cases, the hydrophobic collapsed entities associate and form large aggregates. A summary of the observations is given in Fig. 5.13.

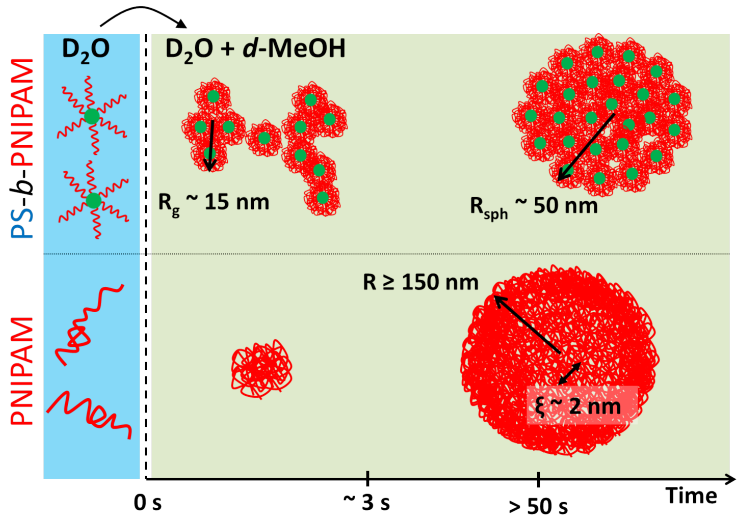

Figure 5.13.: A schematic summary of all the observed structural changes in the presented here experiment.

The structural information obtained via this approach reveals the dependence of the aggregation mechanism on the amount of methanol added. For the case of the diblock copolymer small aggregates in the range of 15 nm are present already at the beginning. Thus, we postulate that the first stages of the aggregation occurred before the solution was injected in the neutrons beam path; i.e. the phase transition has happened inside the stopped-flow device. In spite of this, the followed aggregation pathway was studied in detail. The process consists of different regimes. Initially, the size of the aggregates remains constant (during the first 1 sec), but after a certain time, which depends on the *d*-MeOD content the aggregates start to grow. During the first stages the growth follows the diffusion limited coalescence model, but with an aggregate life-time which is

orders of magnitude too high than the expected one. This reflects the complexity of the process and highlights the necessity for further studies. Interestingly, during the later stages the growth is hindered and eventually totally arrested. Here a hindered diffusion model was applied, describing the growth in the presence of an energy barrier which is predicted to be increasing with the aggregate radius. The origin of this barrier may be the presence of surface charges on the aggregates or the increasing rigidity of the aggregates. By increasing the *d*-MeOH volume fractions, the result is a lower aggregate life-time in the first regime, i.e. the diffusion limited coalescence regime, as well as in an increased time between collisions and in a decreased barrier in the hindered growth regime. Hence, the final aggregate size increases with the content of *d*-MeOH.

Both systems form aggregates that become more polymer-rich with time; a dense skin of highly collapsed polymer chains is created in the outer part of the aggregate. At the same time some solvent molecules are trapped close to the center of these aggregates. A reason for this could be the fact that solvent molecules close to the surface diffuse faster to escape the densification of the polymer aggreagates; this is not the case for the solvent molecules close to the center. This way a dense skin is formed which acts as a diffusive barrier not easily permeable for the remaining solvent molecules. Differences between the two systems have been observed, and discussed briefly in the previous paragraph.

As concluding point, the results presented in this chapter highlight the strength of time-resolved measurements, especially regarding aggregation phenomena. The access to this type of data, together with the employment of theoretical models, allows us to get a detailed insight into the evolution of the aggregates growth with time and extract quantitative information. The combination of the information presented in literature, mainly obtained by static measurements, with our results, obtained by kinetic studies, can add new insights to the ongoing, vivid discussion.

6. Temperature jumps

In the previous chapter, the influence of the addition of different volume fractions of methanol to an aqueous solution of a PS-*b*-PNIPAM diblock copolymer was studied. We followed the aggregation by means of TR-SANS and different regimes were identified. In the present chapter we wish to follow a different thermodynamic path to induce the phase separation: by increasing rapidly the temperature, i.e. by performing temperature jumps. This differentiation to the previous approach aims to resolve the first stages of the phase transition, and hopefully, to resolve also the existence of swollen micelles below T_{cp}. Here, the selected polymer is a P(S-d_8)-*b*-PNIPAM amphiphilic diblock copolymer and was predissolved in mixed solvents of D_2O with *d*-MeOD,*d*-EtOD and *d*-DMK (*d*-MeOD, *d*-EtOD and *d*-DMK stand for fully deuterated methanol, ethanol and acetone, respectively). The selection is done with respect to the molar volume of the cononsolvents, since it has been shown that the increase of the molar volume decreases stronger the T_{cp} [CF02]. A sample in pure D_2O is also studied, to act as reference. Based on this plan, the aim is to study the extent to which the solvation environment affects the phase transition, and even more importantly, the aggregation kinetics. The latter expectation is enhanced by the findings presented in chapter 5. The chapter is structured as follows: firstly, the strategy of our experiment will be presented and will followed by the experimental section, where information about the materials, the experimental set-up and the realization of the experiment is given. Then, in the main part of the chapter, the TR-SANS data are presented, together with the respective analysis. The next part elucidates the aggregation kinetics above the T_{cp} and, within the framework of the reversible association model [ZCBB11,ZCB13], offers an insight on the molecular interactions that govern the process. The results are summarized in the last section of this chapter.

6.1. Strategy

To address the question of how the system under investigation behaves under different solvation conditions, three different alcohols are chosen as cononsolvents. Namely methanol, ethanol and aceton are mixed with water at a concentration of 5% mol. The use of molar fraction as a unit for the mixing is based on "offering" to the system the same amount of

alcohol molecules, in order to specify the same conditions in the microscopic length scale. Also a sample in pure water is studied, as a reference. All solvents are fully deuterated. The system of choice here is an amphiphilic diblock copolymer P(S-d_8)$_{11}$-*b*-PNIPAM$_{431}$ with $M_{w,P(S-d_8)}$=1600 g/mol and $M_{w,PNIPAM}$=48800 g/mol, synthesized by RAFT polymerization [BKGL$^+$10]. The reasoning for choosing a diblock copolymer, instead of a PNIPAM homopolymer, is that we aim in elucidating the aggregation process as detailed as possible, which requires high time resolution. We have proven in the previous chapter that the aggregation of a homopolymer evolves much faster than of a diblock copolymer, so the use of a homopolymer may hinder the detailed study of the aggregation process with a sufficient resolution. In any case, the micellar solution of P(S-d_8)-*b*-PNIPAM can be regarded as a dispersion of responsive colloidal particles and obtaining information for such a system can be linked to different systems (e.g. nanoparticles coated by PNIPAM chains). The selected polymer concentration was 30 mg/ml, high above the expected CMC in D_2O [AMKBK$^+$11]. The use of deuterated solvents and deuterated PS ensures the ability to focus on the PNIPAM shell, due to matching the SLD values of the surrounding solvent with the one of micellar core. The phase transition is induced by the rapid increase of the temperature (i.e. temperature jump) and the evolution of the aggregation process is studied by TR-SANS. The aim here is to resolve the influence of the solvation environment on the PNIPAM conformation in the swollen state of the micelles, as well as the transition to hydrophobic aggregates and their subsequent growth with time. Therefore we follow a different path than in the previous chapter, here we choose to induce the phase separation by a temperature jump. We aim to trigger a slower phase separation than in the previous experiment, and thus to extract more detailed information, especially for the early stages of the aggregation.

6.2. Experimental set-up

The sample preparation was done as follows. First, the mixed solvent was prepared at a concentration of 5-% mole of deuterated alcohol and was left to equilibrate for 24 hours. After that, the polymer was dissolved in the mixed solvent at a concentration of 30 mg/ml. The samples were left to equilibrate at 5 °C for a week, prior to the beamtime. Special precautions were taken to avoid the evaporation of the highly volatile alcohols. The TR-SANS experiments presented in this chapter were performed at the high-flux SANS instrument D22 at ILL, in Grenoble, France. The temperature jumps were realized by using a stopped flow instrument Biologic SFM-300, coupled with a custom made sample holder. The reservoir (i.e. the stopped flow instrument) and the sample cell were connected via a short plastic tube. Fig. 6.1a presents a photo of the custom

set-up. The two components, the stopped flow reservoir and the sample holder, were kept at different temperatures by using two different thermobaths; i.e. the initial and the target temperature, respectively. In all cases, the initial temperature was 3 K below the respective T_{cp} and the target temperature 2 K above. This way, the conditions of the different jumps were kept similar. Prior to the beamtime (ex-situ), the temperature inside the sample holder was calibrated by using a thermosensor (i.e. a negative temperature coefficient NTC thermistor PB5-43-SD4). In this way, a temperature profile was obtained as a function of the time and thus the exact time at which the sample reached the T_{cp} could be detected. The temperature profiles were then compared with the SANS data to check the mutual consistency and the two pictures showed very similar behaviour. The cuvettes used here are flow circulation cells (Hellma 137-QS) with a nominal light path (thickness) of 1 mm. The sample was mounted in the reservoir and left to equilibrate at T_{cp} - 3 K for 10 min before the start of the measurement. The jump was then performed by injecting a total volume of $\sim$ 1 ml from the reservoir into the preheated sample cell. Hence we ensured that the volume of the cell (260 μl) was filled completely. At the end of the injection, a transistor-transistor logic (TTL) signal started the data acquisition. Visual inspection revealed a turbid solution in the cuvette. After each jump the sample cell was replaced with a clean one for the next measurement. The connecting tube was also replaced with a clean one. Thus the contamination of the next measurement by residual aggregates was excluded.

In order to emphasize in the first stages of the phase separation, we choose a time profile that focuses on this regime. In more detail, the first image was taken 0.2 s after the injection. Then the acquisition time was increased logarithmically by a factor of 1.05 until it reached 15 s per frame. This first part lasted in total $\sim$ 5 min. For the remaining $\sim$ 20 min the acquisition time was constant at 15 s per frame. To increase statistics and improve reliability of the approach, each jump was repeated twice for the SDD of 4.0 m and thrice for the SDD of 14.4 m. In all cases, the azimuthally averaged intensity curves did not show systematic differences and were averaged.

6.3. Phase diagram

The T_{cp} values for all samples were determined prior to the SANS beamtime by means of a thermobath and visual inspection. The use of the turbidimetry device used in Chapter 5.3 was not possible, due to inhomogeneous phase separation throughout the volume of the sample cell. Therefore a bath of toluene, in which a glass cuvette containing the polymer solution was inserted, thermally equilibrated with a precision of 0.2 K, was used and by visual inspection T_{cp} was marked. The values of the T_{cp} are given in Table 6.1, together

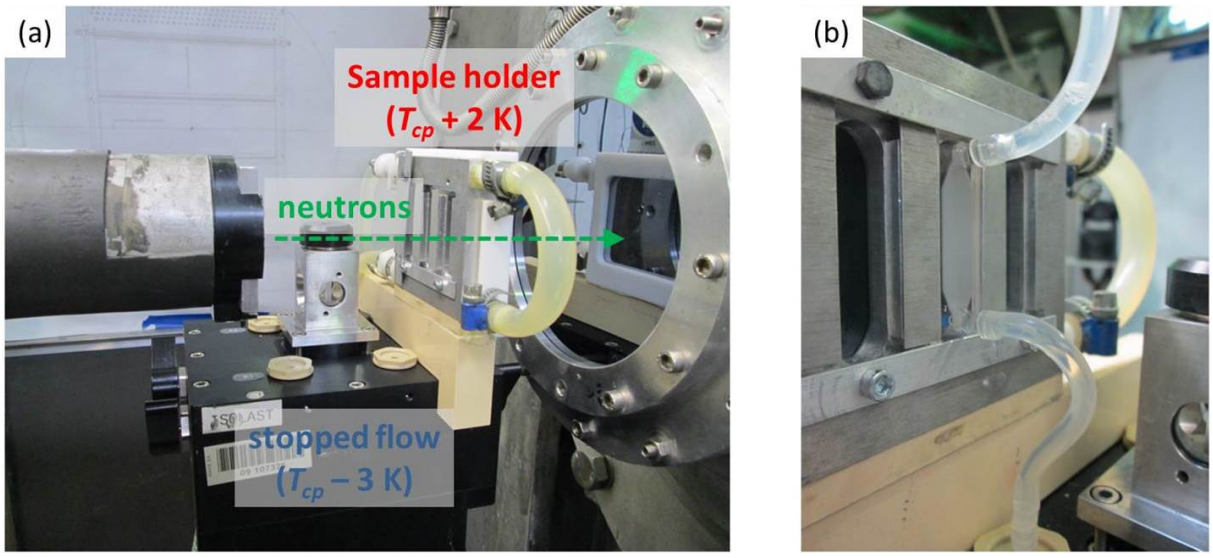

Figure 6.1.: Photographs of the actual experimental set-up: (a) The customized sample holder mounted on the stopped flow device. The respective temperatures, as well as the neutron beam path, are presented; (b) At the end of an actual measurement, we observe the solution to be turbid in the cuvette, but transparent in the tubes, thus the phase separation occured only in the probed volume.

with the ratios of the molar volumes of the different solvent species. The absolute values of molar volumes are given in Table 6.1. The selection is done in this way, so the influence of the molar volume of the cononsolvent can be studied as a function of the ratio of the molar volumes $V_{m,alcohol}/V_{m,D_2O}$. Fig. 6.2 presents the values of T_{cp} for all samples as a function of the ratio $V_{m,alcohol}/V_{m,D_2O}$. We observe a decrease of the critical temperature as the molar volume of the cononsolvent increases, a behaviour that is expected [CF02].

solvent	T_{cp} (°C)	$V_{m,alcohol}$ (cm^3/mol)	$V_{m,alcohol}/V_{m,D_2O}$	viscosity (mPa s)
D_2O	30.0 ± 0.2	18.2	-	0.931
D_2O:*d*-MeOD	28.0 ± 0.2	40.9	2.2	0.952*
D_2O:*d*-EtOD	27.0 ± 0.2	57.8	3.2	1.01*
D_2O:*d*-DMK	26.0 ± 0.2	73.4	4	0.993*

Table 6.1.: T_{cp} for the P(S-d_8)$_{11}$-*b*-PNIPAM$_{431}$ solutions in the different mixed solvents and the ratios of the molar volumes for the respective mixed solvents. (*) the viscosities of the mixed solvents were calculated by using the viscosities of the pure solvents and the Refutas equation. [Map00]

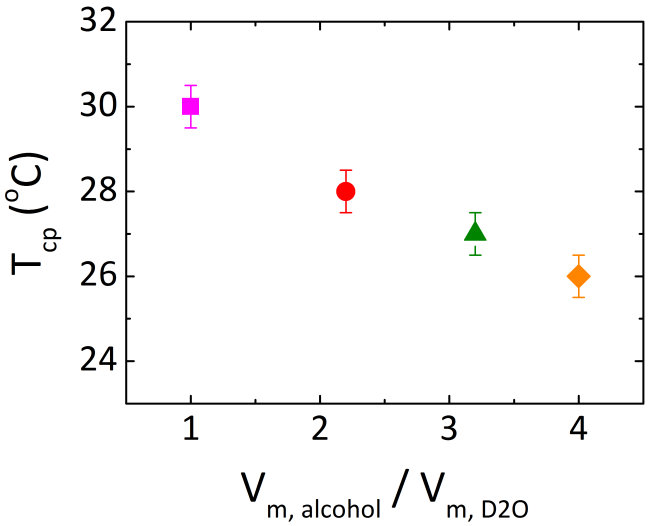

Figure 6.2.: The T_{cp} values for all solutions as a function of the ratio of the volume of the two components: magenta square for pure D_2O, red circle for D_2O:*d*-MeOD, green triangle for D_2O:*d*-EtOD, orange diamond for D_2O:*d*-DMK

6.4. TR-SANS

6.4.1. P(S-d_8)-*b*-PNIPAM in D_2O

First the data obtained for P(S-d_8)$_{11}$-*b*-PNIPAM$_{431}$ in pure D_2O for the jump from 27 °C to 32 °C will be presented. Fig. 6.3 shows the sum of the TR-SANS measurements for this sample. This type of plot presents the scattered intensity $I(q)$ as a function of q for the whole time range probed. Three regimes can be distinguished, which are depicted by different colors on the graph. Regime I (blue curves) shows scattering from swollen micelles. As soon as the temperature of the sample reaches T_{cp} (see the inset of Fig. 6.3), regime II sets in (red curves). The micellar core collapses, the micelles are now hydrophobic and they aggregate with time. This is indicated by the systematic increase of the forward scattering, which is due to the presence of larger scattering objects in the solution. During this regime the size of the aggregates is small enough to be resolved by our set-up. After a certain time, the size of the aggregates exceeds the resolution of our set-up. Thus, in regime III (green curves) the curves are characterized by strong forward, Porod like scattering; an indication of very large aggregates. It is worth mentioning here that the transition time from regime I to regime II, i.e. from swollen micelles to collapsed micelles that aggregate, is in very good agreement with the temperature profile obtained ex-situ.

In the next step structural models will be used to extract quantitative information from

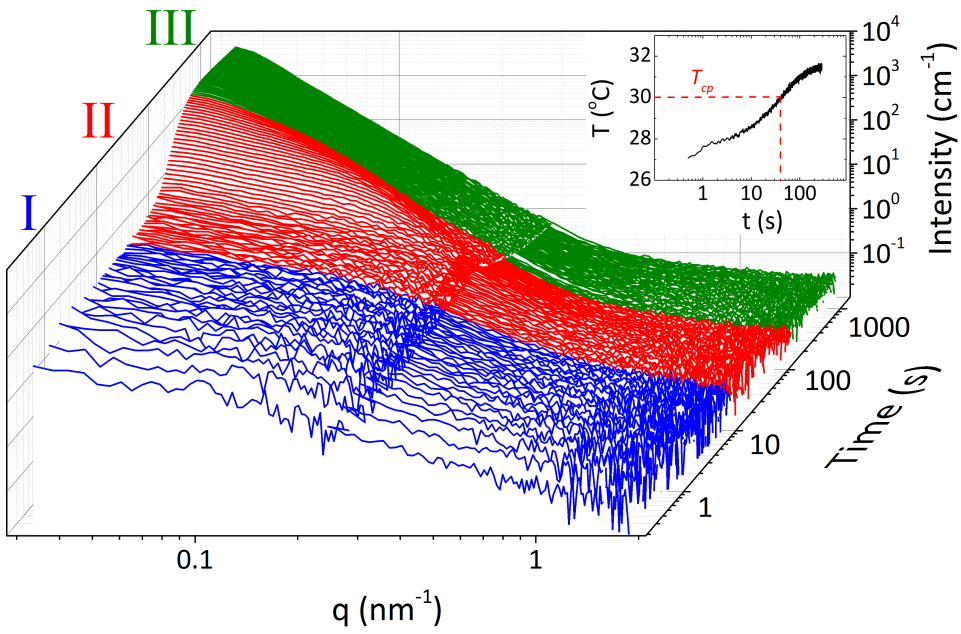

Figure 6.3.: TR-SANS curves for the temperature jump from 27 °C to 32 °C for the sample in D_2O. The scattered intensity is presented as a function of the q for the whole time probed. Different regimes are distinguished. The inset presents the temperature profile obtained ex-situ.

the scattering curves. Different models are required for the different states of the system. Below T_{cp} (regime I) the swollen micelles are modelled by a form factor for core-shell micelles (Eq. 4.6) together with an Ornstein-Zernicke term (Eq 4.14) to account for the density fluctuations within the swollen micellar shell. Thus the final fitting function reads

$$I(q) = P_{mic}(q) + I_{OZ} + I_{bkg}. \tag{6.1}$$

Above T_{cp} (regime II), the generalized Guinier-Porod model (Eqs. 4.1, 4.2) is used to resolve the size of the aggregates that are formed and to follow the increase of their size with time. Moreover, this model allows monitoring the shape of the scattering objects, thus any changes regarding the shape can also be detected. For regime III, a generalized expression of the Porod law (Eq. 4.13) was used, together with the Ornstein-Zernicke term (Eq. 4.14); the later was required to capture the small shoulder on the high q-regime (see Fig. 6.4). We assign this small shoulder to the presence of trapped solvent molecules within the large aggregates, that give rise to density fluctuations. So, the final fitting function is

$$I(q) = I_{Porod}(q) + I_{OZ} + I_{bkg}. \tag{6.2}$$

Fig. 6.4 compiles representative fits for the three different regimes. Of interest to note here is the behaviour of the red curve; an obvious deviation from the expected behaviour of a perfect sphere is observed in the low q-regime. This deviation created the need to use the Guinier-Porod model, that describes also particles with different shapes, instead of a model that describes purely spherical particles. This was not the case in the other three samples, but for sake of consistency the same model was used in this regime for all four solutions. As it was discussed in chapter 4.1.1, this model can also describe spherical particles.

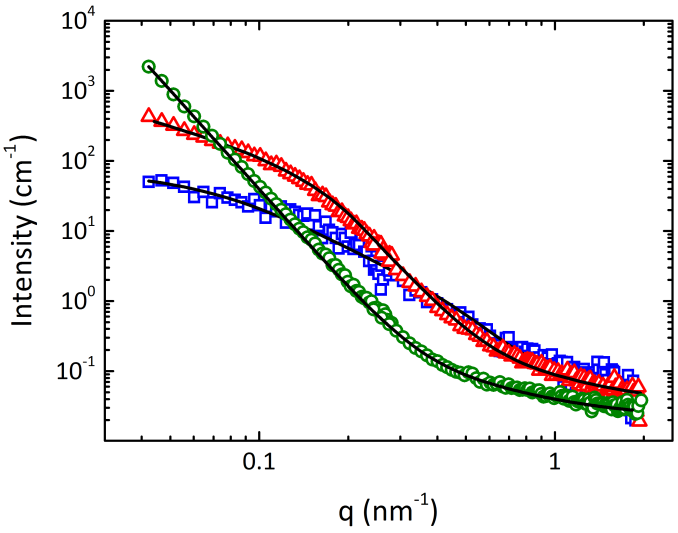

Figure 6.4.: Representative fits at different time frames of the different regimes: blue squares at 14.3 s, red triangles at 70.7 s and green circles at 1500 s after the injection. The lines present the respective fits. See text for details.

The coefficients from the different models are presented as a function of time in Fig. 6.5. Starting from regime I (below T_{cp}) the r_{mic} and the r_{core} are given (Fig. 6.5a). r_{core} was kept constant, since P(S-d_8), that consists the core, is not expected to swell in water. The value of 2.7 nm was found by performing fits on the curves with good statistics (i.e. after 10 s). The fits were redone by keeping r_{core} constant.r_{mic} slightly increases as T_{cp} is approached. The polydispersity was always 0.5-0.6 and will not be discussed further here. The slight increase of r_{mic} may act as an evidence of the gradual change of the temperature and the proximity of the phase transition. As soon as T_{cp} is reached, regime II starts and the micellar core collapses and the small, hydrophobic, collapsed micelles start to aggregate. This is monitored by the radius of the aggregates r_{agg} (Fig. 6.5a) which increases with time from 5.6 nm to 35 nm. During the same time the prefactor I_G^0 (Fig. 6.5b) also increases, reflecting the increase of the number of the existing aggregates.

From the same model the dimensionality parameter is obtained (Fig. 6.5c) and decreases from 1.2 down to 0.2; this reflects the formation of more spherical aggregates with time.

The requirement for using the Guinier-Porod model instead of a model describing purely spherical particles (e.g. spheres with Gaussian size distribution or simplified sphere form factor) originates from a small upturn of the SANS curves (see Fig. 6.4, red triangles). This may reflect the presence of elongated aggregates (non-spherical). The decrease of the dimensionality parameter, that captures the shape of the particles, from 1.2 (i.e. rods) to 0.2 (i.e. almost spheres) indicates that with time the particles become spherical. This observation is expected for aggregating particles of soft matter, since they may be able to structurally reorganize, and moreover is in agreement with the results presented in the previous chapter. For sake of clarity we should mention here that this behaviour may originate also from the relatively long measuring times, in comparison to the other solutions. Due to the fact that T_{cp} was reached later in the case of D_2O, the acquisition time profile has progressed significantly and therefore, each frame averages over a relatively long period of time. This may result in the observed upturn in the low q-region. As a general comment, we tried also to analyse the curves in this regime with other models (e.g. fractals, cylinders), but no good fits were obtained. Moreover, for the other solutions we do not observing a similar behaviour, but for the sake of consistency we used the Guinier-Porod model for all solutions.

In regime III, when the size of the aggregates exceeds the resolution limit of the set-up, the decrease of I_P^0 with time reflects the further increase of the aggregates size (Fig. 6.5d). This is an indirect way to probe the evolution of the size, since the I_P^0 is related to the specific surface (S/V) of the aggregates. The fact that here a generalized Porod model is used (Eq 4.13), where the power law of 4 has been replaced by a free variable α does not allow the use of the direct proportionality between I_P^0 and S/V (see paragraph 4.1.4 for details). Nevertheless, we can qualitatively follow the decrease of S/V, hence we can deduce that the aggregates continue to grow. In Fig. 6.5e the values of α are presented. The results from both the Guinier-Porod model and the Porod law are compiled. In regime II we observe an increase of α from 4.4 to 5.7. Values above 4 are expected for aggregates with a SLD gradient along the surface normal. The further increase can be assigned to the increase of this gradient with time. After reaching the highest value, α relaxes to a value $\sim$5.5 and stays constant throughout regime III. Hence, we can describe with this observation the formation of aggregates with a surface that becomes more polymer-rich with time. This could be explained by the continuous release of solvent molecules from the outer part of the aggregates volume. After a certain point this process reaches an equilibrium state and the reason for that could be the formation of a dense polymer skin

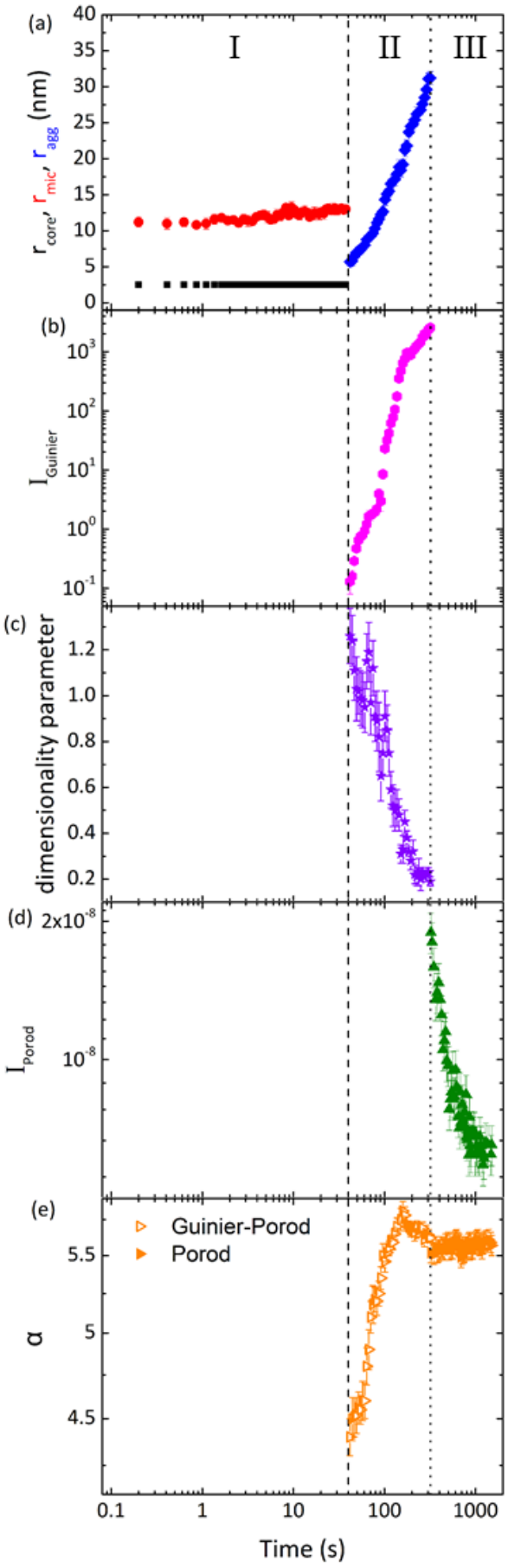

Figure 6.5: TR-SANS results. Fit parameters are presented for P(S-d$_8$)$_{11}$-*b*-PNIPAM$_{431}$ in D_2O as a function of time after the injection: (a) the radius of the micelles, r_{mic}, (red circles) and the radius of the core, r_{core}, (black squares) from the form factor for core shell micelles below T_{cp} and the radius of the aggregates, r_{agg}, (blue diamonds) above the T_{cp} from the Guinier-Porod model; (b) the prefactor of the Guinier Porod model, I_G^0, (magenta polygons); (c) the dimensionality parameter (violet stars) from the same model; (d) from the Porod law the Porod intensity, I_P^0, (green triangles); (e) the values for the Porod exponent α from both the Guinier-Porod model (orange open right triangles) and the Porod law (orange solid right triangles). The dashed line marks the time that the T_{cp} was reached. The dotted line marks the transition between regime II and III. Whereas the former was found by comparing the ex-situ obtained temperature profiles with the behaviour of the SANS curves, for the latter the point was taken at which the forward scattering was starting to dominate the SANS signal.

that acts as a diffusive barrier, which prohibits the continuous release of solvent molecules from the inner part of the aggregate.

6.4.2. P(S-d_8)-*b*-PNIPAM in D_2O:*d*-MeOD

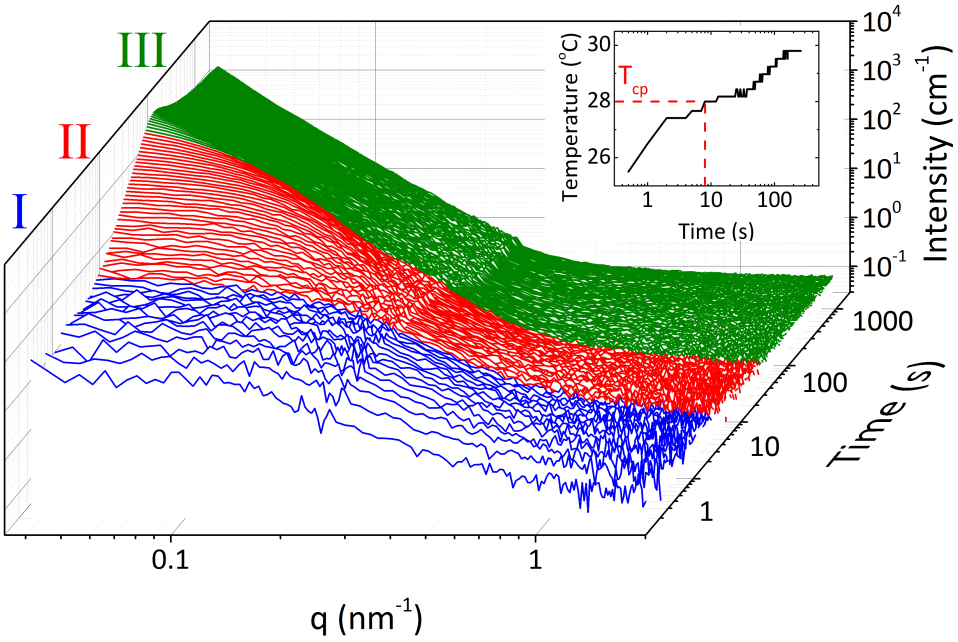

Figure 6.6.: TR-SANS curves for the temperature jump from 25 °C to 30 °C for P(S-d_8)$_{11}$-*b*-PNIPAM$_{431}$ in D_2O:*d*-MeOD 95:5 mol/mol. The scattered intensity $I(q)$ is presented as a function of the q for the whole time probed. Three different regimes are distinguished. The inset presents the temperature profile obtained ex-situ.

In this second part, the results for the temperature jump for the P(S-d_8)-*b*-PNIPAM in D_2O:*d*-MeOD 95:5 mol/mol from 25 °C to 30 °C will be presented. All SANS curves are summarized in Fig. 6.6. As before, three different regimes can be distinguished and the general behaviour is similar to the previous case. The important points or differences to be highlighted are three. First of all, below T_{cp} scattering from swollen micelles is observed, hence the assumption in chapter 5 that micelles persist even in mixtures of D_2O and *d*-MeOD is valid. Any influence on the exchange dynamics cannot be excluded, but it will be outside the observation window of our experiment [SKZ+14]. The second point is the observation that T_{cp} is crossed earlier in the mixed solvents D_2O:*d*-MeOD, than in pure D_2O. The origin of this is not still clear. Maybe it is correlated to the proximity of T_{cp} to the room temperature. The third observation regards the micellar radius. The increase of r_{mic} in D_2O:*d*-MeOD as T_{cp} is approached is stronger than in pure D_2O. This

already acts as a sign of the influence of the solvation environment on the PNIPAM chain conformation. In the next step the results of the fitting process will be presented.

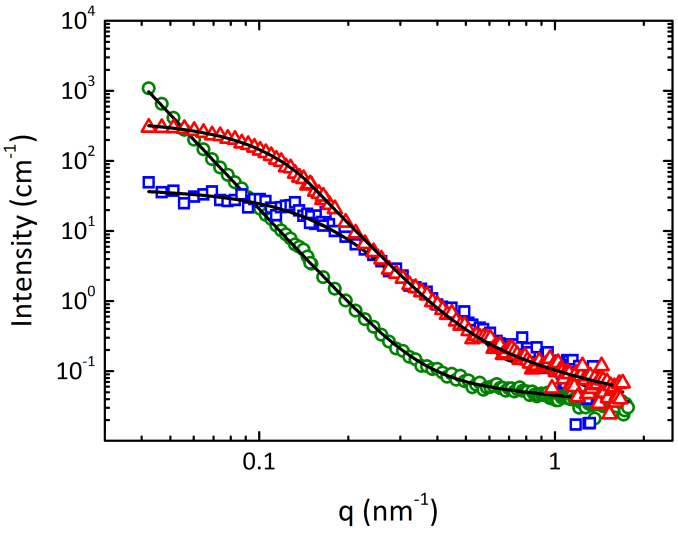

Figure 6.7.: Representative fits at different time frames of the different regimes for the sample in P(S-d_8)$_{11}$-*b*-PNIPAM$_{431}$ in D_2O:*d*-MeOD 95:5 mol / mol: blue squares at 1.1 s, red triangles at 13.3 s and green circles at 1500 s after the injection. The lines present the respective fits. See text for details.

The fitting models employed here, are similar to the ones used in the previous paragraph. The only difference is the dimensionality parameter of the Guinier-Porod model, used just above T_{cp}. Here there is no need to account for non-spherical particles, since the small upturn present in the data for D_2O is not observed (see Fig. 6.7). Thus, the dimensionality parameter was kept constant at 0. Fits with this parameter as free variable were always giving values very close to 0. Fig. 6.7 compiles some representative fits from the three regimes.

A qualitative comparison between Figs. 6.4 and 6.7 reveals the difference in the behaviour in the small q-regime. The resulting parameters from the fits are summarized in Fig. 6.8. The size of the micelles is presented in Fig. 6.8a via the r_{mic}. As before, the r_{core} was kept constant. Similar to the case of D_2O, r_{mic} increases as the T_{cp} is approached. The increase here is stronger than in pure D_2O (36% and 14% respectively). After the T_{cp} is reached, the hydrophobic, collapsed micelles associate into bigger aggregates with time, starting from a size of 15.8 nm and reaching 40.5 nm at the end of this regime II. At the same time the prefactor of the model I_G^0 (Fig. 6.8b) increases with time, reflecting the increase of the number of aggregates. At the end of this regime, the size of the aggregates

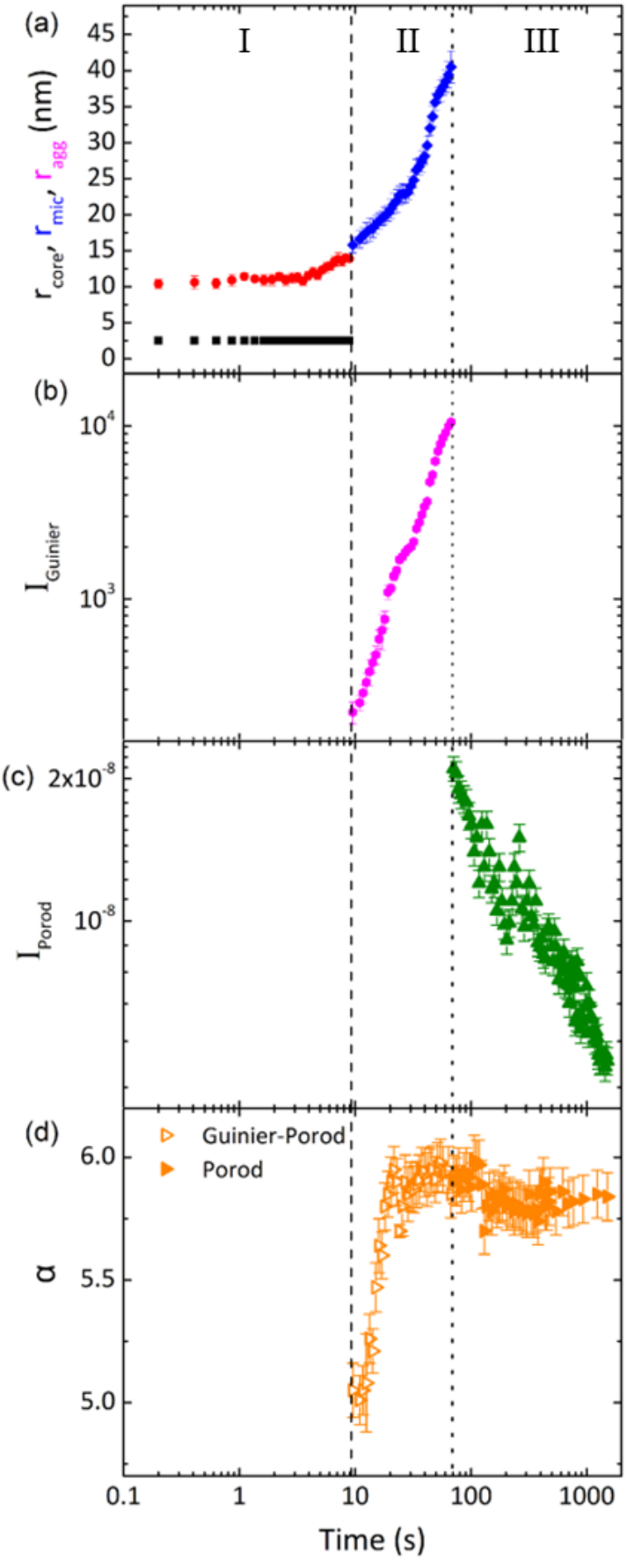

Figure 6.8: TR-SANS results. Fit parameters for P(S-d_8)$_{11}$-*b*-PNIPAM$_{431}$ in D_2O:*d*-MeOD 95:5 mol/mol as a function of time after the injection: (a) the radius of the micelles r_{mic} (red circles) and the radius of the core r_{core} (black squares) from the form factor for core shell micelles and the radius of the aggregates r_{agg} (blue diamonds) above the T_{cp} from the Guinier-Porod model; (b) the prefactor of the Guinier Porod model I_G^0 (magenta polygons); (c) from the Porod law the Porod intensity I_P^0 (green triangles); (d) the values for the Porod exponent α from both the Guinier-Porod model (orange open right triangles) and the Porod law (orange solid right triangles). The dashed line presents the time that the T_{cp} was reached. The dotted line presents the transition between the second and the third regime. Whereas the former was found by comparing the ex-situ obtained temperature profiles with the behaviour of the SANS curves, for the latter the point was taken at which the forward scattering was starting to dominate the SANS signal.

exceeds the resolution of the set up and thus in the third regime the further increase of the aggregates size is followed via the evolution of the I_P^0 (Fig. 6.8c). In the last block of the Fig. 6.8 the values of α from both the Guinier-Porod and the Porod law are presented. Also here values higher than 4 are observed at the beginning (i.e. 5.01) and they increase further with time reaching values close to 5.9. We assign this behaviour to the formation and the evolution with time of a SLD gradient along the surface normal of the aggregates. During regime III the values remain almost constant.

6.4.3. P(S-d_8)-*b*-PNIPAM in D_2O:*d*-EtOD

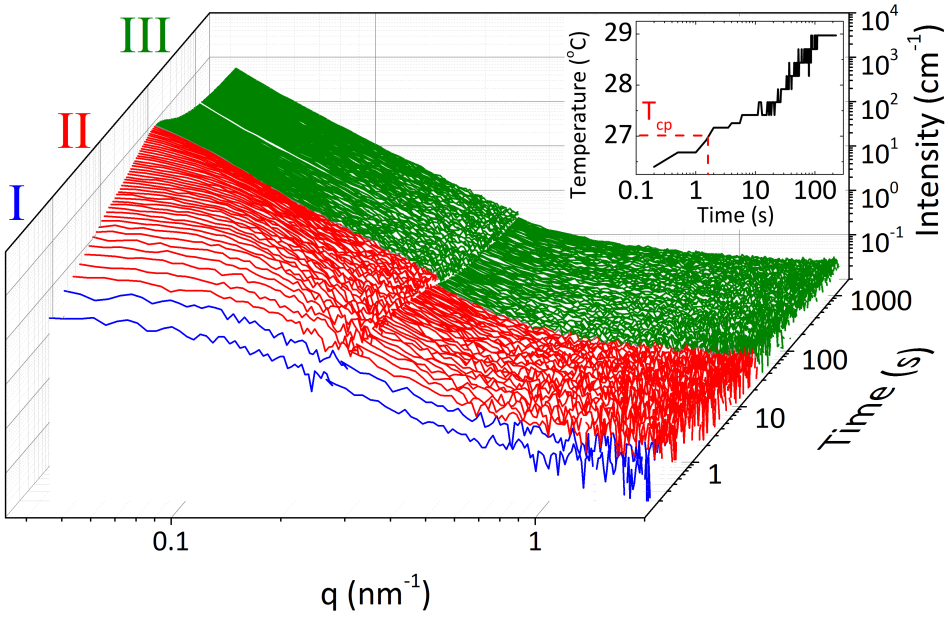

Figure 6.9.: TR-SANS curves for the temperature jump from 24 °C to 29 °C for P(S-d_8)$_{11}$-*b*-PNIPAM$_{431}$ in D_2O:*d*-EtOD 95:5 mol/mol. The scattered intensity is presented as a function of the q for the whole time probed. Different regimes are distinguished. The inset presents the temperature profile obtained ex-situ.

In this third part, the results for the temperature jump from 24 °C to 29 °C for P(S-d_8)$_{11}$-*b*-PNIPAM$_{431}$ in D_2O:*d*-EtOD 95:5 mol/mol will be presented. The summary of the SANS curves is presented in Fig. 6.9. Similar to the previous cases, three different regimes are distinguished, corresponding to different states of the system. A qualitative comparison between the three so far discussed systems (see Figs. 6.3, 6.6, 6.9) shows a systematic shift of the different regimes in the time-axis. In other words the T_{cp} is reached earlier as we move from pure D_2O to mixture of D_2O:*d*-MeOD and then to mixture of

D_2O:*d*-EtOD. This is a pure consequence of the fact that the T_{cp} of the systems decrease and get closer to the ambient temperature. Another observation of interest here is that, in all three systems presented until now, micelles are present. Thus the assumption made also in paragraph 5, that in mixtures of D_2O:*d*-MeOD the micellar structure remains intact, holds true also for mixed solvents of D_2O:*d*-EtOD.

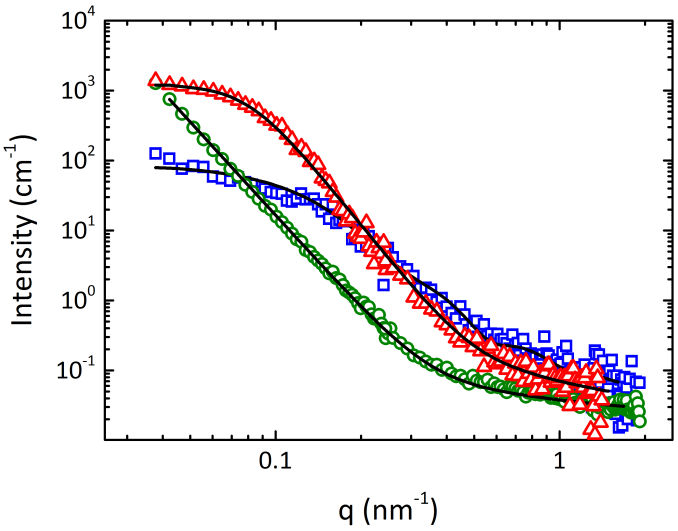

Figure 6.10.: Representative fits at different time frames of the different regimes for P(S-d_8)$_{11}$-*b*-PNIPAM$_{431}$ in D_2O:*d*-EtOD 95:5 mol/mol: blue squares at 0.1 s, red triangles at 4.3 s and green cirles at 1006 s after the injection. The lines present the respective fits. See text for details.

The fit models used in the previous two cases, are also employed in this section. An important observation is that in all the solutions presented until this point, micelles are present below T_{cp}; i.e. the coexistence of D_2O and alcohols does not disrupt the micellar structure. Above T_{cp}, and similar to the solution in D_2O and D_2:*d*-MeOD, the dimensionality parameter here was kept constant at 0. Preliminary fits with dimensionality parameter as free variable gave always values very close to 0. Thus the aggregates formed above T_{cp} are spherical from the beginning. Representative fits are presented in Fig. 6.10.

Fig. 6.11 compiles the results from the fits from all three regimes. Due to the very short time range of the regime I, we do not extract much information about the micellar structure. Nevertheless, at the very early stages micelles can be resolved. No information about the evolution of the micellar radius can be deduced, but the presence of micelles is an important finding. The values of r_{mic} are relatively high (i.e. ∼13.3 nm) (Fig. 6.11a), due to the fact that the first curves are already very close to the phase transition. Hence,

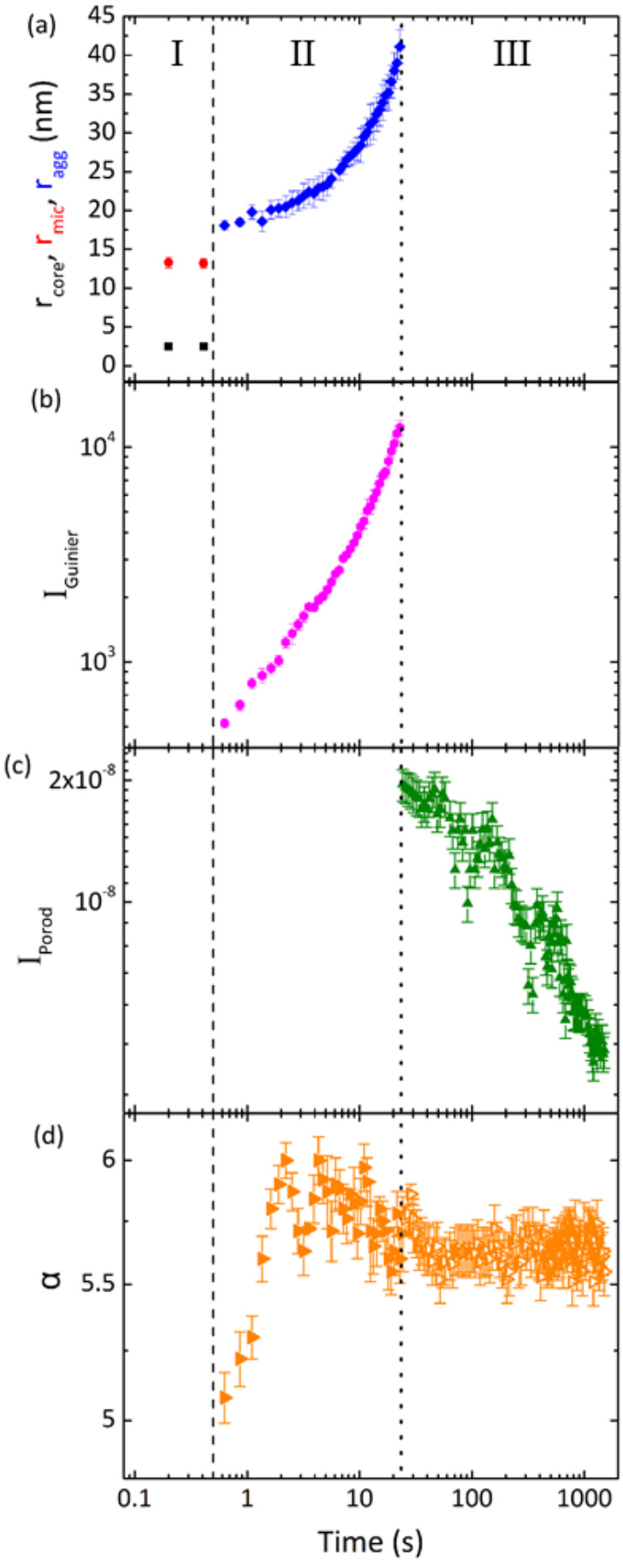

Figure 6.11: TR-SANS results. Fit parameters for P(S-d_8)$_{11}$-*b*-PNIPAM$_{431}$ in D_2O:*d*-EtOD 95:5 mol/mol as a function of time after the injection: (a) the radius of the micelles r_{mic} (red circles) and the radius of the core r_{core} (black squares) from the form factor for core shell micelles in regime I and the radius of the aggregates r_{agg} (blue diamonds) above the T_{cp} from the Guinier-Porod model in regime II; (b) the prefactor of the Guinier Porod model I_G^0 (magenta polygons); (c) from the Porod law the Porod intensity I_P^0 (green triangles); (d) the values for the Porod exponent α from both the Guinier-Porod model (orange empty right triangles) and the Porod law (orange solid right triangles). The dashed line presents the time that the T_{cp} was reached. The dotted line presents the transition between the second and the third regime. Whereas the former was found by comparing the ex-situ obtained temperature profiles with the behaviour of the SANS curves, for the latter the point was taken at which the forward scattering was starting to dominate the SANS signal.

we can assume that we resolve only the last part of the expansion of the micellar shell observed in the previous samples upon approaching the T_{cp}.

As soon as T_{cp} is reached, regime II starts and the aggregation process is triggered. Starting from an initial value of 18.1 nm, the radius of the aggregates reaches at the end of regime II a final value of 41.1 nm (Fig. 6.11a). During this regime the prefactor of the model I_G^0 is presented (Fig. 6.11b) and is found to increase with time. This increase reflects the increase of the number of the formed aggregates. These findings are in agreement with the previous systems. In regime III, the size of the aggregates is exceeds the resolution of the set-up and thus the further aggregation is followed indirectly through the decrease of the I_P^0 (Fig. 6.11c). The α is presented in the last block. As before, an increase in regime II is observed from a value of 5.08 to 5.89 and in regime III relaxes at ∼5.63. This behaviour is interpreted as a formation of dense polymer skin on the outer layer of the aggregate, which in turn creates a SLD gradient along the surface normal.

6.4.4. P(S-d_8)-*b*-PNIPAM in D_2O:*d*-DMK

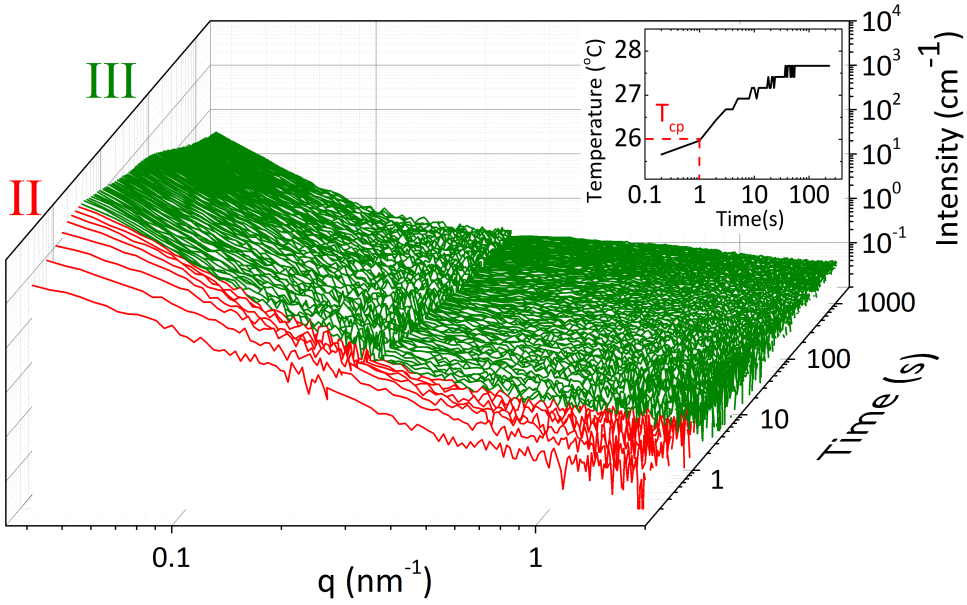

Figure 6.12.: TR-SANS curves for the temperature jump from 23 °C to 28 °C for P(S-d_8)$_{11}$-*b*-PNIPAM$_{431}$ in D_2O:*d*-DMK 95:5 mol/mol fraction. The scattered intensity $I(q)$ is presented as a function of the q for the whole time probed. Different regimes are distinguished. The inset presents the temperature profile obtained ex-situ.

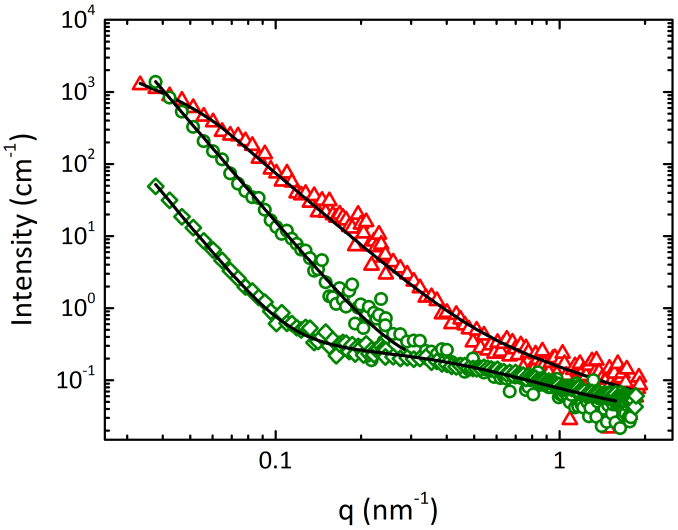

Figure 6.13.: Representative fits at different time frames of the different regimes for the sample in D_2O:*d*-DMK 95:5 mol/mol: red triangles at 0.41 s, green circles at 13.3 s and green diamonds at 1428 s after the injection. The strong drop of the I_P^0 with increasing time can be seen in the last regime. Moreover, a slight difference in the incoherent background value is observed. The lines present the respective fits. See text for details.

Here the results will be presented, that correspond to the jump from 23 °C to 28 °C for P(S-d_8)$_{11}$-*b*-PNIPAM$_{431}$ in D_2O:*d*-DMK 95:5 mol/mol. Fig. 6.12 summarizes all the measurements for this sample. Here only two regimes can be distinguished, in contrary to the previous three cases. Right from the beginning we observe regime II; i.e. small aggregates are already present in the solution. Regime I of swollen micelles is not present but already from the beginning some aggregates are present (∼20 nm), despite the fact that the temperature profile (see the inset of Fig. 6.12) indicates that the T_{cp} was reached ∼1 sec after the injection. In spite of this, no micelles can be detected within this second. This observation may have two different origins. The first is that the phase transition occurred during the transfer from the reservoir to the sample cell (i.e. in the tube). The proximity of T_{cp} to the ambient temperature may have contributed to that. Another reason could be that the small amount of aceton used here was enough to dissolve also the P(S-d_8) core. Thus no micelles are present, but only single chains dissolved.

The behaviour of the system in regime III (green curves) points also towards the absence of micelles in the solution. First of all, we observe with time that the I_P^0 decreases much stronger than in the previous cases (see also Fig. 6.14). Here the decrease spans over almost 4 orders of magnitude. Therefore, we assume that this is not only due to aggregation, but also due to strong phase separation that leads eventually to precipitation

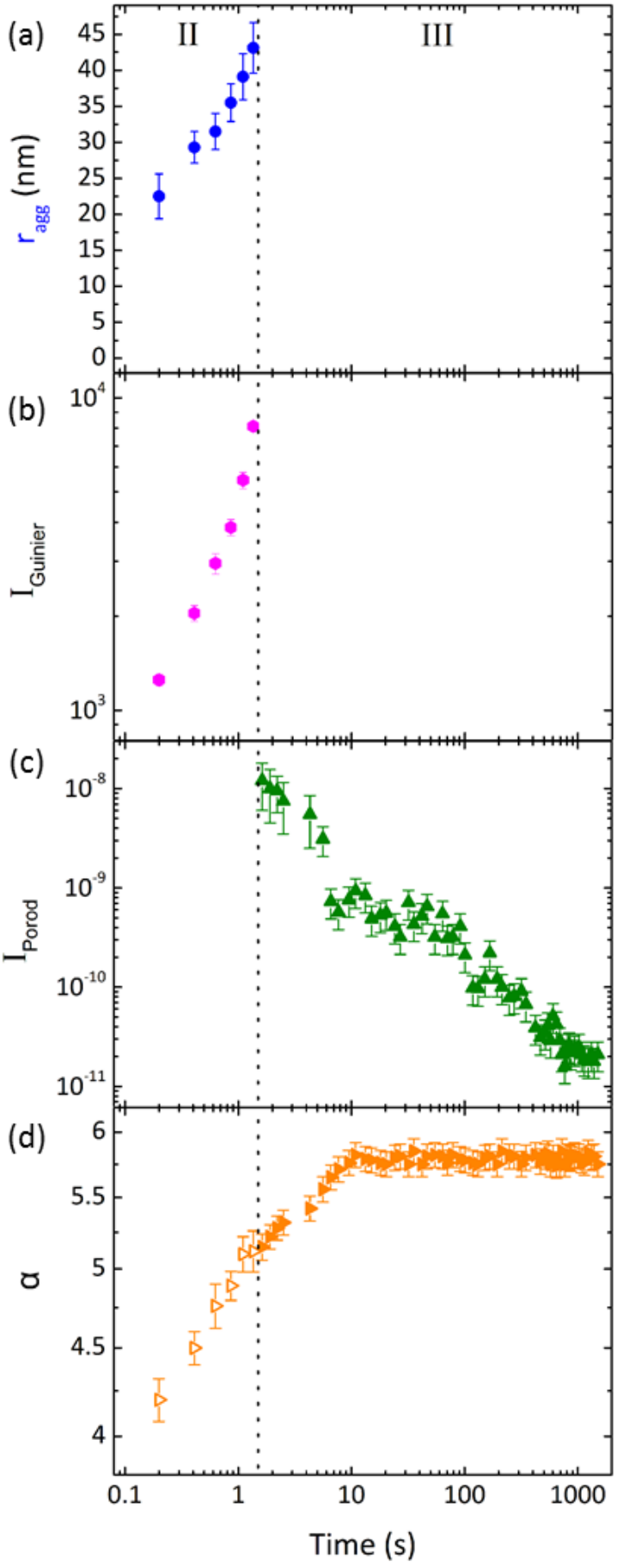

Figure 6.14: TR-SANS results. Fit parameters for the temperature jump from 23 °C to 28 °C for P(S-d_8)$_{11}$-*b*-PNIPAM$_{431}$ in D_2O:*d*-DMK 95:5 mol/mol as a function of time after the injection: (a) the radius of the aggregates r_{agg} (blue circles) above the T_{cp} from the Guinier-Porod model; (b) the prefactor of the Guinier Porod model I_G^0 (magenta polygons); (c) from the Porod law the Porod intensity I_P^0 (green triangles); (d) the values for the Porod exponent α from both the Guinier-Porod model (orange hollow right triangles) and the Porod law (orange filled right triangles). The dotted line presents the transition between the second and the third regime. For this the point was taken at which the strong forward scattering dominates the signal.

of the polymer. As a result, the concentration of the polymer in the scattering volume decreases strongly and subsequently the total intensity decreases also. This is corroborated by a slight change of the incoherent background, whereas the shoulder corresponding to the density fluctuations within the formed aggregates is more prominent. All these three points act as evidence that the aggregation process followed here is intrinsically different than in the other solutions. Taking into account the results obtained in the previous chapter, where a comparison between a micelle-forming system and a single-chain system was presented, we can assume that indeed here we follow the aggregation of single chains, rather than collapsed micelles.

The behaviour of α observed here is similar to the previous cases. Initially, a value at 4.3 is obtained and thereafter increases until reaching a value $\sim$5.75, at which remains constant until the end of the experiment. Interestingly here we do now observe the fluctuation of the values of α before the relaxation at the final, constant value. This may also act as a hint that the aggregation process in this system is totally different.

6.4.5. Aggregation kinetics

Now lets turn our attention to the aggregation process that takes place above T_{cp}. Qualitatively we observe similar trends for all 4 solutions. The fact that the solution in D_2O:*d*-DMK consists from single, dissolved chains, in contrast to the other three solutions that contain micelles, seems not to affect the trend. For the former case the aggregation is expected to be even faster, as it was seen in the previous chapter 5. This will be discussed again later. Initially the aggregates have a radius of some nm and grow with time to reach a final radius of $\sim$40 nm. Interestingly this process takes place in totally different time scales for each sample, thus it is assumed that the different solvation environments affect strongly the aggregation kinetics at a mesoscopic length scale. It would be of interest to extract information on the molecular origin of these effects. The applicability of the universal laws DLCA [WHLS84] and RLCA [LLW$^+$89] has been checked and was found not satisfying, since none of these models captured the behaviour of all four systems. This is not surprising since, as it was discussed before in this work, the aggregation of soft matter particles may deviate from these models. It is expected for soft matter particles, the interactions to be weaker, thus association and dissociation can occur, leading eventually to spherical, compact aggregates; i.e. a level of internal, structural reorganization is possible. Furthermore here the DLC model, that was used in the previous chapter to describe partially the data from the methanol content jump, failed also to describe adequately all the data sets obtained. For the case of the temperature jump in D_2O:*d*-MeOD 95:5 mol/mol this model captured well the time evolution of the aggregate radius, but failed

in the other three cases. Last but not least, we employed also the logarithmic coalescence model [KPA+14], similarly to chapter 5. Again, the model did not capture the behaviour of all four solutions, whereas qualitatively good fits resulted in values with no physical content.

We adapt here the reversible association model proposed by Zaccone et al. [ZCBB11, ZCB13]. This model was introduced in order to describe the aggregation and, eventually, gelation of dispersions of thermoresponsive nanoparticles with a radius of ≈85 nm upon the change of the temperature. This model is used here, with some minor corrections required for the much smaller particles studied here in comparison to the original work [ZCBB11,ZCB13], to describe the aggregation of collapsed micelles. Our aim is to extract the interaction potential that governs the process from the time evolution of the aggregate radius. The model describes a kinetic mechanism that is characterized by an association k_+ and a dissociation k_- rate. On one hand, k_+ is diffusion limited and in the case of large particles is given by the Smoluchowski rate $k_+ = (8/3)k_BT/\eta$, where T is the temperature and η the solvent viscosity. This holds only for large particles, i.e. for particles with radii much larger than the range of the assumed interaction. For hydrophobic interactions of soft, colloidal particles in solution this range is ∼10 nm [Isr11], therefore, especially in the first stages of the aggregation in our experiments this approximation does not hold. Thus, a more generalized expression is used, taking into account the small size of the particles [ZT12]

$$k_+ = \frac{4\pi D_{mut}}{\left(\frac{1}{2r_{agg}^{cp}} - \frac{1}{2r_{agg}^{cp}+\delta}\right) e^{-V/k_BT} + \frac{1}{2r_{agg}^{cp}+\delta}} \tag{6.3}$$

where $D_{mut} = k_BT/3\pi\eta r_{agg}^{cp}$ is the mutual diffusion coefficient, r_{agg}^{cp} the particle radius at $t = t_{cp}$, T is the temperature (taken here as T_{cp}), η is the viscosity of the mixed solvent (Table 6.1) and V the total depth of the interaction potential. δ is the width of the potential. For δ we use the nominal value of 10 nm for the hydrophobic interaction of organic surfaces in aqueous media [Isr11]. On the other hand, k_- is given by

$$k_- = \frac{D}{\delta^2} e^{-V/k_BT} \tag{6.4}$$

where $D = k_BT/6\pi\eta r_{agg}^{cp}$ is the diffusion coefficient. The reversibility of the process is captured by the effective association constant K_{eff}

$$K_{eff} = \frac{16k_+^3N^2}{(2k_- + 4k_+N - k_-2.62)^2}. \tag{6.5}$$

N is the number density of particles (i.e. the building blocks of the aggregates). For estimating N, the initial polymer concentration, together with M_w of the two blocks are used, in order to calculate the number density of chains in the solution. By assuming an aggregation number of 30 chains/micelle we can arrive at the number density of micelles in the solution. The estimation of the aggregation number per micelle was done by using the density of PS (1.05 g/cm^3), the $N_{PS} = 11$ and the volume of the micellar core of radius $r_{core} = 2.7$ nm. The steps until here were sufficient for the solution in D_2O, where the first aggregates were found to have radius of 5.7 nm, i.e. in the range of a size of a single, collapsed micelle. So the number density of micelles in the solution could serve as the initial concentration of particles N. In the other three cases the initial values of radii were higher, thus the use of number density of micelles would induce a significant error. To overcome this we estimated the number of micelles per aggregate by $V_{agg}/V_{coll,micelle}$ at $t = t_{cp}$ and corrected the number density accordingly. In short, for each one of the solutions we are obliged to use different initial radii, initial concentrations, viscosities and temperature that will give subsequently values for D and D_{mut} that differ between the systems. An overview is given in Table 6.2.

solvent	T (° C)	r_{agg}^{cp} (nm)	N (particles/m^3)	D (m^2/s)	D_{mut} (m^2/s)
D_2O	30	5.7±0.6	1.2×10^{19}	4.90×10^{-11}	9.8×10^{-11}
D_2O:*d*-MeOD	28	15.7±1.1	0.07×10^{19}	1.49×10^{-11}	2.98×10^{-11}
D_2O:*d*-EtOD	27	18.1±1.6	0.04×10^{19}	1.22×10^{-11}	2.43×10^{-11}
D_2O:*d*-DMK	26	22.1±2.4	0.02×10^{19}	9.83×10^{-12}	1.97×10^{-11}

Table 6.2.: The values of all coefficients for all four solutions required for the aggregation model; the temperature $T = T_{cp}$, the initial radius r_{agg}^{cp} taken as the first value of the fit in regime II (above T_{cp}), the number density N after the correction for the early formation of small aggregates in the samples with the alcohols, the diffusion coefficient D and the mutual diffusion coefficient D_{mut} are given.

The final result is a master equation that expresses the radius evolution with time

$$\frac{dr_{agg}(t)}{dt} = \frac{I_2}{2I_1}\left(1 - \frac{r_{mon}}{r_{dim}}\right) NK_{eff} r_{agg}^{cp} = cNK_{eff} r_{agg}^{cp} \tag{6.6}$$

where I_1 and I_2 are the scattering intensities of a monomer, here taken as a particle with radius $r_{mon} = r_{agg}^{cp}$, and of a dimer with $r_{dim} = 1.38 r_{agg}^{cp}$ [RSS01] at $q \to 0$, respectively. In the original work, I_1 and I_2 were taken from light scattering experiments, i.e. at large q values. Here, to estimate I_1 and I_2 we use the relation $I(q \to 0) \propto (\Delta\rho)^2 NV^2$, with V the volume, estimated here as $V = 4\pi r^3/3$, N the number of particles, as found before, and

$\Delta\rho = \rho_{agg} - \rho_{sol}$ which is taken as a constant. For estimating ρ_{agg}, the volume fraction of the two blocks, i.e. PNIPAM and P(S-d_8), and their ρ values were used. If we assume that during the formation of dimers, the $\Delta\rho$ is constant, we arrive at a value of $A = 0.78$.

By applying Eq. 6.6, we can describe the aggregate radius with time and, as a result, we can access K_{eff}. The fits are presented in Fig. 6.15. A very good agreement is observed. As it can be seen from Eqs. 6.5, 6.3, 6.4 the only unknown variable in K_{eff} is the depth of the potential V. Thus the model offers a tool to extract the interaction potential for the the 4 solutions and, subsequently, an access to the molecular interaction. The results of the fits are summarized on Table 6.3. We observe a systematic decrease of the depth of the interaction potential, as the size of the cononsolvent increases. This is direct reflection of the aggregation kinetics, as observed in Fig. 6.15.

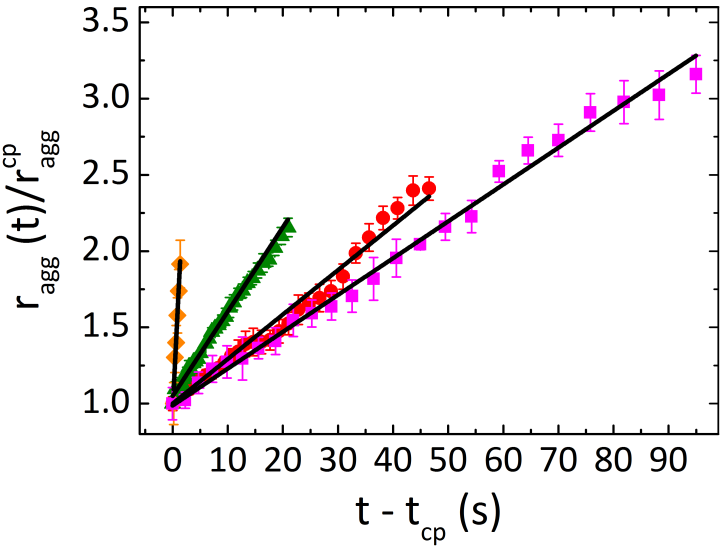

Figure 6.15.: The normalized radius of the aggregates is presented as a function of the reduced time $t - t_{cp}$. As t_{cp} the time when T_{cp} was reached is used. In the case of D_2O:*d*-DMK, where the aggregation started before the nominal T_{cp}, we use as t_{cp} the start of the SANS experiment (t_{cp}=0.2 s). The data for D_2O (magenta squares), for D_2O:*d*-MeOD (red circles), for D_2O:*d*-EtOD (green triangles) and for *d*-DMK (orange diamonds) are presented. The lines are the fits of Eq. 6.6 to the experimental data.

A common way to describe the interaction of two spherical particles in solution is a Lennard-Jones potential [Jon24]. Since here we consider the hydrophobic interaction we have to account for the limited range of the hydration force (i.e. δ=10 nm [Isr11]), therefore we use a truncated LJ potential that reads

solvent	K_{eff} (s^{-1})	V_{tot} (k_BT)
D_2O	9.47×10^{-19}	-5.71
D_2O:*d*-MeOD	9.02×10^{-18}	-7.59
D_2O:*d*-EtOD	6.52×10^{-18}	-8.18
D_2O:*d*-DMK	6×10^{-18}	-8.66

Table 6.3.: The results of the fits of Eq 6.6 on time evolution of the radii. The effective association constant K_{eff} and the depth of the resulting interaction potential V_{tot} are given.

$$U(h) = \begin{cases} U_{LJ}(h) - U_{LJ}(h_c) & , \; for \; h \leq h_c \\ 0 & , \; for \; h > h_c \end{cases} \tag{6.7}$$

where h_c is the cut off length, equal to $\delta = 10$ nm and $U_{LJ}(h)$ denotes the classic Lennard-Jones potential

$$U_{LJ}(h) = 4V \left[\left(\frac{\sigma}{h} \right)^{12} - \left(\frac{\sigma}{h} \right)^{6} \right] \tag{6.8}$$

of a total depth V. The fits of Eq. 6.6 on the radii data give access to the values of V for the respective solutions. In this way we can reconstruct the interaction potentials of the four solutions. The results are presented in Fig. 6.16. Interestingly, a systematic influence of the molar volume of the cononsolvent is observed; i.e. for higher molar volume values a deeper potential is retrieved and thus the interaction is stronger. This is a direct reflection of the differences on aggregation kinetics observed in 6.15. The systematic increase of the depth of the well, as the molar volume of the cononsolvent increases, quantifies the influence of the solvation environment on the molecular interaction. We would like to elucidate more on the origin of this influence and try to reveal the molecular picture that governs this behaviour.

To address this point, we consider the stronger influence that the cononsolvent molecules is expected to have on the olution. As discussed before in this chapter, and also as it will be proven experimentally in the next one, any alcohol molecule in aqueous environment induces an enhanced structural organization of water molecules around it; i.e. affects the structure of the water molecules. This is a well established phenomenon in literature, is termed as *kosmotropic* effect. The latter originating from the order induced [GSAK97]. This topic is of high importance for our work and will be thoroughly discussed in the next chapter. In the context of the presented here results, we propose a novel model to describe our observations. According to this, in pure D_2O the water molecules create

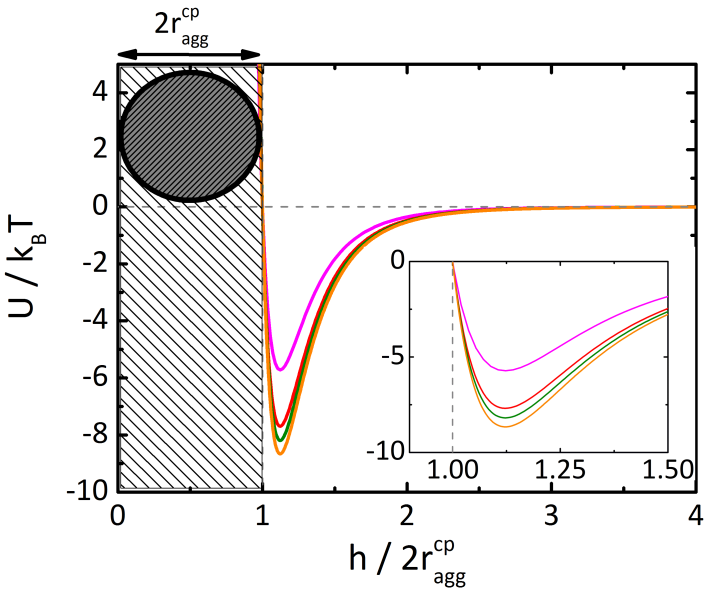

Figure 6.16.: The potential wells describing the interaction between the aggregating particles in the four different solutions; in D_2O (magenta line), in D_2O:*d*-MeOD (red line), in D_2O:*d*-EtOD (green line) and in D_2O:*d*-DMK (orange line). The inset shows a magnification of the wells close to their minimum.

structured layers on the aggregate surface. Several studies have shown that PNIPAM still contains water even above T_{cp} [MHI00, KNM+05, PKS+14], presumably due to residual H-bonds between water molecules and the amide group. Thus the idea of residual hydrophilicity, which is the prerequisite for the formation of the hydration layers, has found some experimental evidence. As a consequence, these layers induce a repulsive hydration force, of steric character, that mediates the interaction. We propose that the picture is strongly altered when the alcohol molecules are present. Due to the energy gain for D_2O to hydrate the alcohol molecules instead of PNIPAM [BCT14, BCDLR+14], the layers of structured water are perturbed and therefore the repulsion they induce is decreased or even diminished. The imminent result is the acceleration of the aggregation kinetics. Moreover, the influnce is expected to be stronger for larger molecules since they will accommodate more water molecules, which is in agreement with the results presented in Fig. 6.16. A schematic representation of the proposed here model is given in Fig. 6.17.

Based on the proposed model in the previous paragraph, we wish now to quantify our results. We assume that the total potential consists of an attractive part, due to the hydrophobic interaction, and a repulsive one, due to the repulsive, hydration force. The former is considered to be equal in all 4 solutions studied without loss of validity; i.e. a typical value of $-10k_BT$ is selected. The assumption of equal attractive interaction in all

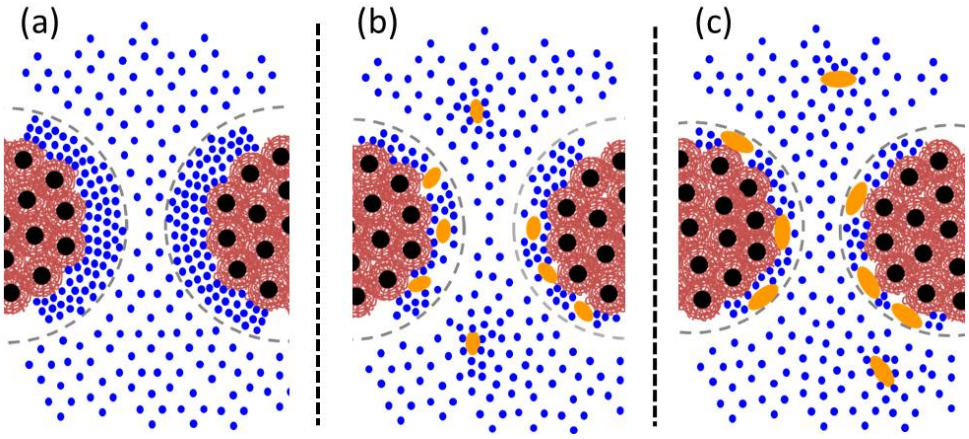

Figure 6.17.: A schematic representation of the proposed model (not to scale). In pure D_2O (a), layers of structured water (blue circles) are formed on the surface of the particles, exerting a repulsive force. In the presence of alcohol molecules (orange ellipses) (b), the structuring of the water is perturbed and the repulsive force is decreased. The magnitude of the perturbation is expected to increase with increasing the size of the cononsolvent (c).

cases is a simplification of our approach that leaves aside any influence of the solvation environment. This approach is not expected to induce significant errors to our results. For the second part, the repulsive hydration is modelled by the following expression

$$U_{rep}(h) = F_0 r_{agg}^{cp} \lambda^2 \exp\left(-\frac{(h - r_{agg}^{cp})}{\lambda}\right) \tag{6.9}$$

which is based on the original expression [Isr11] and modified to account for the spherical shape of the particles. Here F_0 is the force constant, which is strongly dependent on the system, and reflects the level of organization of the water layers within the structured layer and λ is a measure of the width of the layer of structured water molecules. Since both F_0 and λ are *a priori* unknown, no direct way to access any of the two is possible. Ideally, sophisticated measurements (e.g. AFM investigation of the force exerted upon the approach of two colloidal particles) could reveal experimental values for these two parameters. This would be outside the scope of this work, but our results can spark future experiments on this subject. Still, it is possible to estimate F_0 as a function of λ. It has been seen in previous studies that λ has nominal values in the range 1-2.5 nm ($\sim 10 \times r_{H2O}$, where $r_{H2O} = 2.75$ Å is the radius of a single water molecule). By varying thus λ within this range, we calculate the values of F_0 for $h = 2^{1/6} \times 2r_{agg}^{agg}$, i.e. at its deepest point, where the $V = V_{tot}$ as summarized in Table 6.3. The resulting F_0 values are presented in Fig. 6.18. A systematic decrease of F_0 with increasing ratio $V_{m,alcohol}/V_{D_2O}$ is observed for all λ's, i.e. the constant of the hydration force decreases as

the molar volume of the alcohol increases. A physical picture that could be assigned to this observation is the decrease of the level of structuring of the water molecules within the hydration layer. This result comes in agreement with the proposed model (Fig. 6.17) and implies that the presence of the alcohol molecules disrupts the level of ordering of the structured water layers. Subsequently the repulsive force decreases and the aggregation accelerates. Moreover, the larger the molar volume of the alcohol is, the stronger the effect, as expected since larger alcohols are perturbing stronger the structure of water. Previous studies on the repulsive, hydration forces between two hydrophilic, silica surfaces in mixed solvents have shown that the addition of the methanol decreases the hydration force [YV98]. Moreover, in the previous chapter of the present work it was shown that the addition of larger volume fractions of methanol to aqueous solutions of a PS-*b*-PNIPAM resulted in a complex aggregation pathway, that was consistent at the later stages with the presence of an energy barrier which was increasing with r. Here, we probe a qualitatively different stage of the aggregation, i.e. a much earlier one.

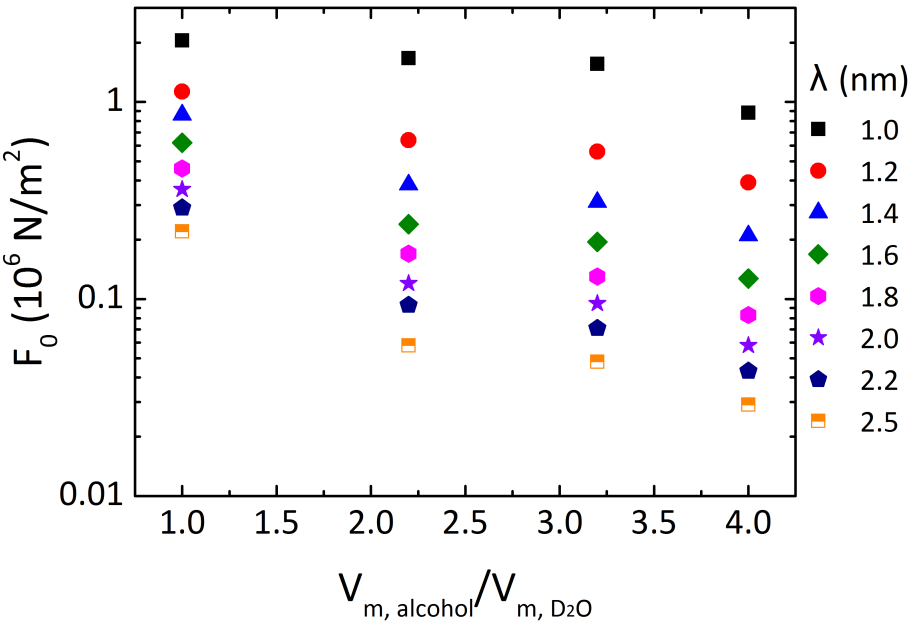

Figure 6.18.: The constant of the hydration force F_0 as a function of the ratio $V_{alcohol}/V_{D_2O}$ for selected λ values. A systematic decrease is observed, as the volume of the cononsolvent molecule increases.

Concluding this section of the work, we would like to emphasize on the novel model proposed in this work and highlight the strength of combining the experimental results with a theoretical model. Acting in a complementary way, these two tools allowed us to

access the molecular interactions, and quantify the influence of the solvation environment on it, starting from the mesoscopic length scale. To the best of our knowledge, this is the first report of this kind of relation in the case of aggregation of PNIPAM-based in particles in solution and may lead to a deeper understanding of previous results.

6.5. Conclusions

This chapter presented a study of the influence of different solvation environments on the aggregation kinetics of a P(S-d_8)-*b*-PNIPAM amphiphilic block copolymer. In contrast to the previous chapter, we followed here a different approach, namely the phase separation was induced by temperature jumps and the aggregation was followed by means of TR-SANS. This allowed us to resolve different stages of the system, also below and above T_{cp}. By varying the solvation environment, i.e. by using 3 different cononsolvents - i.e. short chain alcohols - and studying also a solution in pure D_2O, we aim to study the influence of the molar volume of the cononsolvents on the aggregation kinetics.

Below T_{cp} micelles are formed in all cases, except from the solution in D_2O:*d*-DMK; presumably the small amount of acetone present dissolved the PS core of the micelles. In the cases, where micelles are present, an increase of the micellar radius, i.e. of the micellar shell, is observed as T_{cp} is approached, and moreover, this increase is higher in the mixed solvents. This reflects the influence of the solvation environment on the molecular conformation of PNIPAM. Above T_{cp} the PNIPAM shell collapses, and the collapsed micelles associate into bigger aggregates. We follow the evolution of the aggregates size with time.

The study of the radii reveals a strong influence of the solvation environment. In all mixed solvents the aggregation evolves faster than in pure D_2O and moreover, in the mixed solvents the aggregation rate depends on the molar volume of the cononsolvent molecule. The larger the latter is, the faster the aggregation becomes. We quantify this influence by employing the reversible association model [ZCBB11, ZCB13]. We extract thus the interaction potentials that govern the aggregation at a molecular level. They are found to deepen with increasing $V_{m,alcohol}$, reflecting the respective behaviour of the radii with time at a mesoscopic length scale. We propose a novel model to explain this experimental observation. According to this, in pure D_2O layers of structured water molecules are formed on the aggregates surface and create a repulsive, hydration force that mediates the interactions and decelerates the aggregation. The presence of alcohol molecules is expected to disrupt these water layers, since the latter will preferably hydrate the alcohols rather than PNIPAM. The phenomenon is expected to be stronger for larger

alcohol molecules. Indeed, by quantifying the characteristics of the hydration force, a systematic decrease of its strength with increasing $V_{m,alcohol}$ is retrieved.

The results presented in this part of the work highlight the strength of combining experimental techniques with theoretical models, accessing thus the molecular interactions that govern the processes at a molecular level. The novel model presented in this work, within the theoretical framework of the reversible association model, can thus help in understanding under a new scope previous results on aggregation processes of colloidal dispersions of thermoresponsive polymers or particles.

7. Solvent dynamics

As it was discussed in the first part of this work, the origin of cononsolvency lies at the molecular origin, i.e. in the local polymer-solvent and solvent-solvent interactions. Few previous studies have employed Fourier transform infrared spectroscopy (FTIR) to study PNIPAM in mixed solvents of water and methanol. Liu et al. have detected significant changes in the spectra around the critical methanol volume fractions, at which the PNIPAM collapses [LBS05]. Sun and Wu confirmed the results of Liu et al. [LBS05], and furthermore emphasized on the formation of water - methanol clusters, proposing the latter as the main reason for cononsolvency [SW10]. In another work, Katsumoto et al. studied in detail the changes induced by the addition of methanol in the intramolecular hydrogen bond [KTI$^+$07]. Interestingly, these results imply that the MeOH is not only active with the outer solvating layers that interact with PNIPAM, but rather interacts more directly with the polymer chain.

In this part of the work we will present a QENS study of the diffusion dynamics of the solvation species, water and methanol, in their coexistence in a ternary solution PNIPAM/water/methanol. Previous results on aqueous solutions of PNIPAM, offered by our group [PKS$^+$14], highlight the strength of QENS in studying the diffusion dynamics of solvating molecules. The aim of this part of the work is to resolve the interactions between the different components of the system and reveal the decisive factors that create cononsolvency. The unique ability of neutrons to distinguish between hydrogen and deuterium will be used here. By studying mixtures of the same composition and using pairs of non-deuterated / deuterated solvents, i.e. H_2O:*d*-MeOD and D_2O:MeOH, we are able to selectively study the dynamics of the protonated component. Additionally, by varying the temperature, we aim to clarify to which extent the phase separation of polymer will influence the dynamics of the solvation molecules. To the best of our knowledge, this is the first QENS study on the subject of cononsolvency. The chapter is structured as follows. First the strategy of the experiment will be explained and afterwards the experimental set-up will be briefly explained, as well as the sample preparation routine. In the results part that follows, first the results emphasizing on the dynamics of H_2O will be presented and afterwards the ones on MeOH. At the end a short discussion on the results will be presented as a concluding point.

7.1. Strategy

In this part of the work we will probe the dynamics of the solvent molecules in a solution of PNIPAM homopolymer in a mixed solvent of H_2O and MeOH. To obtain the complete picture, we start with measurements of the two pure solvents and their pure mixture (no polymer added). These measurements will allow us to prove experimentally the influence of MeOH on the structure and the diffusion dynamics of H_2O. Moreover, they will create the basis for evaluating the impact of each step on the diffusion dynamics of the solvation species. To tune the selectivity of the method, we measure a mixture of the two solvents where the one of the two components is deuterated; this allows us to focus on the dynamics of the one of the components selectively. The composition of the mixed solvent is kept constant at 85:15 v/v H_2O:MeOH (i.e. 85:15 v/v H_2O:*d*-MeOD and 85:15 v/v D_2O:MeOH, respectively). In the next step we add the polymer at a concentration of 25 wt. %. The polymer concentration was chosen at this value to ensure that the majority of the solvating molecules will be associate with the polymer chain, similarly to previous experiments [PKS$^+$14]. So we are able to study the dynamics of the solvent molecules in the ternary mixture of water-methanol-PNIPAM. Again here, two samples are studied; namely H_2O:*d*-MeOD:PNIPAM and D_2O:MeOH:PNIPAM. These two samples allow the separate study of the non-deuterated solvent in the presence of the other other solvent and the polymer chain. The dynamics of the polymer chain are outside the resolution window of this technique and well separated on the time scale from the dynamics of the solvent molecules by two orders of magnitude. So, we focus on one of the two solvent components and study the influence of the complexity of the solvation environment and the critical behaviour of the polymer on its diffusion dynamics. Starting from the pure solvents, and proceeding in the next step to the pure mixture of the two solvents, we are able to deduce the complete picture, when we consider also the polymer.

7.2. Experimental

All experiments were performed at the cold spectrometer TOF-TOF, located in MLZ, Garching. The polymer solutions were prepared one week prior to the beamtime. PNIPAM was obtained from Sigma-Aldrich (M_w=22500 g/mol) and was used as received. Millipore water (H_2O) and highly pure methanol (from Carl-Roth) were used for the non-deuterated components. Deuterated solvents were obtained from Deutero GmbH (D_2O and *d*-MeOD) and were both 99.9 %. The preparation was done in three steps. The two solvents were mixed at the first step and left to equilibrate for 24 hours. The polymer was then added in two steps to achieve a final polymer concentration of 25 wt. %, with a gap

of 3 days. The latter was required in order to avoid phase separation due to the very high final concentration. The samples were stirred until clear, viscous solutions were obtained and kept afterwards at ∼4 °C. The day before the beamtime the samples were put in the sample holders. The latter consists of a couple of aluminium cylinders with a slit size of 0.1 or 0.2 mm, depending on the sample. In this slit the sample was inserted and then it was hermetically closed to avoid the evaporation of the highly volatile alcohol. Fig. 7.1 shows a photo of the sample holder before and after the insertion of the sample. This step was difficult to the high viscosity of the solution and the very small volume of the sample holder. For the sample PNIPAM at 25 wt.% in D_2O:MeOH 85:15 v/v a sample holder with a slit size of 0.2 mm was used, because the protonated component which is expected to dominate the scattering signal is the minority of the solvation environment. By using the thicker slits for this sample, we increased the statistics and decreased the required accumulation time. The T_{cp} values for the two polymer solutions were determined beforehand and were found to be 28 °C and 27 °C in H_2O:*d*-MeOD and in D_2O:MeOH, respectively.

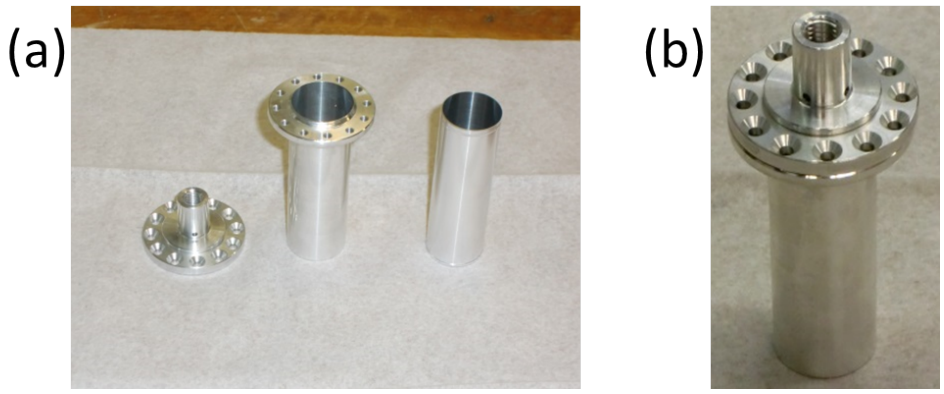

Figure 7.1.: Photographs of the sample holder used for the QENS experiment. Before (a) and after (b) the insertion of the sample. The difference of the radii of the two cylinders defines the slit size.

7.3. QENS

7.3.1. H_2O

First the results for the pure water will be presented. Two different temperatures were selected; i.e. 21 °C and 34 °C. The obtained spectra were analysed by using two Lorentzians, together with a Gaussian describing the elastic line (Fig. 7.2). Naively thinking, we would

expect one Lorentzian to suffice for describing the spectrum of bulk H_2O, since only the long range diffusion of H_2O molecules is expected to contribute. In our experiments, this was not the case. For the proper analysis of the spectra, we are obliged to use two Lorentzians. We explain the presence of a second contribution by local motions of the H_2O (e.g. rotational modes) as suggested in previous experiments performed at the same instrument with similar energy resolution set-up [BU11]. Thus, we continue with using two Lorentzians, one accounting for the long range diffusion and one for local motions.

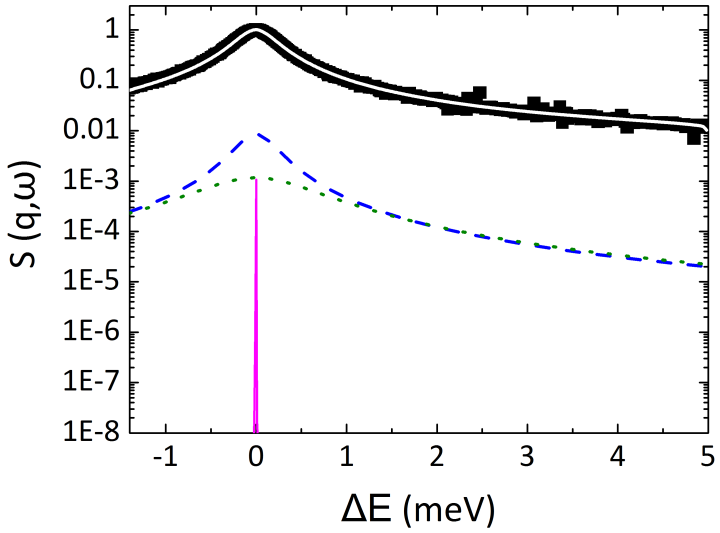

Figure 7.2.: QENS spectrum $S(q,\omega)$ of pure H_2O as a function of the energy transfer ΔE at q=1.1 Å^{-1} at 21 °C. The experimental data are presented by the black squares and the total fit by the solid white line. The different contributions to the fit are presented also; the narrow Lorentzian (blue dashed line) accounting for the long range diffusion, the broad Lorentzian (green dotted line) accounting for local motions and the vanadium measurement (magenta solid line) for the elastic line.

Fig. 7.2a presents representative QENS spectrum for H_2O at a selected q-value at 21 °C, together with the respective fit. The different contributions to the final fit are also presented. We use here a narrow Lorentzian (L_{narrow}) to describe the long range diffusion of the water molecules and a broad one (L_{broad}) to capture the local motions.

From the two Lorentzians we extract all the width Γ. The results are presented in Fig. 7.3. Γ_{narrow} describes the diffusion of water molecules, thus its q^2 dependence will give their diffusion coefficient (D_{jump}). It has been shown that the diffusion of water is better described by a jump diffusion model, rather than a normal diffusion model [Be8, GCT+10, QSH11]. According to this model, a H_2O molecule remains at a given

position for a certain residence time before it jumps to another position. The length of this jump is a characteristic quantity of the process and for bulk H_2O, it is $\sim$ 1 Å [HLLH04, QSH11]. From the fits of the jump diffusion model to our data (see Fig. 7.2) we obtain D_{jump} for water molecules and also the residence time τ_{res}.

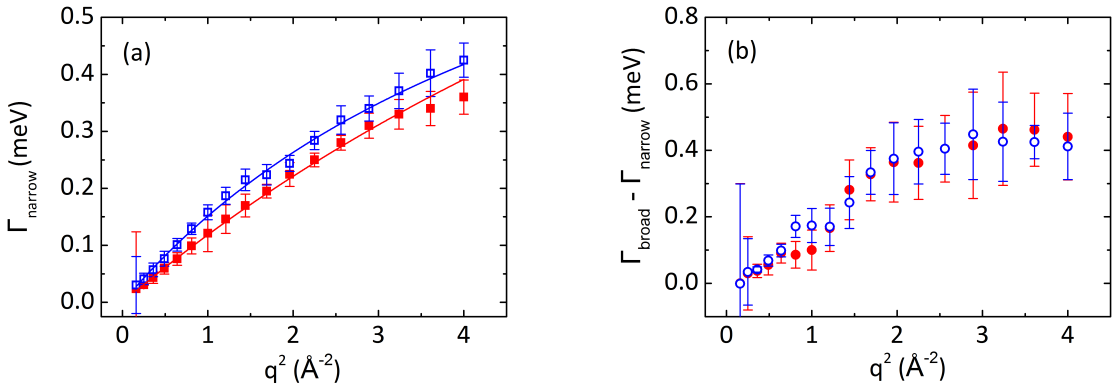

Figure 7.3.: The width Γ of the two Lorentzians as a function of the q^2 at 21 °C (red solid symbols) and 34 °C (blue hollow symbols) for (a) the narrow Lorentzian describing the long range diffusion of H_2O molecules and (b) the difference of the widths between the narrow and the broad Lorentzian. In (a) the lines present the fits of the isotropic jump diffusion model to the experimental data.

The former is presented in Fig. 7.4 together with several values from the literature for comparison. We see a very nice agreement between our results and the previously reported values for the D_{jump} of H_2O molecules. Moreover, it shows also the expected dependence on the temperature. The residence time τ_{res} is at both temperatures 0.12 - 0.13 ps, so very close to the expected value [QSH11]. Γ_{broad} is q-dependent (see Fig. 7.3b) as well, a behaviour that is not expected for purely rotational motions. At this point no clear indication is given about the true origin of this relaxation mechanism. We postulate that the second contribution is a superposition of from several local motions of the H_2O molecules and not from only one, distinct rotational motion. In any case, no further analysis was attempted within the framework of this thesis. Nevertheless a use of a very broad Lorentzian is required in the analysis of all the spectra. For sake of clarity and completeness, we have to point out that especially in the QENS curves that describe the ternary system water-methanol-PNIPAM the contribution of this broad contributions very small. In any case it has been shown that the selection of the broad Lorentzian does not affect the narrow Lorentzian [SBGU08], hence we have a solid basis to proceed with our analysis.

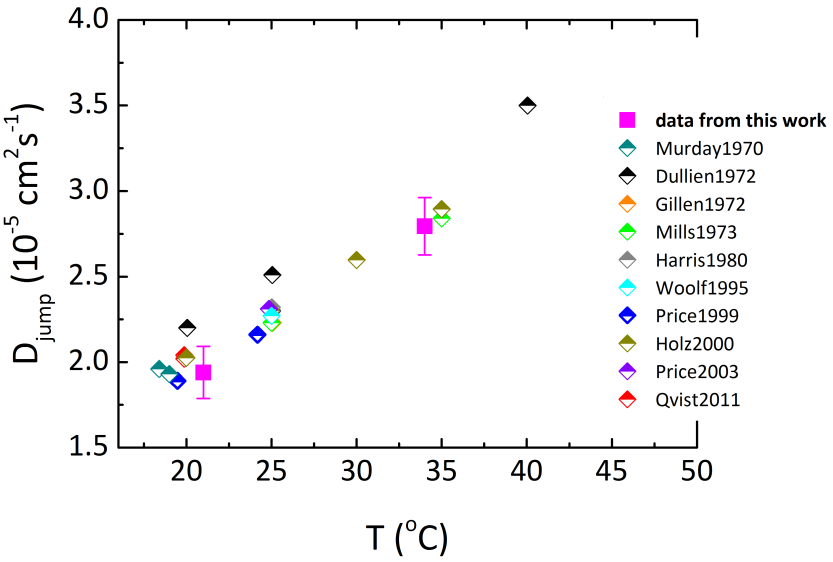

Figure 7.4.: The diffusion coefficient D_{jump} for bulk water from this work (magenta filled squares) as function of temperature. Values from the literature are also presented for comparison; by QENS:Qvist 2011 [QSH11]; by NMR: Price 1999 [PIA99], Harris 1980 [HW80], Holz 2000 [HHS00], Murday 1970 [MC70], Price 2003 [PIA03], Woolf 1985 [Woo85] ; by IR and Raman: Gillen 1972 [GDH72]; by diaphragm-cell technique: Mills 1973 [Mil73]; by theoretical modelling: Dullien 1972 [Dul72].

7.3.2. H_2O:*d*-MeOD 85:15 v/v

In the next step we present the results obtained for the mixture H_2O:*d*-MeOD 85:15 v/v. Here, we aim at studying the influence of the presence of the *d*-MeOD on the diffusion dynamics of H_2O. Fig. 7.5a presents a qualitative comparison of the QENS spectra for pure H_2O and for H_2O:*d*-MeOD 85:15 v/v. As expected, the presence of *d*-MeOD results in slowing down the diffusion dynamics of the H_2O molecules; i.e. the spectrum becomes narrower. To quantify the results we proceed by fitting again a sum of two Lorentzians, for long range diffusion and local motions respectively, and a Gaussian for the elastic line, as in the previous part for the pure water.

From the analysis we obtain the q^2-dependence of Γ_{narrow} as presented in Fig. 7.6a. We apply again the the isotropic jump diffusion model (Fig. 7.6a) to derive the D_{jump} and the τ_{res} of the H_2O molecules in the presence of *d*-MeOD. The results are presented in Fig. 7.6b. The data for bulk H_2O are also presented for comparison. As expected, we observe a decrease of the D_{jump} of the water in the presence of methanol molecules. This observation verifies the picture presented in several previous studies and is in agreement with the physical picture assumed for the system [KU77, Woo85, SF93, LC96, MTV+96,

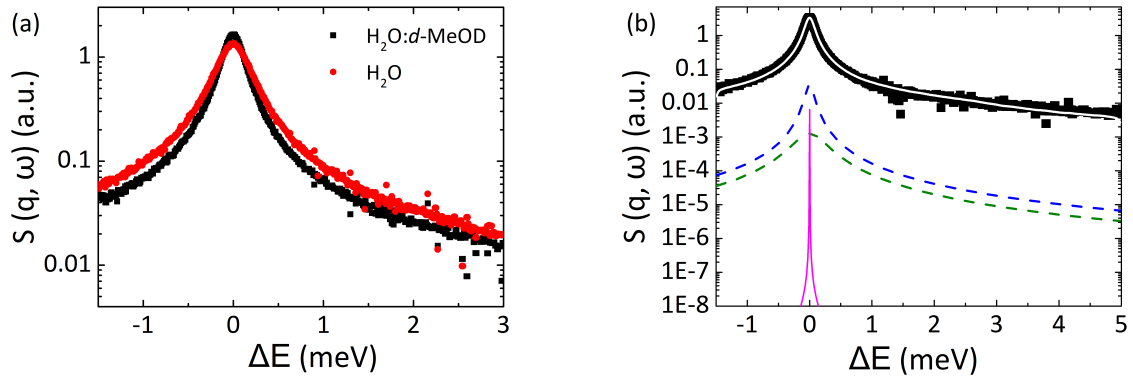

Figure 7.5.: (a) Comparative plot for bulk water (red circles) and for the mixture H_2O:*d*-MeOD 85:15 v/v (black squares). (b) QENS spectrum $S(q,\omega)$ versus energy transfer ΔE for q=1.1 Å^{-1} of H_2O:*d*-MeOD 85:15 v/v at 21 °C. The experimental data are presented by the black squares and the total fit by the solid white line. The different contributions to the fit are presented also; the narrow Lorentzian (blue dashed line) accounting for the long range diffusion, the broad Lorentzian (green dotted line) accounting for local motions and the vanadium measurement (magenta solid line) that defines the resolution.

LKS97, PIA03, MBC$^+$10, PG12, PM13]. Experiments by various experimental techniques and simulations have proven that the coexistence of water with any short chain alcohol, which is able to create H-bonds, is accompanied by the formation of complexes between the two components. Especially in the water rich regime, it has been suggested that the water molecules "hydrate" the alcohol (here *d*-MeOH) molecules by forming around them a hydrating cluster. Consequently, the structure of water is enhanced and becomes more stable, resulting in the observed decrease of the diffusion coefficient. Due this effect on the water structure, methanol and most of the alcohols (ethanol, isopropanol, etc.) are called kosmotropes [GSAK97, MNDLR04]. In contrary substances that destroy the structure of bulk water are called chaotropes [CF02], due to the *chaos* they induce.

An impact on the τ_{res} values of H_2O is observed; in the mixed environment τ_{res} increases slightly, giving an extra indication for the strengthen of the water network. Namely here we obtain τ_{res}=0.68 ps and τ_{res}=0.35 ps at 21 °C and at 34 °C respectively.

Since this thesis is focused on the behaviour of the solvent in the presence of the PNIPAM chain, we performed here measurements only at the two extreme temperatures planed to be studied for the samples containing the polymer. Thus, we do not proceed with a deeper analysis of the spectra of the solvent mixture. It is encouraging though, to see that the D_{jump} values for the free water and the water that interacts with methanol, are well separated in the D_{jump} vs T map in Fig. 7.6. Furthermore, since QENS data

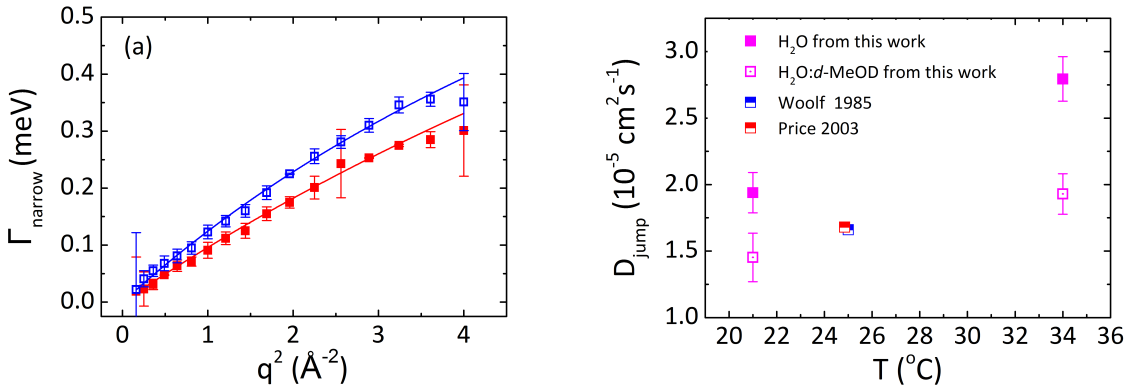

Figure 7.6.: (a) Γ_{narrow} describing the long range diffusion of H_2O in the presence of *d*-MeOD as function of q^2 at 21 °C (red solid squares) and at 34 °C (blue hollow squares). The lines present the fits of the isotropic jump diffusion model on the data. (b) The resulting D_{jump} for the H_2O in the presence of *d*-MeOD, in comparison to the values of bulk H_2O from this work and values from the literature for mixtures H_2O:*d*-MeOD; from NMR: Woolf 1985 [Woo85], Price 2003 [PIA03].

of mixtures of water and methanol are scarce, if not non-existing, it was vital for the interpretation of the data presented in the next sections, to create in these first steps a clear picture about the diffusion dynamics of the pure solvents and their mixtures as probed by our experimental set-up. The reassuring agreement of our results with literature values for both bulk H_2O and H_2O:*d*-MeOD creates a solid basis for the next steps.

7.3.3. 25 wt.% PNIPAM in H_2O:*d*-MeOD 85:15 v/v

In this section, we present the QENS data from the PNIPAM solution at 25 wt.% in mixture of H_2O:*d*-MeOD 85:15 v/v. We aim at probing the dynamics of the water molecules in the presence of both *d*-MeOD and the PNIPAM chains. It is expected that, in pure aqueous solutions of PNIPAM at this concentration, the majority of the H_2O will be associated to the polymer chains [OSKY09, PKS+14]. In addition to that complexes of methanol and water molecules may also occur, as has been seen in the previous section (7.3.1). Fig. 7.7 presents a representative QENS spectrum for this sample at q=1.1 Å^{-1} at 21 °C. In order to fit the spectra here we had to use 3 Lorentzians. We attribute the two narrow Lorentzians to two distinctive water populations: one very strongly associated ($L_{verynarrow}$) and one loosely associated (L_{narrow}) water population; i.e. the former is expected to exhibit severely arrested dynamics, and the latter less arrested dynamics but in any case slower than the bulk H_2O. Again we need to use a broad Lorentzian (L_{broad}) to capture the behaviour of the curve at large ΔE values. As before, we assign L_{broad} to a

sum of local motions, and thus we will not discusse it further. For sake of completeness, we tried to fit the data with only two contributions (i.e. not use L_{broad}). The values obtained were identical for the $L_{verynarrow}$ and slightly different for L_{narrow}. Thus, we proceeded with using both 3 L_i in order to achieve the best results and also to have a common approach to the data treatment throughout the whole chapter of this work.

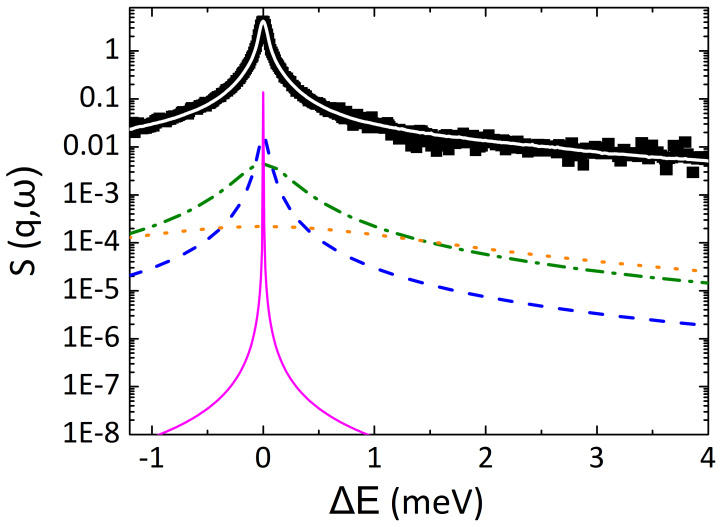

Figure 7.7.: QENS spectrum for PNIPAM solution at 25 wt.% in H_2O:*d*-MeOD 85:15 v/v at 21 °C at q=1.1 Å^{-1}. The experimental data are represented by the black squares and the total fit by the white solid line. The partial contributions to the total fit are also presented: the $L_{verynarrow}$ describing strongly associated water (blue dashed line), the L_{narrow} describing loosely associated water (green dash-dotted line) and L_{broad} accounting for local motions of water molecules (orange dotted line). The magenta line gives the experimentally measured vanadium spectrum.

The resulting widths Γ_i are presented in Fig. 7.8. Both are exhibiting q^2 dependence as expected for water diffusion, but at different absolute values. Therefore, we model the results with the isotropic jump diffusion model, as before. The D_{jump} values for the two populations are presented in Fig. 7.9a, together with the values for bulk H_2O and for the mixture D_2O:*d*-MeOD 85:15 v/v. We observe that the D_{jump} values of the two populations are well separated, hence we can distinguish clearly the difference in the diffusion dynamics. The strongly associated water indeed exhibits strongly arrested dynamics. The speculation about the existence of this water population, generally referred to as first hydration layer, has inspired a very vivid discussion in literature, because this first hydration layer is expected to play an important in the functionality of many biologic soft matter systems [MM14,SJC14,Hey14]. Very recent experiments have given an indirect

evidence of the existence of such a population in aqueous solutions of the same PNIPAM system at the same concentration [PKS+14]. Previous studies on PNIPAM gels have also produced indications for the existence of a population of water molecules with strongly restricted diffusive behaviour [HLLH04, CCP07, GCT+10].

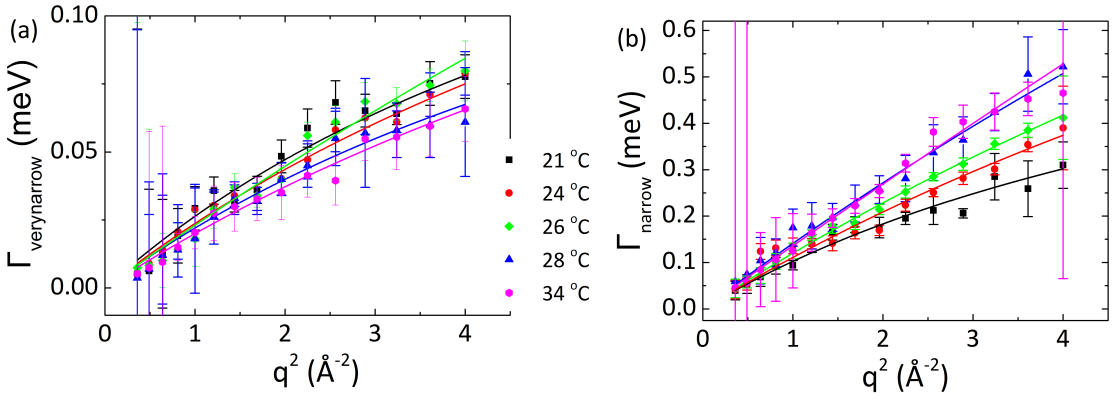

Figure 7.8.: The widths of the Lorentzians describing the two populations of water at all temperatures: (a) $\Gamma_{verynarrow}$ for the strongly and (b) Γ_{narrow} for the loosely associated water. The lines present the fits of the isotropic jump diffusion model. The legend in the middle holds true for both graphs.

The behaviour of the D_{jump} values of this strongly associated population as a function of temperature is stable. This is an unexpected result, since it is expected to be significantly altered above T_{cp}, if the initial idea of total dehydrated chain was corrected. In contrary, these results imply that even high above T_{cp} a portion of the directly associated water molecules persists and is not liberated even if the polymer chain is collapsed at a mesoscopic length scale and forms big aggregates. These results are in good agreement with the recent results presented by Philipp et al. [PKS+14] and previous studies [MHI00, KNM+05]. These findings support the idea of residual hydrophilicity in PNIPAM aggregates above T_{cp}, which was also proposed in the previous chapter in order to explain the aggregation behaviour of PNIPAM-rich particles above T_{cp}.

We now turn to the loosely associated water. At 21 °C the D_{jump} for the loosely associated water is almost identical to the one for the pure H_2O:*d*-MeOD (i.e. without polymer). Hence it is not possible at this point to distinguish whether this arrest of the water dynamics are due to water-polymer or water-methanol interactions. A coexistence of both possibilities cannot be excluded at this point. As it has been seen in Ref. [PKS+14], the D_{jump} in the former case (i.e. water:polymmer interactions) is expected also in the same range. It is expected that the strong interaction that defines the first hydration layer (defined here as strongly associated water), induces a further organization of water

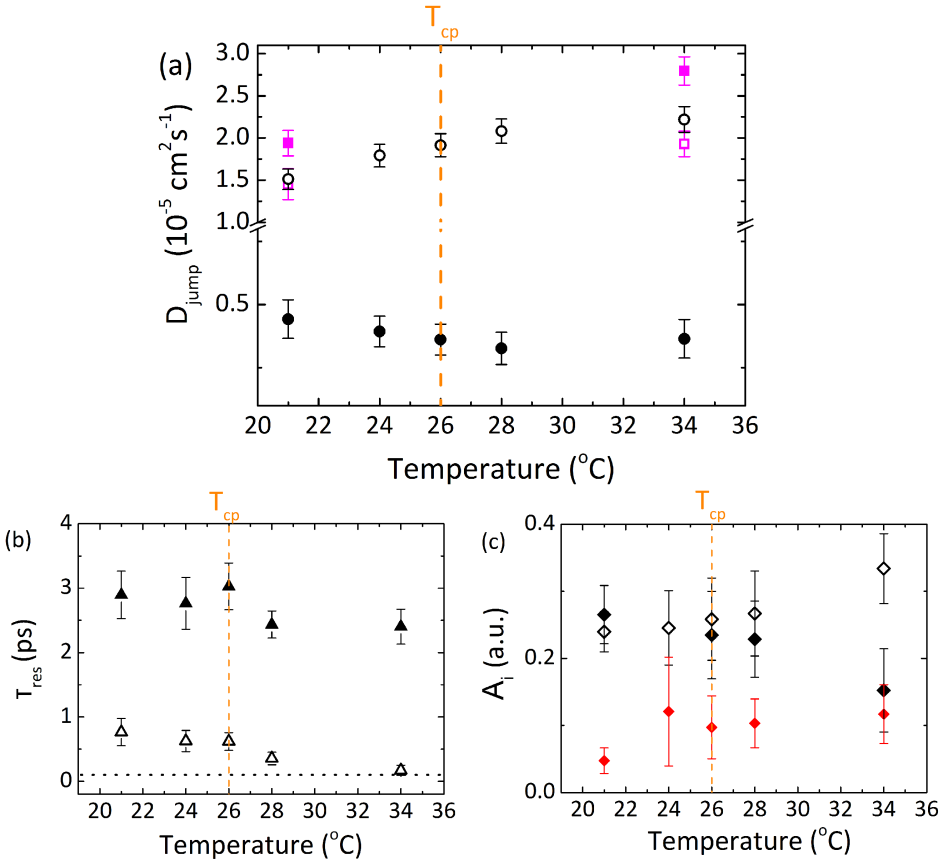

Figure 7.9.: (a) D_{jump} for strongly associated water (black solid circles) and loosely associated water (black empty circles) for the solution of PNIPAM (25 wt.%) in H_2O:*d*-MeOD. The values from pure water (magenta filled squares) and from the pure 85:15 v/v H_2O:*d*-MeOD (magenta empty squares) are also presented for comparison. (b) The residence time τ_{res} for the two populations of water; solid black triangles for the strongly associated population and black empty triangles for the loosely associated population. (c) The amplitudes A_i from the different contributions; black filled diamonds for the strongly associated water, black empty diamonds for the loosely associated water and red diamonds for the local motions. The latter is presented for sake of completeness. In all cases the orange dashed line presents the T_{cp}.

molecules towards the bulk phase. Hence a type of hierarchical, structural organization of water is possible, resulting to a distribution of water populations, than to two distinct populations of bulk and hydration water. An additional structural organization of water molecules around the hydrophobic group of PNIPAM is also possible; the latter is expected to create likewise a population of water with enhanced stability (i.e. slow dynamics) [GRS79, HTW92, SYAM98].

From the analysis we obtain also τ_{res} of the two water populations. The results are presented in Fig. 7.9b. As expected the two different populations exhibit different τ_{res}.

For the strongly associated water τ_{res} is ~ 3 ps at the beginning and interestingly remains unaffected by the T_{cp}. This adds up with the observation about the constant D_{jump} for this population to create a picture of a portion of water molecules strongly interacting with the polymer chain (i.e. via direct H-bonds) and, moreover, part of this population remains unaffected by the T_{cp}. In other words, even high above the T_{cp} some water molecules still reside on the PNIPAM chain, even though the latter is hydrophobic and in the collapsed state. The second population (i.e. loosely associated water) exhibits significantly lower τ_{res} values, which with temperature decrease further, coming closer to the values expected for bulk water. Whether this decrease is related to the switching of the properties of the polymer, is not possible to decide at this point. To complete the picture, we present also the amplitudes (A_i) of the different contributions in Fig.7.9c. This parameter acts as an indication about the amount (number of molecules) that participate in each population. Here an influence of the temperature is observed; i.e. above T_{cp} the $A_{verynarrow}$ decreases in favour of the A_{narrow}. A part of the strongly associated water is liberated and joins the loosely associated water, an observation that can be explained since the conformational changes of the chain at T_{cp} is expected to influence strongly the amount of accessible H bonding sites. We should point out here also that this exchange of amplitudes is not happening abruptly at T_{cp} but rather spans over 5-8 °C. A similar result was reported also in Ref. [PKS+14].

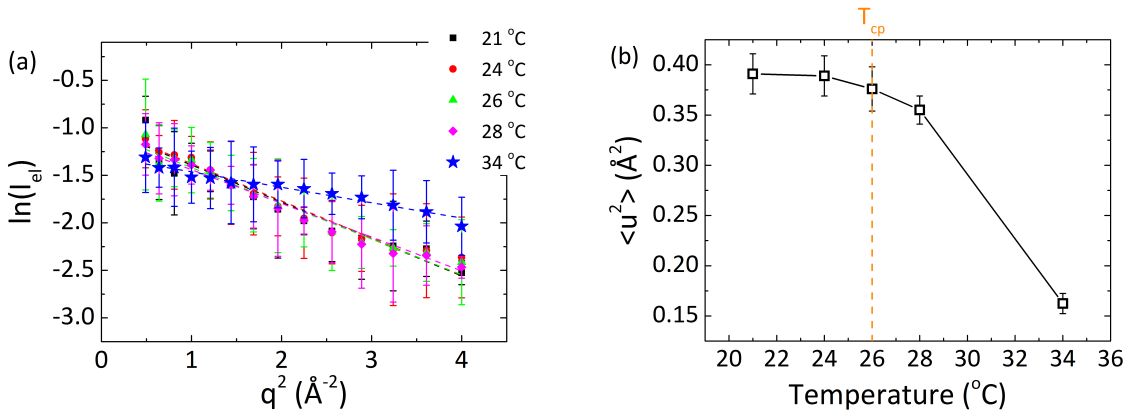

Figure 7.10.: (a) The logarithm of the intensity of the elastic line I_{el} as a function of q^2 at all temperatures measured. The symbols present the data points and the dashed lines the fits of Eq. 3.26 (b) $\langle u^2 \rangle$ of the polymer chain is presented as a function of temperature. The solid black line is a guide to the eye. The orange dashed line presents the T_{cp}.

As it was discussed in section (3.1.4), the elastic line may carry information about the dynamics of the chain, which is expected to be slow enough to contribute to the $I_{elastic}$. Taking into account the latter and using the relation 3.26, we attempt to extract the mean

square displacement $\langle u^2 \rangle$ of the polymer chain as a function of temperature. The result is presented in Figs. 7.10a and b. We observe indeed an effect of the temperature on $\langle u^2 \rangle$. The latter is a quantitative way of describing the mobility of the polymer chain at the different temperatures. As expected, above T_{cp} the $\langle u^2 \rangle$ decreases, reflecting the contraction of the PNIPAM chain in the hydrophobic state. Interestingly, the transition between the swollen state (below T_{cp}) and the collapsed state (above T_{cp}) does not occur abruptly but rather gradually. This is somehow contradictory observation, when compared with the abruptness of the phase transition as observed in the previous two chapters (5 and 6). The reason for this difference can be sought at first in the vastly different length scales that SANS and QENS probe. The behaviour of the chain and/or the solvent molecules at the molecular level play an important role, but it may also be the case that other factors may govern the transition as probed at bigger length scales. Moreover, we have to account also for the different concentrations that we study in the two cases. Here, at 25 wt.%, we are high above the c^*, that defines the critical concentration at which the overlap between neighbouring chains becomes an important issue. So the solution is better described as a pseudo-gel (no chemical or physical crosslinks are present, but overlap of neighbouring chains). In any case the picture obtained here is in very good agreement with the one obtained for τ_{res} (Fig. 7.9b) and with the results offered by Philipp et al. [PKS$^+$14].

Summarizing briefly the so far obtained results, we start with the effect of the methanol on the water dynamics. D_{jump} is strongly decreased upon addition of *d*-MeOD, reflecting the strengthening of the water network due to the kosmotropic effect. We obtain solid experimental evidence for the existence of a water population that interacts very strong with the PNIPAM chain, presumably by direct H-bonds, and thus exhibits severely arrested dynamics. In several previous studies, the existence of this very strongly associated water has been speculated, but to the date, to the best of our knowledge, no unambiguous proof has been offered. Moreover, we observe a second population of water with relatively faster dynamics when compared to the strongly associated water. At this point we cannot argue definitely whether this population resides in hydration shells around methanol molecules, in hydration shells around the hydrophobic moieties of the PNIPAM chain or are just part of the second hydration layer that has decreased dynamics due to the gradual structuring towards the bulk water. A combination of all these three cases can not excluded at this point. At this point, FTIR experiments may reveal important information about the true origin of the loosely associated population. A decrease of the strongly associated water population in favour of the loosely associated is also observed. Based on this picture we will proceed with the analysis of the next step, at which we will focus on the dynamics of the methanol molecules.

7.3.4. MeOH

As before, the results for pure methanol (MeOH) will be presented. This is required, since in the literature data for the diffusion dynamics of methanol is scarce if non existing, especially from QENS. As in the case for pure water we measure here at the two extreme temperatures, at 21 °C and at 34 °C. A representative QENS spectrum is presented in Fig. 7.11. As before, we are obliged to use two contributions described by two Lorentzians (L_i) to fit adequately the data; a narrow one (L_{narrow}) accounting for the long range diffusion of MeOH molecules and a broad one (L_{broad}) accounting for local motions. The full fit and the different contributions are presented in Fig. 7.11. From the analysis we obtain the widths of the two lorentzians (Γ_i) and also the amplitudes. The former are presented for both contributions in Fig. 7.12. L_{broad} (Fig. 7.12b) will not be discussed further, since it comprises a summary of local motions and it is not possible at this stage to decouple. The dependence of L_{narrow} on q^2 can be analysed by the isotropic jump diffusion model, since MeOH molecules form a linear network via H-bonds. The fits are presented also in Fig. 7.12. From the analysis we can obtain the diffusion coefficient D_{jump} for the long range diffusion.

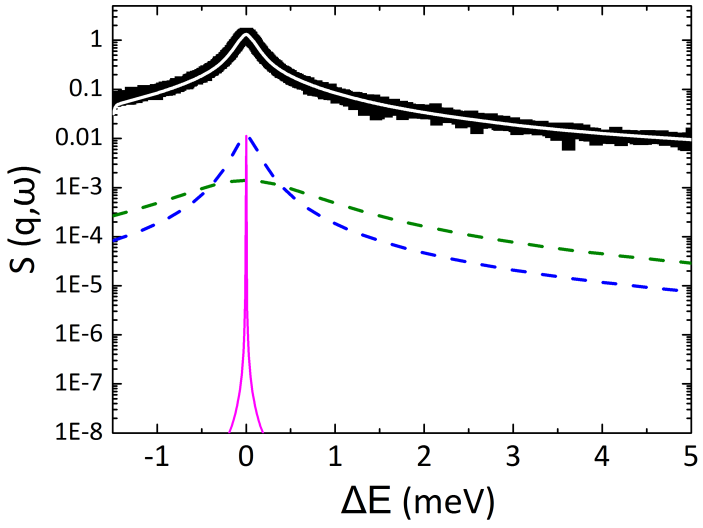

Figure 7.11.: QENS spectrum $S(q,\omega)$ versus energy transfer ΔE for q=1.1 Å^{-1} of pure MeOH at 21 °C. The experimental data are presented by the black squares and the total fit by the solid white line. The different contributions to the fit are presented also; the narrow Lorentzian (blue dashed line) accounting for the long range diffusion, the broad Lorentzian (green dotted line) accounting for local motions and the vanadium measurement (magenta solid line) that defines the resolution.

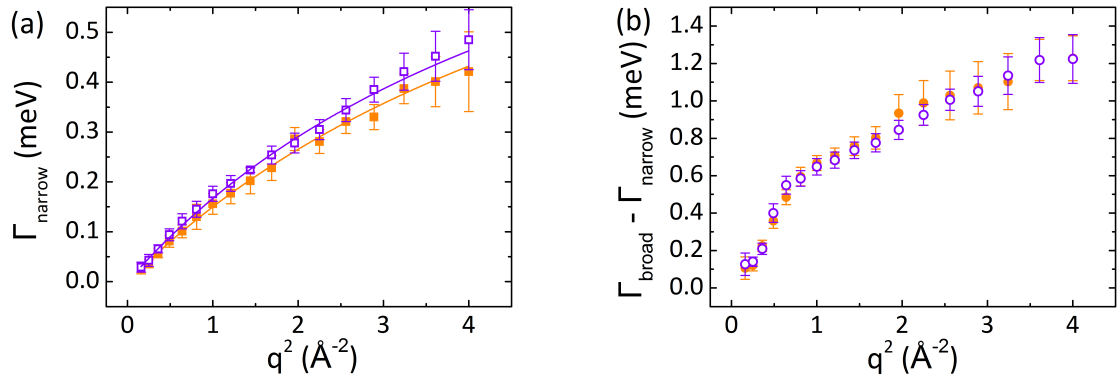

Figure 7.12.: The width Γ of the two Lorentzians as a function of the q^2 at 21 °C (orange solid symbols) and 34 °C (violet hollow symbols) for (a) the narrow Lorentzian describing the long range diffusion of water molecules and (b) the difference of the widths between the narrow and the broad Lorentzian. In (a) the lines present the fits of the isotropic jump diffusion model to the experimental data.

The resulting D_{jump} values are presented in Fig. 7.13, together with data from the literature are presented also for comparison. A small difference between the values obtained here and the ones from literature is observed. A reason for this discrepancy may be the different energy/time scales that is probed in NMR in comparison to the QENS, which is used here. The discrepancy of the values obtained by QENS are again attributed the difference on the energy resolutions of the various set-ups. Thus such a deviation should not be surprising. In any case, the reassuring observation that our data follow the expected T dependence is positive. Furthermore we obtain the τ_{res} of the MeOH molecules and it is found to be 0.039 ps and 0.059 ps at 21 °C and 34 °C, respectively.

7.3.5. MeOH:D_2O 15:85 v/v

In the next step, the data for the mixture MeOH:D_2O 15:85 v/v will be presented. We aim to probe selectively the dynamics of the MeOH molecules. It was proven before in this thesis (7.3.2), that the coexistence of H_2O and MeOH molecules results in a arrest of the diffusion dynamics of the former due to their strong interaction. A similar result is expected also for MeOH. The mixture has been studied again at the two extreme temperatures; at 21 °C and 34 °C. A comparative plot of the QENS spectrum of the pure MeOH and the MeOH:D_2O is presented in Fig. 7.14a. Indeed a slowing down of the dynamics of the MeOH is observed, which is reflected on the narrowing of the QENS

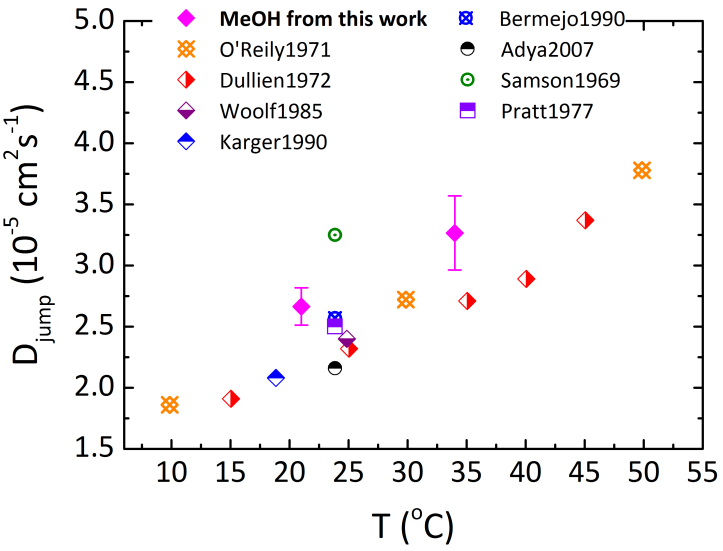

Figure 7.13.: The diffusion coefficient D_{jump} for bulk methanol from this work (magenta filled diamonds) as function of temperature. Values from the literature are also presented for comparison; by NMR: O'Reily 1971 [OP71], Woolf 1985 [Woo85], Karger 1990 [KVL90]; by theoretical modelling: Dullien 1972 [Dul72]; by QENS: Sampson 1969 [Sam69], Bermejo 1990 [BBE$^+$90], Adya 2007 [AKH07]; by flow technique: Pratt 1977 [PW77].

spectrum. For the analysis we use two Lorentzians, one accounting for the long range diffusion and one for local motions (7.14b).

From the analysis, we obtain Γ_{narrow}, which is presented in Fig. 7.15a. The dependence of the Γ_{narrow} on q^2 is modelled by the isotropic diffusion model. The resulting D_{jump} values are presented in Fig. 7.15b. The comparison with the data for the pure MeOH shows a significant arrest of the diffusion dynamics in the presence of D_2O. As expected, the hydration of MeOH by water molecules decreases its ability to move. The values are well separated, and thus allow clear observation of this effect. Moreover, the comparison with literature data reveals good agreement. We also obtain the residence time of the MeOH molecules between each jump, and this is found to be τ_{res}=0.35 ps and 0.40 ps, at 21 °C and 34 °C respectively. In agreement to the D_{jump}, the τ_{res} is strongly affected, thus it increased in the presence of D_2O. From the results presented here, we have a second indication that in water/methanol mixtures, both species suffer from a strong arrest of their diffusion dynamics. The reason is the strong interaction at a molecular level; their ability to form H-bonds leads to hydration of MeOH by H_2O. Based on these results, we will proceed with the analysis of the solution of PNIPAM in MeOH:D_2O.

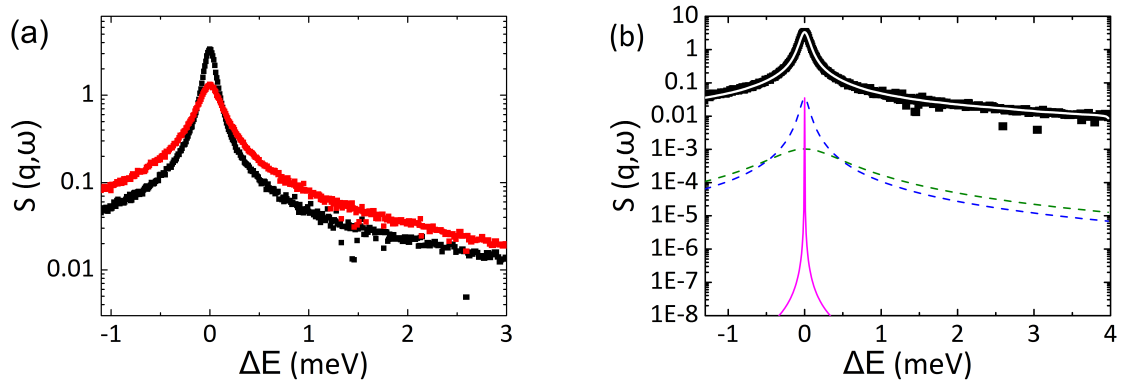

Figure 7.14.: (a) Comparative QENS spectra $S(q,\omega)$ versus energy transfer ΔE for the pure MeOH (black squares) and the MeOH:D_2O mixture (red squares) at q = 1.1 Å^{-1}. (b) QENS spectrum $S(q,\omega)$ versus energy transfer ΔE for q=1.1 Å^{-1} of pure MeOH at 21 °C. The experimental data are represented by the black squares and the total fit by the solid white line. The different contributions to the fit are presented also; the narrow Lorentzian (blue dashed line) accounting for the long range diffusion, the broad Lorentzian (green dotted line) accounting for local motions and the vanadium measurement (magenta solid line) for the elastic line.

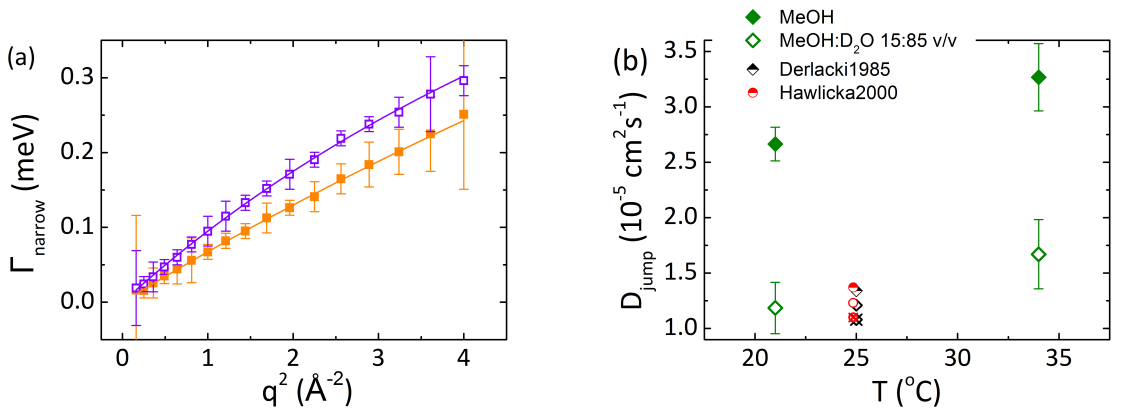

Figure 7.15.: (a) The width Γ_{narrow} describing the long range diffusion of MeOH molecules in the mixture MeOH:D_2O as function of q^2 at 21 °C (orange filled squares) and at 34 °C (violet hollow squares). The dashed lines present the fits of the isotropic jump diffusion model. (b) The diffusion coefficient D_{jump} as result from the analysis of the Γ_{narrow} for MeOH molecules in the mixture MeOH:D_2O (hollow green diamonds). The data for bulk MeOH (filled green diamonds) and data from literature (black half filled diamonds) are also presented for comparison; from NMR: Derlacki1985 [DEE$^+$85] (half filled black diamond for x_{MeOH}=0.05, hollow black diamond for x_{MeOH}=0.10, crossed black diamond for x_{MeOH}=0.15); Hawlicka2000 [HSW00] (red half filled circle for x_{MeOH}=0.05, red hollow circle x_{MeOH}=0.10, red crossed circle for x_{MeOH}=0.15).

7.3.6. 25 wt.% PNIPAM in MeOH:D_2O 15:85 v/v

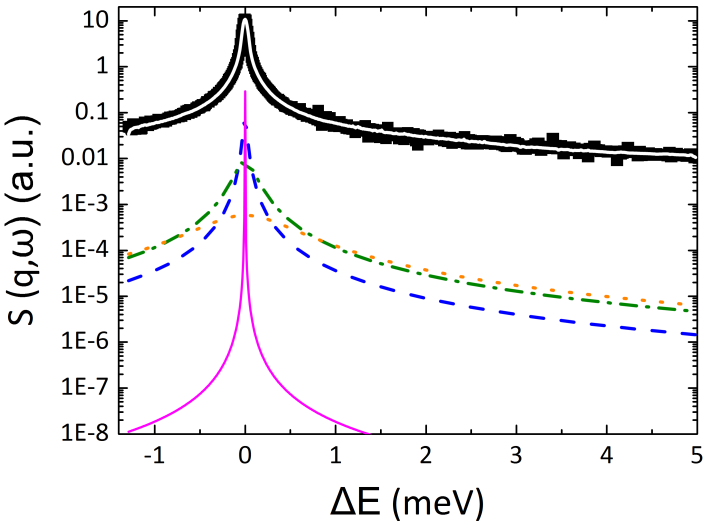

Figure 7.16.: QENS spectrum $S(q,\omega)$ versus energy transfer ΔE for q=1.1 Å^{-1} of 25 wt. % PNIPAM in MeOH:D_2O 15:85 v/v at 21 °C. The experimental data are presented by the black squares and the total fit by the solid white line. The experimental data are presented with the black squares, whereas the total fit by the white solid line. The partial contributions to the total fit are also presented: the $L_{verynarrow}$ describing strongly associated methanol (blue dashed line), the L_{narrow} describing loosely associated methanol (green dash-dotted line) and L_{broad} accounting for local motions of water molecules (orange dotted line). The magenta line gives the elastic line.

The last part of this chapter will discuss the results obtained for the PNIPAM solution at 25 wt. % in MeOH:D_2O 15:85 v/v. We aim here to probe selectively the dynamics of the MeOH in the complex environment. We have obtained the knowledge from the previous part that the coexistence of MeOH and D_2O leads to the hydration of the former and thus to a significant arrest of the diffusion dynamics of both species. Here the question is addressed, whether MeOH interacts with the PNIPAM chain directly or prefers to interact solely with D_2O. Fig. 7.11 shows a representative QENS spectrum at a selected q-value at 21 °C. To analyse the spectra for this solution adequately, we need to use 3 contributions-Lorentzians, similarly to the case of PNIPAM in H_2O:*d*-MeOD (7.3.3). Hence we have a first indication that the MeOH molecules interact strongly with the PNIPAM chain by forming direct H-bonds. We arrive to this conclusion, since a very narrow Lorentzian is required and naturally this is expected to describe a population of MeOH molecules that have significantly arrested dynamics. A second, broader Lorentzian is then used to

describe a second, faster population of MeOH molecules, and as before a third one, very broad, to account for local motions. The latter will not be discussed further. The first two will be analysed on the same framework as before, in order to extract the diffusion coefficients.

The dependence of Γ_i on q^2 for the two cases is presented in Fig. 7.17. The strongly associated population (Fig. 7.17a) shows no dependence on temperature. In contrary, the loosely associated population is influenced by the change of the temperature. From the analysis we obtain at first the D_{jump} for two populations and the result is presented as function of temperature in Fig. 7.18a; the values of the two populations are well separated. Thus, the two different populations indeed describe methanol molecules with different diffusion dynamics. In agreement to the picture obtained for D_2O, the strongly associated population persists also above T_{cp}. Thus, a portion of the strongly associated methanol molecules remains bound on the polymer chain, even if the latter is collapsed. Whether the number of these methanol molecules decreases with temperature, will be clarified by the behaviour of the respective amplitude $A_{verynarrow}$. which will be discussed in the next paragraph. The experimental proof that a portion of the methanol molecules interacts strongly with the PNIPAM chain has an imminent impact on the discussion about the cononsolvency, as well as the fact some of these molecules remain on the chain above T_{cp}. Both observations will be discussed later on.

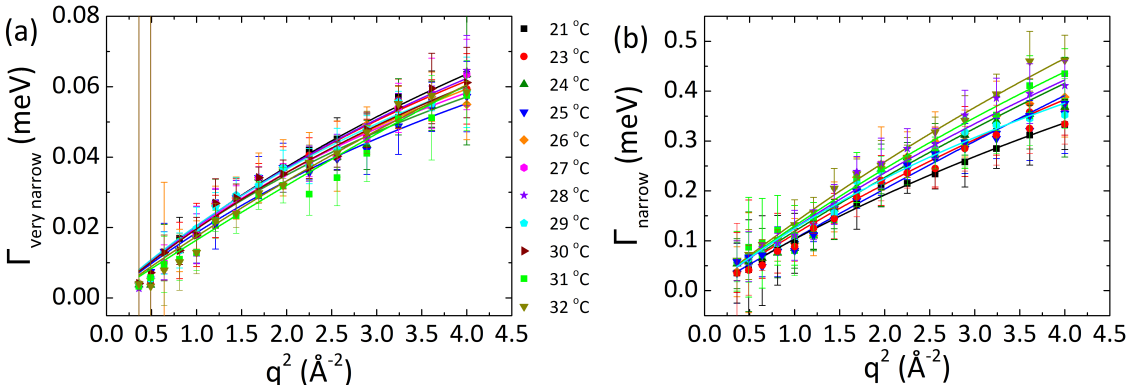

Figure 7.17.: The widths of the Lorentzians describing the two populations of water at all temperatures: (a) $\Gamma_{verynarrow}$ for the strongly and (b) Γ_{narrow} for the loosely associated methanol. The dashed lines present the fits of the isotropic jump diffusion model. The color-symbol scale is the same and is given by the table in the middle.

From the analysis, the residence time τ_{res} and the amplitude A_i of the respective populations are also obtained. Fig. 7.18b and c present the results. The values of τ_{res} of the two populations reflect the picture which was observed also from the D_{jump}; i.e. the

molecules that participate in them exhibit significantly different dynamics. For both populations no strong dependence on the temperature is observed, but they are both rather stable. The A_i (Fig. 7.18c) show that with temperature the number of the strongly associated molecules decreases, in favour of the loosely associated population. This is expected, since the contraction of the chain is expected to reduce the available solvation sites. Interestingly, the decrease is rather mild and in any case smaller than in the case of H_2O (Fig. 7.9). In other words, the comparison between the two species shows that above T_{cp} MeOH resides more preferably on the chain, reflecting the fact that MeOH is a better solvent for PNIPAM.

Elucidating briefly on the origin of the two populations, we can assume that the strongly associated methanol is probably interacting directly with the PNIPAM chain via H-bonds, and thus exhibits strongly arrested dynamics. Here we have a direct experimental evidence, that in the complex solvation environment, the PNIPAM chain is solvated by both species: H_2O (as seen in the previous chapter) and MeOH interact directly via H-bonds with presumably the amide group of PNIPAM [KTI$^+$07]. The latter may act in favour of the model proposed by Tanaka et al. [TKXW11], but we cannot argue at this point against or in favour of the formation of sequences of solvating molecules on the chain. In any case, we observe that the dynamics of the strongly associated MeOH molecules remains unaffected by the T_{cp}. In spite of the apparent, macro- and mesoscopic phase separation, at a molecular level a portion of the MeOH molecules still resides on the PNIPAM chain. Similar observations were made in the previous chapter for the H_2O molecules. Interestingly, we observe that both solvation species reside on the chain even above the T_{cp}, indicating residual solvophilicity. The latter implies that the decisive factor for the solvophobicity of the chain, as it emerges at larger length scales, is the disruption of hydrophobic hydration of the isopropyl group of PNIPAM, rather than the direct solvation on the H-bonding sites.

On the other hand, loosely associated methanol molecules have D_{jump} values between the bulk MeOH and the mixture MeOH:D_2O. Hence the origin of the reduction of the dynamics cannot be determined accurately at this point. We have verified from the previous part of this chapter the formation of hydration shells around the methanol molecules, resulting in a strong decrease of the D_{jump} of both species. Nevertheless, as we can see from Fig. 7.18 the obtained here values are higher than the ones obtained for the MeOH;D_2O, thus it may be the case that the observed here population is not purely associated with D_2O molecules. Association of MeOH with D_2O molecules that participate in the second hydration layer cannot be excluded. In general, the possible association mechanisms for MeOH molecules, except for direct H-bonding that we assumed for the strongly associated MeOH, are three: association with "free" D_2O molecules, association with D_2O

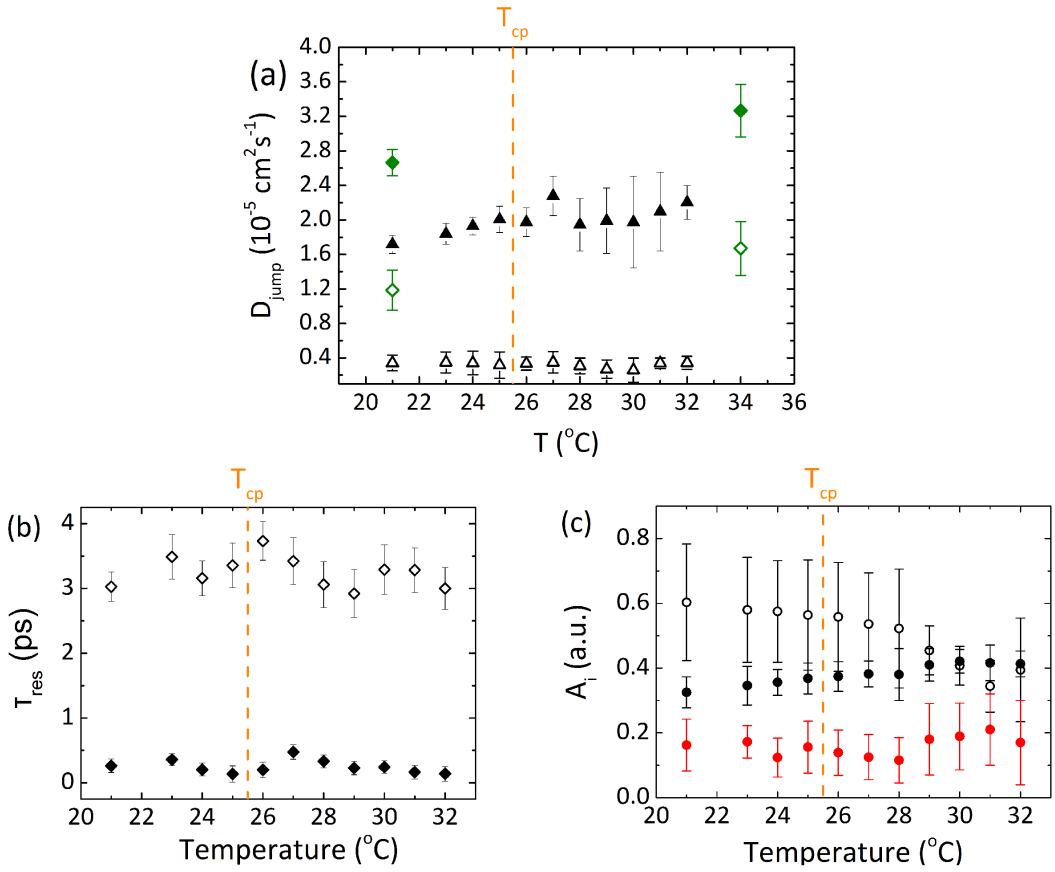

Figure 7.18.: (a) D_{jump} for strongly associated methanol (black empty triangles) and loosely associated methanol (black solid triangles) for the solution of PNIPAM at 25 wt.% in MeOH:D_2O 15:85 v/v. The values for pure methanol (green filled diamonds) and from the pure MeOH:D_2O 15:85 v/v (green empty diamonds) are also presented for comparison. (b) The residence times τ_{res} for the two populations of methanol; filled black diamonds for the loosely associated population and black solid diamonds for the loosely associated population. (c) The amplitudes A_i from the different contributions; black solid circles for the loosely associated MeOH, black empty circles for the strongly associated MeOH and red circles for the local motions. The latter is presented for sake of completeness. In all cases, the orange dashed line presents the T_{cp}.

molecules belonging to the second hydration layer of the PNIPAM and association with D_2O participating in the hydrophobic hydration of the isopropyl group. The latter is the least possible explanation, since it is expected to be rather destabilized than accumulating MeOH molecules in it. Summarizing, it is not possible to distinguish between the above mentioned mechanisms with the so far obtained picture. Future FTIR measurements could act complementary to our results, in order to lighten the true origin of this population.

In the last step we will use the information that the elastic line carries, in order to study the influence of the T_{cp} on the dynamics of the PNIPAM chain, as we did for PNIPAM in H_2O:*d*-MeOD. Fig. 7.19a presents the dependence of the intensity of the elastic line as a function of q^2 for all temperatures. The expected decay is observed, with different slope at different temperatures. We use a modification of 3.26 to analyse the behaviour of $ln(I_{el})$ and extract quantitative information regarding the MSD of the PNIPAM chain in the complex solvation environment as a function of temperature. The result is presented in Fig. 7.19b. As expected, above the T_{cp} the $\langle u^2 \rangle$ decreases, reflecting the contraction of the chain. In agreement with the case of H_2O:*d*-MeOD, we observe the decrease to happen gradually over several degrees, rather than abruptly at T_{cp}.

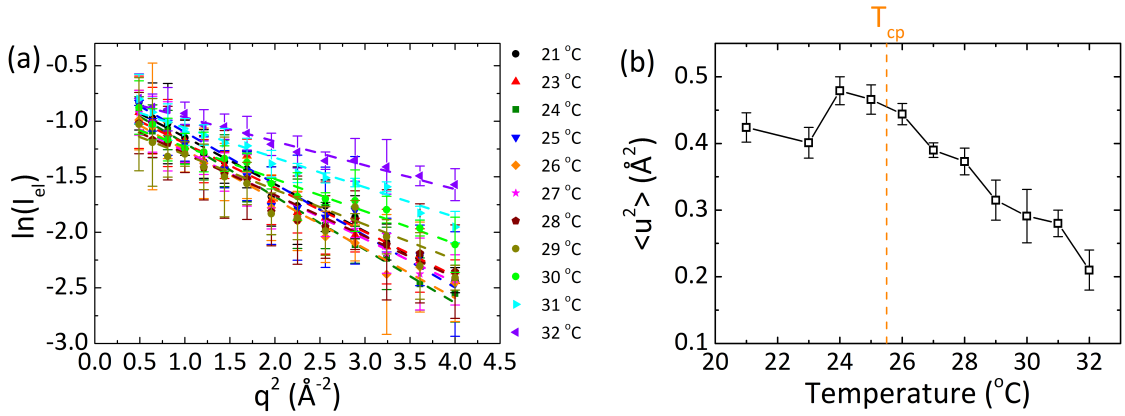

Figure 7.19.: (a) The logarithm of the intensity of the elastic line I_{el} as function of q^2 at all temperatures measured. The symbols present the data points, whereas the dashed lines the fits of Eq. 3.26. (b) The $\langle u^2 \rangle$ of the polymer chain is presented as function of temperature. The solid black line is a guide to the eye. The orange dashed line presents the T_{cp}.

In a partial summary of the study of the diffusion dynamics of MeOH in the complex environment of PNIPAM:D_2O:MeOH, we arrive at some very interesting and important conclusions. We offer solid experimental proof that MeOH molecules reside on the PNIPAM chain, interacting strongly with it. Moreover the influence of the T_{cp} on its behaviour is minor; a small decrease of the amount of the strongly interacting MeOH molecules is observed. This decrease occurs gradually over several degrees and not abruptly, as would someone naively expect. This gradual response of the system on the molecular level is observed also in the behaviour of the MSD of the chain, where the contraction induced by the thermoresponsive switching is followed. From the so far obtained picture it is not possible to argue in favour or against the formation of water and methanol sequences that solvate the chains, as proposed by Tanaka et al. [TKXW11]. In any case the observation of solvating methanol molecules even above the T_{cp} acts in favour of the model

that proposes the hydrophobic solvation of the isopropyl group to be at the origin of the thermoresponsive behaviour, rather than the direct solvation via H-bonds.

7.4. Conclusions

In this chapter of the thesis, the diffusion dynamics of the solvating molecules in the complex environment of a PNIPAM solution at 25 wt.% in H_2O:MeOH (85:15 v/v) was studied. To selectively emphasize on the one of the two solvating components, we use pairs of deuterated and non-deuterated species. The relatively high concentration assures that the majority of the solvation molecules will interact with the polymer chain. Starting from the pure solvents and the mixtures without polymer, we manage to verify the well established kosmotropic effect of MeOH on the H_2O network structure. This is quantified by the arrest of the dynamics of both species with respect to their bulk behaviour, when they coexist. Based on this basis we proceed with the analysis of the diffusion dynamics of both species in the ternary system PNIPAM:H_2O:MeOH.

Starting from the solution of PNIPAM at 25 wt.% in H_2O:*d*-MeOD (85:15 v/v), we aim to elucidate the behaviour of the H_2O molecules. We resolve two populations of H_2O molecules: one loosely and one strongly associated population. The existence of the latter is an interesting and important information, since it verifies the widely accepted idea of the existence of more than one hydration water population around hydrophilic or biologic systems. Evidence for the existence of this water has been previously offered, but a direct, unambiguous observation was not possible [PKS$^+$14]. Here we are able to resolve the dynamics of this portion of strong interacting H_2O and follow its dependence on temperature. Surprisingly a percentage of this water molecules remains on the PNIPAM chain even high above T_{cp}, whereas the rest is liberated. This finding supports the discussion regarding the soft nature of PNIPAM aggregates even in the collapsed state, a factor that defines the aggregation behaviour as this has been discussed in the previous chapters. The origin of this "softness" is the residual hydrophilicity as our QENS data show. Moreover, the unambiguous proof that PNIPAM chains are partially hydrated even above T_{cp} advocates the hydrophobic hydration of isopropyl group of the PNIPAM chain to be the true origin of the thermoresponsiveness. In spite of directly associated water molecules on the PNIPAM chain above T_{cp}, the latter is in the collapsed state. Thus the hydrophobic interaction, that is sheathed under T_{cp}, dominates at T_{cp} as a result of the disruption of the hydration shell around the isopropyl group of the chain and triggers the collapse. The loosely associated population we assign to H_2O molecules interacting either with MeOH or with the isopropyl group of PNIPAM chain (i.e. part of the hydrophobic hydration population). The possibility that this population contains also contributions

from molecules that participate in the second hydration layer (i.e. they are associated to the molecules that consist the strongly associated population, but exhibit faster dynamics) cannot be excluded at this point.

Interestingly, the transition from below T_{cp} to higher temperatures, as reflected in the decrease of the amplitude of the strongly associated in favour of the loosely associated water, occurs over a range of temperatures and not abruptly at T_{cp}. Similar behaviour is also obtained for the $\langle u^2 \rangle$ of the polymer chain, which points to a gradual contraction of the chain. These two facts point out that the phase transition may occur at a mesoscopic and macroscopic length scale relatively fast, but at a molecular level the processes evolve at different rates. It is thus of importance to highlight the difference between T_{cp} as it is defined macroscopically (e.g. turbidimetry) and the processes that govern the phase separation at the molecular level. Under the light of our findings here, the use of the term *dehydration* to describe the phase separation of PNIPAM fails to describe the real situation. The hydrophobic switching is proven to be not governed decisively by the direct hydration of the chain via H-bonds, an effect that persists even high above the T_{cp}, but rather by the hydrophobic hydration that sheaths the hydrophobic character of the isopropyl groups of the PNIPAM chain. As soon as the latter will be unsheathed, the hydrophobicity will dominate and trigger the collapse of the chain that eventually leads to phase separation.

Similar observations are made also for the solution of PNIPAM at 25 wt.% in D_2O:MeOH (85:15 v/v); here we aim to selectively resolve the dynamics of the MeOH molecules. Interestingly we observe two distinct populations of MeOH molecules: one strongly associated (i.e. severely arrested dynamics) and one loosely associated population. The former acts as a direct evidence that MeOH resides on the PNIPAM chain creating direct H-bonds with the amide group. Some studies in the literature argue in favour of the latter observation [WOB$^+$92, OWT01, LBS05, KTI$^+$07]. Taking into account the fact that MeOH is a better solvent for PNIPAM than H_2O (in pure MeOH the thermoresponsivity is lost), the observation of strong interactions between the PNIPAM chain and MeOH molecules is not surprising. Even more interestingly, this strongly associated population of MeOH persists even above the T_{cp}, despite the macroscopic phase separation. Hence, in addition to the picture obtained for the PNIPAM:H_2O:*d*-MeOH, we have here the interesting result that the PNIPAM chain is hydrated by both solvation species, not only below T_{cp}, but also above it. This picture may be at first glance in agreement with the model of competitive hydration model proposed by Tanaka et al. [TKXW11, TKKW11], but we still lack any experimental evidence for the formation of sequences of the two species on the chain.

For the loosely associated MeOH population, several possibilities are offered. At first, the interaction with H_2O molecules via the kosmotropic effect is possible, as it was ob-

served in the previous steps of this experiment. Nevertheless, the deviation observed for the D_{jump} of the of MeOH in the pure (i.e. without polymer) D_2O:MeOH mixture and in the solution of 25 wt.% PNIPAM in D_2O:MeOH proves that other mechanisms should also be considered. From the point of view of D_{jump} and τ_{res} the the diffusion dynamics of MeOH dynamics do not show dependence on the T_{cp}. From the behaviour of amplitudes A_i, we observe a small decrease of the amount of the MeOH that are strongly bound in favour of the ones that are loosely bound, is observed. In comparison to the same behaviour observed for the strongly associated H_2O molecules, the magnitude of the exchange here is significantly smaller. Hence, we can safely assume that the MeOH reside on the PNIPAM chain even above the T_{cp} more preferably than the H_2O. The evolution of this exchange of populations as a function of temperature occurs not abruptly at T_{cp}, but over a wide range of temperatures, similarly to the results obtained for H_2O. In agreement to that, the contraction of the chain, as it is reflected by the $\langle u^2 \rangle$, occurs over 4-5 °C.

As a general conclusion, we offer here direct experimental proof that in mixed solvents of MeOH and H_2O both species create direct H-bonds with the PNIPAM chain. These interactions define a strongly associated solvation population, that persists even above T_{cp}. Hence, the use of the term "dehydration" of PNIPAM chain to describe the phase separation of the solution is not capturing the total magnitude of the phenomenon. The partial solvation of the chain above T_{cp} acts as a hint that the driving force for the demixing of PNIPAM in water or/and in water-methanol mixtures is the hydrophobic hydration of the isopropyl group. As soon as the shielding hydration shell around it is disturbed (due to temperature or solvent composition variations), the chain collapses, despite the fact that a portion of the solvation molecules still occupy sites via direct H-bonds. This finding may have significant impact on the ongoing discussion in literature regarding the functionality-hydration relationship that governs many biomolecules. Under this scope, PNIPAM may act as a model system to exploit the solvation properties of more important biological systems (e.g. proteins).

8. Conclusions and outlook

This dissertation discussed the *cononsolvency* phenomenon, observed in solutions of PNIPAM in mixed solvents of water and short chain alcohols (e.g. methanol). The composition of the solvent has been proven to be an additional trigger for the phase separation, but still the physical reasons, that lie at the origin of this behaviour, are under strong debate. Hence, in this work we aim to add new insights to the existing work, focusing for the first time on the kinetic aspects of the phase transition and the subsequent aggregation of different PNIPAM-based systems in mixed solvents. Additionally, we study the diffusion dynamics of the solvation molecules in ternary mixtures of polymer/water/methanol and establish a new description for the organization of the solvation species in the vicinity of the polymer chain. The latter point is of high significance, irrespective of the presence of alcohol or not, since some aspects of the hydration mechanism of PNIPAM are still unclear.

In the first two experiments presented, TR-SANS is employed to study the kinetics of the aggregation of different PNIPAM-based systems. The combination of high time resolution (0.1-0.2 s) with neutron scattering enables us to follow the formation and growth kinetics of aggregates and extract important information on the link between mesoscopic and molecular level. The two experiments are performed following different pathways to trigger the phase separation and the aggregation.

First, methanol was rapidly added to aqueous solutions of a PNIPAM homopolymer and a PS-*b*-PNIPAM diblock copolymer, resulting in a very fast phase transition. By varying the methanol volume fraction that is added, we prove that the aggregation kinetics is significantly altered by it. Especially in the case of the diblock copolymer, for which the aggregation process evolves slower than in the homopolymer, we obtain experimental evidence that the size and also the speed of the aggregation can be affected but the volume fraction of methanol that is added. Moreover, the aggregation pathway is found to be complex and consist of different regimes. By employing theoretical models we quantify the observations and offer for the first time, to the best of our knowledge, solid experimental proof that the aggregation kinetics and the size of the formed aggregates can be tuned by the addition of different amounts of a cononsolvent. Still, due to the abruptness of the transition that the addition of methanol triggered, information about the early stages

of the process were not captured. Therefore, for the next experiment we changed the selected pathway for introducing the phase separation in the system, aiming to a milder phase separation.

In the second experiment thus, a similar PS-*b*-PNIPAM was predissolved in mixed solvents of water and three different alcohols and TR-SANS measurements were performed during temperature jumps across the respective T_{cp}. The advantage of the diblock copolymer over the homopolymer is that the aggregation proceeds slower and thus can be resolved in more detail, as it was proven in the previous part. The variation of the cononsolvent molecules aims to clarify whether the molar volume of the alcohol influences the aggregation of the system. According to the initial plan, we resolve in this experiment not only the early stages of the aggregation above T_{cp}, but also verify the existence of micelles below T_{cp}, at least in most of the cases. The growth of the aggregates is followed with fine time resolution and is proven to be faster in the mixed solvents when compared with a pure aqueous solution. Moreover, between the mixed solvents, the speed of the growth depends on the molar volume of the alcohol used; i.e. the larger it is, the faster the aggregation evolves. The wealth of our data on the early stages of the process allows the use of a modified version of the reversible association model, that describes the aggregation of colloidal particles. When employed to our data, this model links the mesoscopic length scale with the molecular level. Hence, the interaction potential is extracted, that governs the association of aggregates and a systematic dependence on the composition of the solvation environment is verified. To account for the observations, we propose here a novel model. Water molecules, still forming H-bonds with the PNIPAM above T_{cp} according to several works and according to our findings presented in the final part of this work, create structured layers on the aggregate surface and exert a repulsive, hydration force that mediates the growth. In the presence of alcohol molecules these layers are perturbed, due to the strong interaction between water and alcohol, and thus the repulsive force decreases. Larger alcohol molecules are expected to influence stronger these layers and hence the dependence on the molar volume derived from our data can also be explained. Our results highlight the possibility to tune the interaction potential between particles of thermoresponsive matter, and manipulate the growth of colloidal particles in aqueous media via this route.

In the last part of the work, we choose to change the probed length scales. By employing QENS, the focus is on the diffusion dynamics of two solvation species, water and methanol, in their coexistence in the vicinity of the polymer chain. Our studies validate the discussion presented until now in the literature on the existence of various hydrating water populations. Moreover, we are able to prove the existence of a water population that interacts very strongly with the PNIPAM chain, exhibiting severely arrested dynam-

ics. In spite of the vivid discussion in literature, on the existence of this type of hydrating population, the direct experimental proofs are scarce and thus our results can contribute significantly in this field. Additionally, by varying the temperature we observe that this strongly associated hydrating population persists, even high above T_{cp}. This comes in agreement with previous studies, and also supports the assumption made in the previous part of this work, regarding the existence of residual hydrophilicity on the surface of PNIPAM rich aggregates. Interestingly, when we focus on the other solvating component, i.e. methanol, we obtain a very similar picture. In this case, again two solvating populations are distinguished, a loosely and a strongly associated. The origin of the former is not yet possible to assigned to only one origin, but the latter is assigned to methanol molecules that reside on the PNIPAM chain, interacting via H-bonds with it. This is a direct experimental proof that methanol forms also H-bonds with the PNIPAM chain, in the presence of water. Hence, we offer ,to the best of our knowledge for the first time, experimental proof that in a water - methanol mixed solvent the PNIPAM chain is solvated by both species. The results presented in this part of the thesis can therefore contribute significantly in the vivid discussion on the origin of cononsolvency. Similar to water, also methanol molecules reside on the polymer chain even high above T_{cp}. By comparing the two species, it is found that methanol persists on hydrating PNIPAM above T_{cp} more preferably than water, reflecting presumably the fact that is better solvent for PNIPAM than water.

By capturing, in the above mentioned results, the influence of the solvation environment on a mesoscopic length scale (in chapters 5 and 6) and by studying the local interactions of the two different solvation species, i.e. water and methanol, with each other and with the polymer chain (in chapter 7), we covered a wide spectrum of the questions arising regarding the cononsolvency phenomenon. Of course, open questions still remain and further experiments will certainly add significant information to the ongoing discussion. The study of the PNIPAM chain dynamics in the mixed solvent water - methanol could reveal the influence of the solvation environment on the chain conformation. Neutron Spin Echo (NSE) spectroscopy would be the method of choice, since it is a very powerful technique for studying the local chain dynamics. Preliminary NSE experiments have been already performed during the last stages of this project, but the data analysis is still at a very early stage and further experiments are required in order to create a concrete picture. Another point that would be of interest is the comparison of the different selected pathways to induce the phase separation; i.e. TR-SANS during temperature jumps vs TR-SANS vs methanol content jumps. By comparing data from the two different experiments, we can extract information regarding the influence of the manner that the phase separation is induced on the aggregation kinetics and the size of the formed mesoglobules. The TR-

SANS data obtained during methanol content jumps, that were presented in chapter 6 could be compared with temperature jumps data and reveal important information. The latter experiments have been already performed and the data will be analysed in the near future. At the last point, we should point out that our findings from the QENS data, and especially our experiments at the TOF-TOF cold spectrometer in MLZ, highlight the power of the technique, and especially of the instrument, with respect to studying the diffusion dynamics of the solvation molecules. Taking advantage of this fact, further experiments on PNIPAM solutions in mixed solvents of varying compositions (from purely aqueous to purely methanol) will create the complete story of the solvation mechanism and will allow a better resolution of the composition of the observed solvation populations.

A. Appendix chapter 1

In the following appendix, the data obtained for the poly(methoxy diethylene glycol acrylate) (PMDEGA) system will be presented. PMDEGA is a novel thermoresponsive system, which was recently synthesized for the first time [ML12]. Here, we present a study of different PMDEGA-based systems, homopolymers and amphiphilic block copolymers (with PS as the hydrophobic block), comprising various techniques. The aim is to study the influence of the molecular architecture on the high dilution regime (e.g. CMC, micellar formation) and on the aggregation behaviour above T_{cp} (e.g. size of aggregates). For the former, we employ fluorescence correlation spectroscopy (FCS) and the for the latter dynamic light scattering (DLS) and small angle neutron scattering (SANS). The structure of this part of the work is the following. First, some information is given regarding PMDEGA and its interesting properties. Afterwards, the experimental part starts, where some the experimental techniques used here are presented. The main part follows, where the results are presented and at the end a short summary closes the Appendix.

A.1. PMDEGA

PMDEGA is a novel, non-ionic thermoresponsive polymer that exhibits LCST behaviour and its T_{cp} lies within the most interesting physiological window of 35-42 °C. Hence, it may act as a good candidate for various applications in the future. It exhibits a rather narrow transition (2-3 K), as probed by turbidimetry, whereas no hysteresis upon cooling from above to below T_{cp} is observed. The absence of intramolecular H-bonding sites is probably the reason for that. These facts designate the main differences between PMDEGA and the, extensively studied, PNIPAM system. Amphiphilic block copolymers of PMDEGA have been also synthesized, with PS as the hydrophobic block [ML12, MLDP$^+$12]. It has been shown that in general T_{cp} depends on the molecular architecture, and in more detail that decreases as the complexity increases; i.e. T_{cp} decreases as we go from homopolymer, to diblock copolymer, to triblock copolymer and to starblock copolymers. This observation has been attributed to topological effects. A certain hysteresis of T_{cp} upon cooling observed for the block copolymers has been attributed to the same reason.

In the literature, the references discussing PMDEGA are scarce, since it is a novel material. It has been shown that the behaviour of a PS-*b*-PMDEGA-*b*-PS triblock copolymer above T_{cp} at the semi-dilute regime exhibits unexpected behaviour. Despite the fact that the correlation between micelles weakens abruptly at T_{cp}, the radius shell and the correlation distance do not decrease significantly [MLDP$^+$12]. For similar systems [Ade12], a hysteresis of the structural changes upon heating across T_{cp} has been reported. In all cases, a macroscopic phase separation can be detected (transition from opaque to turbid solutions), since big aggregates are formed. Moreover, PMDEGA films have been studied, in both thick [ZAN$^+$13] and thin film [ZMR$^+$13] morphology.

A.2. Experimental

A.2.1. Fluorescence correlation spectroscopy (FCS)

FCS is a very powerful technique for studying the behaviour of polymer solutions in the high dilution regime [W$\ddot{\text{I}}$4]. The main advantage of the technique emerges from its ability to detect diffusion of tagged, by fluorescence dyes, molecules, even in crowded environments. Thus, it offers the possibility to probe the diffusion dynamics of polymer chains and/or micelles and extract information about their size. Hence, for the case of solutions of amphiphilic block copolymers, the study of the diffusion dynamics (i.e. radius of gyration R_g) as a function of polymer concentration, can reveal the CMC [BLJP07]. In general, it is a very well established experimental technique with many applications in polymer science [W$\ddot{\text{I}}$4, PKRW14].

For the experiments presented here, we used a FCS instrument ConfoCor 2, from Carl-Zeiss Jena GmbH. It was coupled with a He-Ne laser (λ=543 nm). We performed all measurements at room temperature, which was well below T_{cp} of all polymer solutions studied here. The diffusion of the tagged particles, single dissolved chains or micelles, was found by analyzing the autocorrelation function of the fluctuations of the fluorescence intensity $G(\tau)$:

$$G(\tau) = 1 + \frac{1}{N}\left(\frac{T_T}{1-T_T}\right)\exp\left(-\frac{t}{\tau_T}\right) \times \sum_{i=1}^{n} \frac{\rho_i}{\left(1+\frac{\tau}{\tau_{D,i}}\right)\sqrt{1+\frac{\tau}{(z_0/w_0)^2\tau_{D,i}}}} \tag{A.1}$$

where N is the total number of the fluorescent particles in the observation volume, n the number of the different species, $\tau_{D,i}$ the diffusion time and ρ_i the amplitude of the ith species. By z_0 and w_0 we denote the half-height and half-width of the observation volume, which is always at the femto-liter regime. Before each measurement we defined the w_0 by measuring the diffusion time of Rhodamine 6G (Rh6G, Sigma-Aldrich, D_{Rh6G} =

2.8×10^{-10} m^2s^{-1} [MEW74]), by using the relation $w_0 = \sqrt{4D_{Rh6G} \times \tau_{D,Rh6G}}$. In all cases, w_0 was found to be at values $\sim 0.2\ \mu m$. T_T and τ_T are the triplet function and time, respectively. We found values in the range $T_T = 0.05 - 0.1$ ms and $\tau_T = 0.005 - 0.01$ ms.

In the next step, the hydrodynamic radii $R_{h,i}$ of the ith species was found via the Stokes-Einstein relation

$$R_{h,i} = \frac{k_B T}{6\pi\eta \mathrm{D}_i} \tag{A.2}$$

where k_B is the Boltzmann constant, T the temperature and η the solvent viscosity (10^{-3} Pa at room temperature). The preparation of the samples was done in the following way: first stock solutions of labelled and non-labelled polymer were prepared and then they were mixed accordingly in order to achieve the desired polymer concentration. To avoid saturation of the fluorescent signal, the concentration of the labelled polymer chains was kept below 10^{-8} mol/L.

A.2.2. Dynamic light scattering (DLS)

DLS is one of the most widely used techniques for studying polymer solutions [BP76, Bro93, Sch07]. Among other quantities, it offers also an insight into particle sizes and thus can act as a first step analysis of the behaviour of polymer solution in the dilute regime. Here, temperature-resolved DLS measurements were performed in polarized geometry with an ALV-5000/E correlator, coupled with a goniometer. We used toluene as index-matching material. The light source was a laser Nd:YAG ($\lambda = 532$ nm). Measurements were performed at angles between 30 ° and 150 ° in steps of 5 ° or 10 °, using a photomultiplier to which the signal was fed by an optical fibre. The concentration was always 2 g/L and the samples were prepared 3 days before each experiment. The last step before measuring was to filter the solutions before mounting them in the cuvette, in order to avoid contamination of the measurement by large particles (e.g. dust, undissolved polymer aggregates, etc.). At each angle the measuring time was 60-90 s and 3 runs were performed. The equilibration time at each temperature was 15 min.

The analysis of the obtained intensity correlation functions $G_2(\tau)$, were analysed with the REPES routine (i.e. by inverse Laplace transformation) [Jak88]. The distribution function of relaxation times was found and the mean relaxation time of each mode was extracted from the centers of mass of the peaks. Thus the diffusion coefficients D were determined from the $\Gamma = Dq^2$, where Γ is the inverse of the characteristic time and $q = 4\pi n \sin(\theta/2)/\lambda$ is the scattering vector. Here n is the refractive index of water (n_{water}=1.333). Similarly to the previous paragraph, the radius was then calculated by using Eq. A.2.

A.2.3. Small-angle neutron scattering (SANS)

A detailed discussion regarding the method was presented in chapter 3. The temperature-resolved measurements presented here were performed at the SANS instrument KWS-2 of JCNS, at the reactor MLZ, in Garching, Germany. The selected wavelength was $\lambda = 0.45$ nm ($\Delta\lambda/\lambda = 20$ %). Three SDD's were chosen: 1.36, 4.00 and 20.0 m. This set-up allowed a q-range of 0.035-2.1 nm^{-1}. The accumulation times were 5 min, 10 min and 20 min at 1.36 m, 4.00 m, and 20.0 m, respectively. A Peltier oven (precision $\pm$0.1 K) was used for the heating of the samples, which were mounted into standard Hellma cuvettes with a nominal light path of 2 mm. The 2D images were azimuthally averaged and brought to absolute units by measuring plexiglass and boron carbide. The obtained curves were background-corrected. All operations were performed using QtiKWS software, provided by JCNS.

The polymer solutions were prepared 1 week before the SANS beamtime and kept then at 4 °C. The polymer concentration was 100 g/L, i.e. in the semi-dilute regime. We have selected an amphiphilic diblock copolymer P(S-d_8)$_{11}$-b-PMDEGA$_{505}$, which is expected to form star-like micelles. The choice of a deuterated PS block offers the required contrast for resolving the core-shell structure of the micelles and emphasize on the shell behaviour as a function of the temperature. Due to the relatively high concentration, a level of correlation between the micelles is also expected and thus, in contrary to the previous SANS results presented in this thesis, here the use of a structure factor is to be expected.

For the modelling of the SANS curves, we used a model that combines a form factor for core shell micelles $P_{mic}(q)$ (see paragraph 4.1.3) together with a hard spheres structure factor $S_{HS}(q)$ and the Ornstein-Zernike term $I_{OZ}(q)$ accounting for density fluctuations of the swollen micellar shell (see paragraph 4.1.5) . In addition to these terms, we add also a $I_{agg}(q)$ term to describe scattering from large aggregates. Thus the total fitting function reads

$$I(q) = I_{agg}(q) + P_{mic}(q)S_{HS}(q) + I_{OZ}(q) + I_{bkg} \tag{A.3}$$

where I_{bkg} is the incoherent background. The use of the $I_{agg}(q)$ was required around T_{cp}, where the forward scattering was not negligible any more. Just above T_{cp}, the following expression was used [PPM92]

$$I_{agg}(q) = \frac{K}{1 + 0.22(qr_{agg})^{\alpha}} \tag{A.4}$$

with K a scaling constant, r_{agg} the aggregate radius and α an exponent describing the surface of the aggregates. Values $\alpha \sim 3$ were always obtained, giving evidence of a finite surface roughness [Sch82]. Far above T_{cp} the strong forward scattering was dominating the scattering signal, and therefore the Porod term (see paragraph 4.1.4) was used for $I_{agg}(q)$. Here, α was typically in the order of 5.1 $\pm$ 0.1; i.e. a concentration gradient is present at the aggregate surface. The hard sphere structure factor $S_{HS}(q)$ reads

$$S_{HS}(q) = \frac{1}{1 + 24\eta_{HS}G(2r_{HS}q)/(2r_{HS}q)} \tag{A.5}$$

where r_{HS} is the radius of the hard spheres, which here is equivalent to half the distance between the centers of two micelles, η_{HS} is the volume fraction occupied by the hard spheres and G_χ is defined as

$$\begin{aligned} G(\chi) = \gamma\frac{\sin\chi - \chi\cos\chi}{\chi^2} + \delta\frac{2\chi\sin\chi + (2-\chi^2)\cos\chi - 2}{\chi^3} + \\ \epsilon\frac{-\chi^4\cos\chi + 4(3\chi^2 - 6\cos\chi + (\chi^3 - 6\chi)\sin\chi + 6)}{\chi^5} \end{aligned} \tag{A.6}$$

with the help functions

$$\gamma = \frac{(1 + 2\eta_{HS})^2}{(1 - \eta_{HS})^4} \tag{A.7}$$

$$\delta = \frac{-6\eta_{HS}(1 + \eta_{HS}/2)^2}{(1 + \eta_{HS})^4} \tag{A.8}$$

$$\epsilon = \frac{\gamma\eta_{HS}}{2} \tag{A.9}$$

Depending on the temperature, some terms of the total fitting expression Eq. A.3 were not required. Below T_{cp} no aggregates were present, thus $I_{agg}(q)$ was set to zero. Just above T_{cp}, due to the ongoing structural reorganization of the system, the correlation of the micelles was lost and therefore $S_{HS}(q)$ was set to unity. The $P_{mic}(q)$ was used throughout the whole temperature range probed here. Since P(S-d_8) is not thermoresponsive and not soluble in D_2O, r_{core} was kept constant at 2.7 nm. Regarding the SLD values, ρ_{core} and $\rho_{solvent}$ were set at the nominal values for P(S-d_8) (6.52 $\times$ 10^{-4} nm^{-2}) and D_2O (6.36 $\times$ 10^{-4} nm^{-2}), respectively. The ρ_{shell} was left as free variable and was found always to be $\approx$1.55 $\times$ 10^{-4} nm^{-2} (the SLD of PMDEGA is estimated to be 1.37 $\times$ 10^{-4} nm^{-2}). The slight increase may originate from the fact that the shell contains a significant amount of D_2O.

A.3. Results

The complete list of the polymers studied in this part of the thesis is given in Table A.1. The respective T_{cp} values are also given. The different systems were studied by different techniques. More information will be given in the forthcoming paragraphs.

polymer	T_{cp} (°C)[a]
homopolymer	
$PMDEGA_{543}$	39.0
diblock copolymers	
PS_{11}-*b*-$PMDEGA_{172}$	38.0
PS_{11}-*b*-$PMDEGA_{275}$	39.0
$P(S\text{-}d_8)_{11}$-*b*-$PMDEGA_{505}$	38.5
triblock copolymers	
PS_9-*b*-$PMDEGA_{360}$-*b*- PS_9	37.0
$P(S\text{-}d_8)_9$-*b*-$PMDEGA_{353}$-*b*-$P(S\text{-}d_8)_9$	36 .0
$P(S\text{-}d_8)_9$-*b*-$PMDEGA_{665}$ - *b*-$P(S\text{-}d_8)_9$	38.0
starblock copolymer	
$(PMDEGA_{219}$-*b*-$PS_8)_3$	37.0

Table A.1.: List of studied polymers. The respective T_{cp} values are also given.
[a] As measured by turbidimetry [KAA+14].

A.3.1. FCS

First, the results obtained from FCS will be presented. Here, we discuss data obtained for three different architectures, namely, PS_{11}-*b*-$PMDEGA_{172}$, PS_9-*b*-$PMDEGA_{360}$- *b*- PS_9 and $(PMDEGA_{219}$ - *b* - $PS_8)_3$. Some representative autocorrelation curves are presented in Fig. A.1. As the concentration increases, we observe an abrupt change of the shape of the curves. As soon as the CMC is crossed, micelles are formed and contribute to the scattering signal. The analysis is done by using Eq. A.1, in dependence of the type of diffusing molecules present. Below CMC, a single exponential (i.e. $i = 1$) is sufficient to describe the curves, since only unimers are present. After the CMC is crossed, micelles are formed and a second, slower contribution is required to describe the data. Here we use Eq. A.1 with $i = 2$. Some representative fits are presented also in Fig. A.1. From the analysis the Γ_i values for the unimers and micelles are obtained and from these the respective hydrodynamic radii r_h can be derived. The results are compiled in Fig. A.2.

As expected, in all cases we observe unimers (∼1 nm) below CMC and micelles (∼10.2-12.8 nm) above it. The comparison between the different systems reveals that the CMC of the starblock copolymer lies in the same regime with the other copolymer systems. The latter is an interesting result, since it reveals that the steric hindrances originating from the uncommon architecture of this polymer does not affect so strongly the CMC. In general, we observe an increase of CMC as we increase the complexity of the architecture, going from diblock to starblock and to triblock. The CMC's are found at $1.4 - 7 \times 10^{-8}$ mol/L. As a general comment we can argue that neither the hydrodynamic radii nor the CMC's are strongly dependent on the polymer architecture.

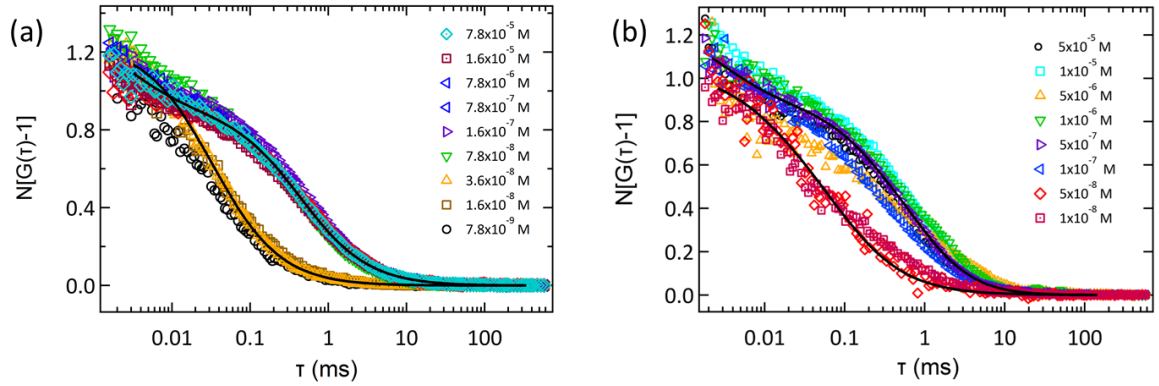

Figure A.1.: Autocorrelation functions for the (a) PS_9-*b*-$PMDEGA_{360}$-*b*-PS_9 and (b) $(PMDEGA_{219}$-*b*-$PS_8)_3$ for all studied polymer concentrations. The solid lines show some representative fits.

A.3.2. DLS

In this part of the appendix, the hydrodynamic radius of various PMDEGA-based polymers is studied as a function of temperature. DLS measurements are facilitated here to reveal the transition from swollen micelles below T_{cp} to aggregates above T_{cp}. The polymers studied here are the following: a $PMDEGA_{534}$ homopolymer, a PS_{11}-*b*-$PMDEGA_{275}$ diblock, a PS_9-*b*-$PMDEGA_{360}$-*b*-PS_9 triblock and a $(PMDEGA_{219}$-*b*-$PS_8)_3$ starblock copolymer. In all cases, the polymer concentration was 2 g/L. At this concentration we expect the copolymer systems to form micelles, since it is much higher than CMC. The autocorrelation curves for the copolymers are presented at selected temperatures in Fig. A.3.

A clear transition across the T_{cp} is observed. Below T_{cp} the curves represent a fast mode, which is attributed to single, swollen chains in the case of $PMDEGA_{534}$ and swollen micelles for the copolymer systems. As soon as the T_{cp} is crossed, PMDEGA collapses

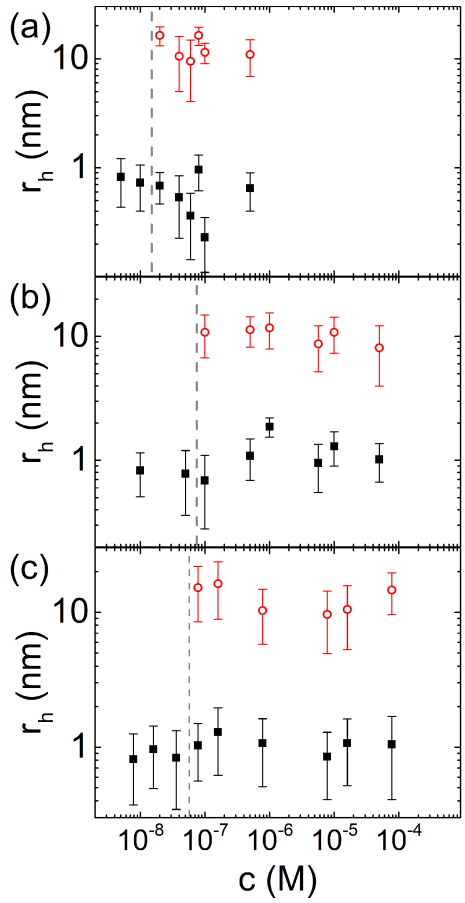

Figure A.2.: Results from FCS. The hydrodynamic radius of unimers (black solid squares) and micelles (red empty circles) as a function of polymer concentration for (a) PS_{11}-*b*-$PMDEGA_{172}$, (b) PS_9-*b*-$PMDEGA_{360}$-*b*-PS_9 and (c) $(PMDEGA_{219}$-*b*-$PS_8)_3$.

and this leads to the formation of aggregates, consisting of collapsed chains in the case of the homopolymer and of collapsed micelles in the case of the block copolymers. The decay time of the autocorrelation function slows therefore down. The curves are analysed by using the REPES routine, as explained in the previous section. In the case of the homopolymer, the analysis above T_{cp} was not possible, most probably due to multiple scattering, originating from the very large aggregates. The fits are also presented in Fig. A.3.

In all other cases, the size could be resolved. For the various systems we observe the following behaviour below T_{cp}. In the case of the homopolymer, r_h is ~ 6 nm, which is in good agreement with the expected value for a single, swollen chain in good solvent conditions. The data for the block copolymers are compiled in Fig. A.4. For PS_{11}-*b*-$PMDEGA_{275}$ a decrease of r_h is observed from 10.9 ± 0.1 to 10.2 ± 0.1 nm. The value

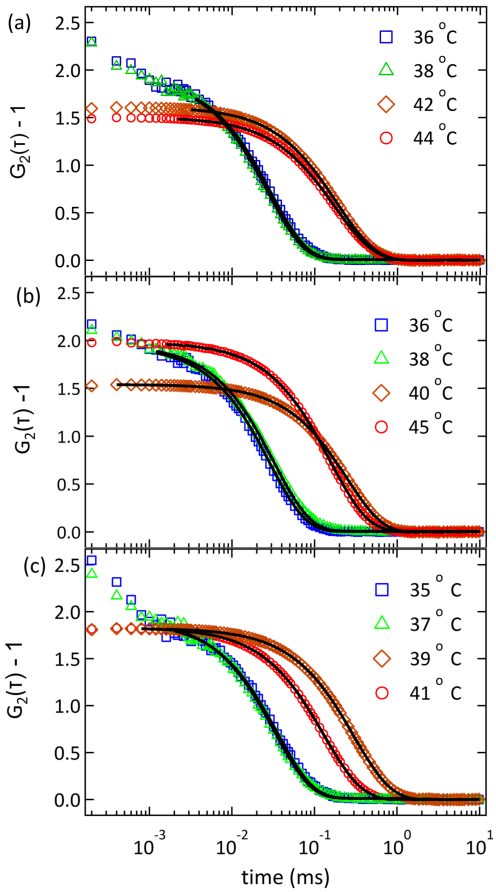

Figure A.3.: Autocorrelation functions at $\theta = 90^o$ for the (a) PS_{11}-*b*-$PMDEGA_{275}$ diblock, (b) PS_9-*b*-$PMDEGA_{360}$-*b*-PS_9 triblock and (c)$(PMDEGA_{219}$-*b*-$PS_8)_3$ starblock copolymer at two temperatures below and two above T_{cp}. The solid black lines present the fits.

found here is slightly lower than the one found by FCS for a diblock with longer PMDEGA block. This is maybe due to different weighting of the size distribution in the two methods. For the triblock PS_9-*b*-$PMDEGA_{360}$-*b*-PS_9 a similar decrease from 11.3±0.1 to 9.7±0.1 nm is observed, as well as for the starblock $PMDEGA_{219}$-*b*-$PS_8)_3$ from 13.0 ± 0.1 to 12.1 ± 0.1 nm. For the two latter systems the values are consistent with the findings by FCS. The T_{cp} values are found to be in the range 38 - 41 °C and, as expected, and to increase as the complexity of the system decreases.

Above T_{cp}, PMDEGA collapses and becomes hydrophobic. In the case of homopolymer, the size of the aggregates exceeds the resolution limit of the instrument, therefore we could not resolve the size of the aggregates. For the block copolymers, we obtain radii between 45 and 108 nm; i.e. large aggregates are formed as expected. When compared to the

PNIPAM aggregates (mesoglobules), the sizes obtained for PMDEGA lay in the same range and are also stable for relatively long times.

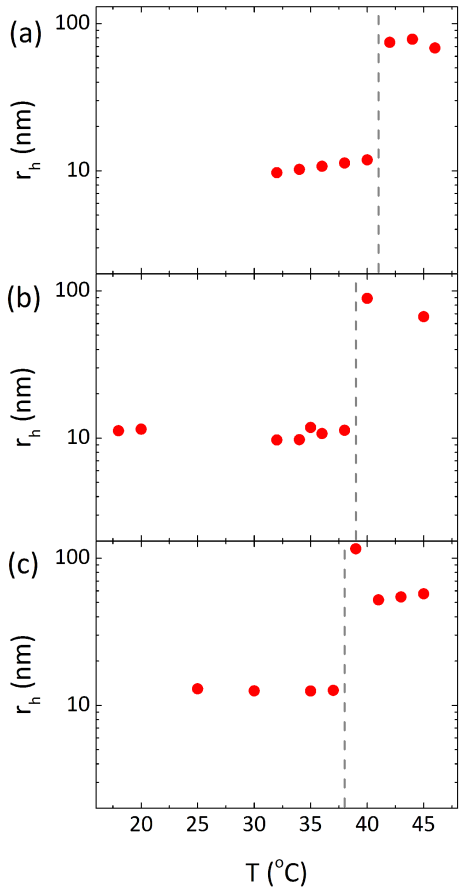

Figure A.4.: The hydrodynamic radii R_h obtained by the DLS measurements for (a) PS_{11}-*b*-$PMDEGA_{275}$ (b) PS_9-*b*-$PMDEGA_{360}$-*b*-PS_9 and (c) $(PMDEGA_{219}$-*b*-$PS_8)_3$ as a function of temperature.

A.3.3. SANS

In this part of the appendix, the SANS results will be presented. The focus here is on the inner structure and the correlation of the micelles formed by the $P(S\text{-}d_8)_{11}$-*b*-$PMDEGA_{505}$ diblock copolymer. The concentration used here is 100 g/L, so higher in comparison to previous cases studied by FCS and DLS. We expect this fact to upgrade the correlation between micelles to an important factor. The T_{cp} was found at 38.5 °C (see Table A.1). The SANS experiments were performed in dependence of the temperature. The fact that the PS block is fully deuterated enables us to focus on the thermoresponsive PMDEGA shell.

Representative curves are presented in Fig.A.5. Qualitatively we can see a peak at $\sim$ 0.18 nm^{-1} at 25 °C, which is assigned to the correlation of the micelles. A shoulder appears at higher q values, together with a smoothly decaying shoulder. As the temperature increases, the shoulder weakens and the forward scattering increases. This acts as a sign of the forthcoming phase transition and the formation of large aggregates at the later stages. Above 41 °C the curve shape changes drastically; i.e. the scattering intensity of the correlation peak and below is reduced, in favour of the forward scattering. This observation shows clearly the formation of large, polymer rich aggregates. Moreover, the correlation peak shifts to higher values, thus we can assume that the correlation distance decreases. At even higher temperatures (48 °C) the correlation peak vanishes completely. All these observations signal the gradual transition of the structure.

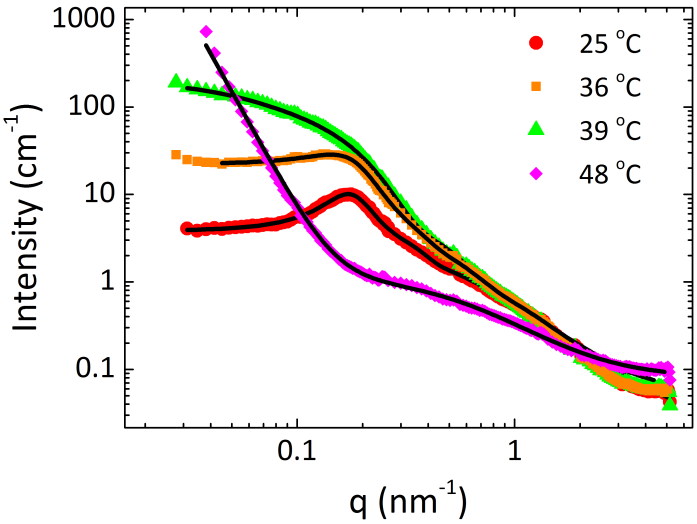

Figure A.5.: Representative SANS curves of P(S-d_8)-*b*-PMDEGA$_{505}$ at a concentration of 100 mg/ml in D_2O at various temperatures (symbols) together with model fits (solid lines).

In order to quantify our results, we continue with modelling of the curves. To capture the different states of the system at the various temperatures, different models are used. The best fits are shown in Fig. A.5. Below T_{cp} we use Eq. A.3 and set $I_{agg}(q) = 0$ since no aggregates are expected. At higher temperatures the complete expression is required. The model is found to describe adequately the curves. As a general picture, the diblock copolymers are forming core-shell micelles, which are strongly correlated. This correlation is described by the hard-sphere structure factor. Density fluctuation within the swollen PMDEGA shell give rise to a weak scattering signal at higher q-values.

The resulting coefficients are presented in Fig. A.6. The core radius r_{core} was fixed at 2.5 nm. At 25 °C, the shell radius is 5.5 ± 0.3 nm and increases with temperature, even across T_{cp}. Finally it reaches a value at 8.8 ± 1.1 nm at 41 °C. When compared these values, to the ones presented above from DLS, a good agreement is obtained. In the range from 41 °C to 44 °C, the r_{shell} decreases abruptly to 3.5 nm. The characteristic length of the density fluctuations, ξ, is $1.5 - 2.5$ nm close to T_{cp}. Above it, decreases, as it is expected for collapsed PMDEGA chains. It is interesting that ξ never reaches zero; i.e. even high above T_{cp} solvent molecules still reside in the polymer rich aggregates.

Regarding the correlation of the micelles, the r_{HS} is 16.7 ± 0.7 nm at 25 °C and decreases as T_{cp} is approached. In the range 38.5 to 41.0 °C, the structure factor could not be used. The correlation is thus lost in this temperature regime. Afterwards, correlation is reinstalled. Now r_{HS} is smaller, namely 9.6 ± 0.6 nm. The volume fraction η_{HS} is initially 0.19 ± 0.02 and decreases to 0.11 ± 0.03 at 38 °C, then the correlation is lost, and when it is reinstalled η_{HS} is relatively high (0.20 ± 0.02); i.e. the micelles are well correlated above T_{cp}. From T_{cp} and onwards, large aggregates are present. Their size starts from $32.7, 1.7$ nm at 38.5 °C and reaches 42.2 ± 2.1 nm at 39.5 °C. Later on, their size increases above the resolution limit of the set-up.

A.4. Conclusions

In this part of the work, the results obtained for the novel thermoresponsive PMDEGA were presented. This material is of interest, since it bears characteristics that make it a possible substitute material in many applications. Here, we study in the first step the influence of the architecture on the high dilution regime. We employ FCS to find the CMC and the micellar radius for three different block copolymers: a diblock, a triblock and a starblock copolymer. No strong influence of the architecture on these two quantities is observed. On solutions with higher concentrations and of various architectures, we employ DLS to study the micellar radii below T_{cp}, and the aggregate radii above T_{cp}. We find a good agreement between the two methods below T_{cp}. In the last step, we employed temperature resolved SANS to elucidate the structural changes induced by the phase transition in a solution of a amphiphilic diblock copolymer. We resolve the micellar structure and follow its evolution with temperature.

Interestingly, we see that the micellar structure is preserved even at and slightly above T_{cp}. At higher temperatures the micellar shell collapses totally. Regarding the correlation of the micelles, it is lost at T_{cp} and reinstalled at higher temperature. Comparing the behaviour of the system, as observed by the DLS and SANS, we see that the two methods reveal different information. Despite the fact that DLS reveals the formation of big

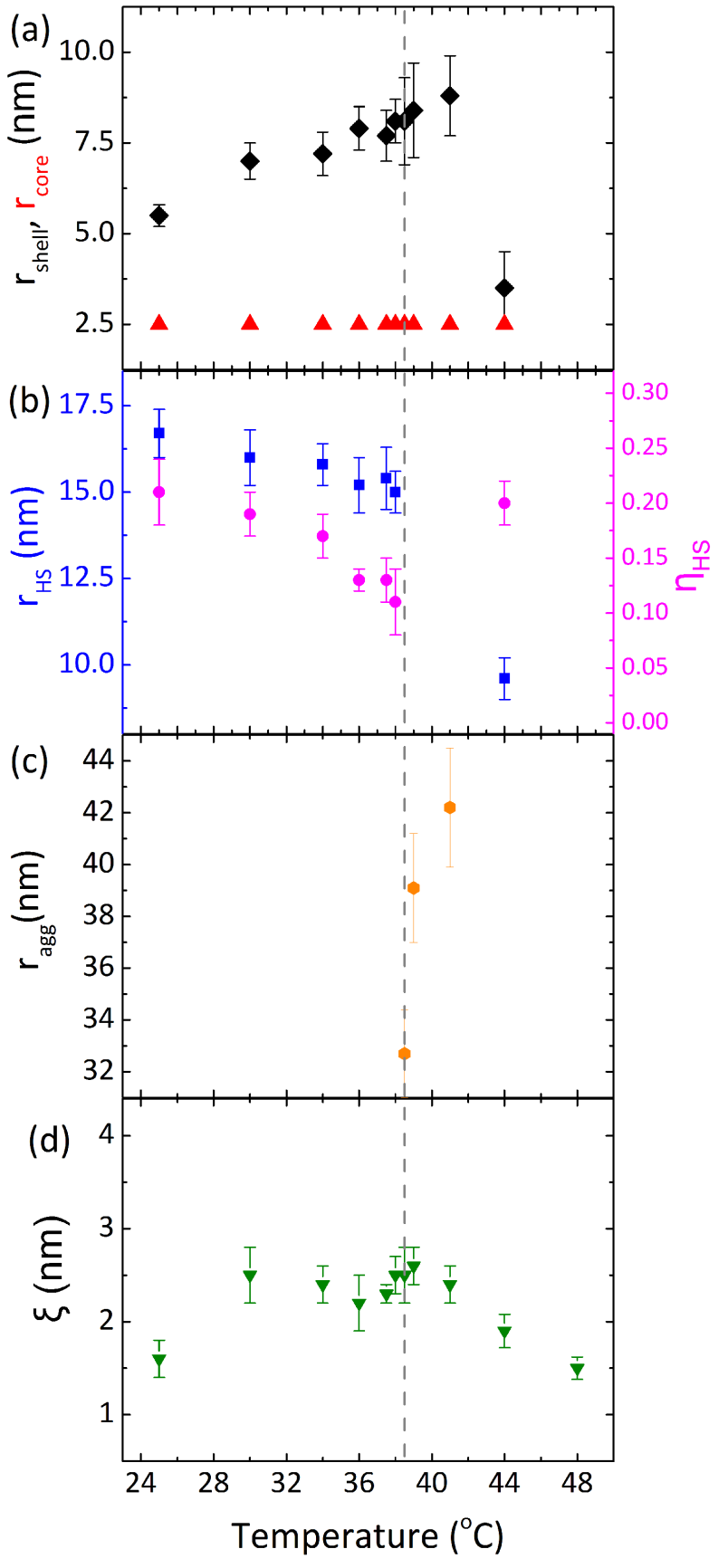

Figure A.6: SANS results. Fit parameters for P(S-d_8)$_{11}$-*b*-PMDEGA$_{505}$ at 100 g/L in D_2O as a function of temperature:(a) the radius of the micellar shell r_{shell} (black diamonds) and the radius of the core r_{core} (red triangles) from the form factor for core shell micelles; (b) the hard-sphere radius r_{HS} (blue squares) and the volume fraction η_{HS} (magenta circles) from the structure factor; (c) the radius of the formed aggregates r_{agg} at and above T_{cp} (orange circles); (d) the characteristic length ξ (green down triangles) of the density fluctuations within the PMDEGA shell. The grey dashed line shows the T_{cp}.

aggregates at T_{cp}, the structural changes evolve much slower. For example, the micellar shell collapses completely only above 41 °C, so appr. 3 grads above T_{cp}.

The results of this study are part of a broader work published recently [KAA+14].

Bibliography

[ADA00] K. F. Arndt, Kuckling D., and Richter A. *Polym. Adv. Technol.*, 11:496–505, 2000.

[Ade12] J. Adelsberger. *Struktur und Kinetic thermoresponsiver Hydrogele*. PhD thesis, Physics Department, TU München, 2012.

[AGK+13] J. Adelsberger, I. Grillo, A. Kulkarni, M. Sharp, A. M. Bivigou-Koumba, A. Laschewsky, P. Müller-Buschbaum, and C. M. Papadakis. *Soft Matter*, 9:1685–1699, 2013.

[AHL+05] V. Aseyev, S. Hietala, A. Laukkanen, M. Nuopponen, O. Confortini, F. E. Du Prez, and H. Tenhu. *Polymer*, 46:7118–7131, 2005.

[AKA+10] J. Adelsberger, A. Kulkarni, J. Abhinav, W. Wang, A. M. Bivigou-Koumba, P. Busch, V. Pipich, O. Holderer, T. Hellweg, A. Laschewsky, P. Müller-Buschbaum, and C. M. Papadakis. *Macromolecules*, 43:2490–2501, 2010.

[AKH07] A. Adya, O. Kalugin, and W. Howells. *Journal of Physics: Condensed Matter*, 19(41):415120, 2007.

[AL00] P. Alexandridis and B. Lindman, editors. *Amphiphilic Block Copolymers: Self-Assembly and Applications*. Elsevier, 2000.

[AMKBK+11] J. Adelsberger, A. Meier-Koll, A. M. Bivigou-Koumba, P. Busch, O. Holderer, T. Hellweg, A. Laschewsky, P. Müller-Buschbaum, and C. M. Papadakis. *Colloid Polym. Sci.*, 289:711–720, 2011.

[bA98] D. ben Avraham. *Phys. Rev. Lett.*, 81:4756, 1998.

[BAR09] A. Blanazs, S. P. Armes, and A. J. Ryan. *Macromol. Rapid Commun.*, 30:267–277, 2009.

[BBE+90] F. J. Bermejo, F. Batallan, E. Enciso, R. White, A. J. Dianoux, and W. S. Howells. *J. Phys.: Condens. Matter*, 2:1301–1314, 1990.

[BCDLR+14] I. Bischofberger, D. C. E. Calzolari, P. De Los Rios, I. Jelezarov, and V. Trappe. *Scientific Reports*, 4:4377, 2014.

[BCT14] I. Bischofberger, D. C. E. Calzolari, and V. Trappe. *Soft Matter*, 10:8288, 2014.

[BDG+07] C. Balu, M. Delsant, P. Guenioun, P. Monti, and M. Cloitre. *Langmuir*, 23:2404–2407, 2007.

[Be8] M. Bee. *Quasielastic Neutron Scattering: Principles and Applications in Solid State Chemistry, Biology and Materials Science.* Adam Hilger, Bristol, England, 1988.

[BKGL+10] A. M. Bivigou-Koumba, E. Görnitz, A. Laschewsky, P. Müller-Buschbaum, and C. M. Papadakis. *Colloid Polym. Sci.*, 288:499–517, 2010.

[BLJP07] T. B. Bonné, K. Lüdtke, R. Jordan, and C. M. Papadakis. *Macromol. Chem. Phys.*, 208:1402–1408, 2007.

[BMS+12] S. Busch, H. Morhenn, G. G. Simeoni, W. Lohstroh, and T. Unruh. *Neutron Scattering: Experimental Manuals*, chapter TOFTOF - Time of flight spectrometer. Jülich Forschungszentrum GmbH, 2012.

[BMWH66] G. L. Bertrand, F. J. Millero, C. Wu, and L. Hepler. *J. Phys. Chem.*, 70:699–705, 1966.

[BO92] P. Bartlett and R. H. Ottewil. *J. Chem. Phys.*, 96:3306, 1992.

[BP76] B. J. Berne and R. Pecora. *Dynamic LIght Scattering.* John Willey & Sons, Inc., 1976.

[BP01] J. J. Brey and A. Prados. *Physical Review E*, 63:021108, 2001.

[Bro93] W. Brown, editor. *Dynamic Light Scattering.* Oxford Science Publications, 1993.

[BU11] P. Busch and T. Unruh. *J. Phys.: Condens. Matter*, 23:254205, 2011.

[Bur84] J. Burke. *The Book and Papaer Group Annual*, chapter Solubility Parameters: Theory and Application, pages 13–58. 1984.

[CCP07] E. Chiessi, F. Cavalieri, and G. Paradossi. *J. Phys. Chem. B*, 111:2820–2827, 2007.

[CF02] R. O. R. Costa and F. S. Freitas. *Polymer*, 43:5879–5885, 2002.

[CGT00] J. Chuang, A. Y. Grosberg, and T. Tanaka. *J. Chem. Phys.*, 112:6434–6442, 2000.

[Cro03] A new neutron imaging facility at bt-6 for the non-destructive analysis of the working fuel-cells. Internet, 2003.

[CSHG+10] M. A. Cohen Stuart, W. T. S. Huck, J. Genzer, M. Müller, C. Ober, M. Stamm, G. B:. Sukhorukov, I. Szleifer, V. V. Tsukruk, M. Urban, F. M. Winnik, S. Zauscher, I. Luzinov, and S. Minko. *Nat. Mater.*, 9:101–113, 2010.

[DC82] M. Daoud and J. P. Cotton. *Journal Physique*, 43:531, 1982.

[DCP+02] S. Dixit, J. Crain, W. C. K. Poon, J. L. Finney, and A. K. Soper. *Nature*, 416:829–832, 2002.

[DEE+85] Z. J. Derlacki, A. J. Easteal, V. J. Edge, L. A. Woolf, and Z. Roksandic. *J. Phys. Chem.*, 89:5318, 1985.

[DHF91] W. D. Dozier, J. S. Huang, and L. J. Fetters. *Macromolecules*, Dozier, W. D. and Huang, J. S. and Fetters, L. J.(24):2810, 1991.

[Dul72] L. Dullien. *Al. Ch. E.*, 18(1):62–70, 1972.

[DZK06] M. Das, H. Zhang, and E. Kumacheva. *Annu. Rev. Mater. Res.*, 36:117–142, 2006.

[FB98] S. Förster and C. Burger. *Macromolecules*, 31:879, 1998.

[Flo42] P. J. Flory. *J. Chem. Phys.*, 10:51, 1942.

[FNFBVdlN01] F. Fernandez-Nieves, A. Fernandez-Barbero, B. Vincent, and F. J. de las Nieves. *Langmuir*, 17:1841–1846, 2001.

[Fri12] H. Frielinghaus. *Scattering Methods for Condensed Matter Research: Towards Novel Applications at Future Sources*, volume 33, chapter Small Angle Scattering, page D1.2. Jülich Forschungszentrum GmbH, May 2012.

[FS87] L. A. Feigin and D. I. Svergun. *Structure Analysis by Small-Angle X-ray and Neutron Scattering*. New York: Plennum Press, 1987.

[FWL96] S. Förster, E. Wenz, and P. Lindner. *Phys. Rev. Lett.*, 77:95, 1996.

[GCT+10] S. V. Ghugare, E. Chiessi, M. T. F. Telling, A. Deriu, Y. Gerelli, J. Wuttke, and G. Paradossi. *J. Phys. Chem. B*, 114:10285–10293, 2010.

[GDCD97] A.V. Gorelov, A. Du Chesne, and K. A. Dawson. *Physica A*, 240:443 – 452, 1997.

[GDH72] K. T. Gillen, D. C. Douglass, and M. J. R. Hoch. *Journal of Chemical Physics*, 57(12):5117–5119, 1972.

[Ged01] U. W. Gedde. *Polymer Physics*. Kluwe Academic Publishers, 2001.

[GK82] O. Glatter and O. Kratky. *Small-Angle X-ray Scattering*. London: Academic Press, 1982.

[Gri] I. Grillo. https://www.ill.eu/?id=2821. online.

[Gri01] I. Grillo. Effect of instrumental resolution and polydispersity on ideal form factor in small angle neutron scattering. Ill technical report, Institut Laue Langevin, DS-LSS, 6 rue Jules Horowitz, B. P. 156, 38042 Grenoble Cedex 9, May 2001.

[Gri08] I. Grillo. *Soft-Matter Characterization*, chapter Small Angle Neutron Scattering and Application in Soft Condensed Matter, pages 707–759. Springer: Dordrecht, Netherlands, 2008.

[GRS79] A. Geiger, A. Rahman, and F. H. Stillinger. *J. Chem. Phys.*, 70(1):263, 1979.

[GSAK97] E. A. Galinski, M. Stein, B. Amendt, and M. Kinder. *Comp. Biochem. Physiol.*, 117A(3):357–365, 1997.

[GZ11] Y. Guan and Y. Zhang. *Soft Matter*, 7:6375–6384, 2011.

[Ham95] B. Hammouda. A tutorial on small-angle neutron scattering from polymers. online, National Institute of Standards and Technology, Materials Science and Engineering Laboratory, Gaithesburg, MD20899, June 1995.

[Ham07] I. W. Hamley. *Introduction to Soft Matter: Synthetic and Biological Self-Assembling Materials*. Wiley, 2007.

[Ham10] B. Hammouda. *J. Appl. Crystallogr.*, 43:716–719, 2010.

[HCB+10] J. Hao, H. Cheng, P. Butler, L. Zhang, and C. C. Han. *J. Chem. Phys.*, 132:154902, 2010.

[Hey14] M. Heyden. *J. Chem. Phys.*, 141:22D509, 2014.

[HG68] M Heskins and J Gillet. *J. Macromol. Sci., Part A: Pure Appl. Chem.*, 2(8):1441–1455, 1968.

[HHS00] M. Holz, S. R. Heil, and A. Sacco. *Phys. Chem. Chem. Phys.*, 2:4740–4742, 2000.

[Hir04] S. Hirotsu. *Macromolecules*, 37:3415–3424, 2004.

[HLLH04] M. R. Harpham, B. M. Ladanyi, N. E. Levinger, and K. W. Herwig. *J. Chem. Phys.*, 121:7855–7868, 2004.

[Hof87] A S Hoffman. *J. Controlled Release*, 6:297, 1987.

[Hof02] A. S. Hoffman. *Adv. Drug Delivery Rev.*, 43:3–12, 2002.

[HPS+12] C. H. Hofmann, F. A. Plamper, C. Scherzinger, S. Hietala, and W. Richtering. *Macromolecules*, 46:523–532, 2012.

[HRB14] M. K. Hazra, S. Roy, and B. Bagchi. *J. Chem. Phys.*, 141:18C501, 2014.

[HSW00] E. Hawlicka and D. Swiatla-Wojcik. *Phys. Chem. Chem. Phys.*, 2:3175–3180, 2000.

[HTW92] D. Hecht, L. Tadesse, and L. Walters. *J. Am. Chem. Soc.*, 114:4336–4339, 1992.

[Hug42] M. L. Huggins. *J. Phys. Chem.*, 46:151, 1942.

[HW80] K. R. Harris and L. A. Woolf. *J. C. S. Faraday I*, 76:377–385, 1980.

[IKK13] H. Inoue, S. Kuwahara, and K. Katayama. *Phys. Chem. Chem. Phys.*, 15:3814–3819, 2013.

[Isr94] J. N. Israelachvili. *Colloids Surf., A*, 91:1–8, 1994.

[Isr11] J. N. Israelachvili. *Intermolecular and Surface Forces*. Academic Press, Inc., 2011.

[Jac08] A. J. Jackson. Introduction to small-angle neutron scattering and neutron reflectometry. NIST Center for Neutron Research, May 2008.

[Jak88] J. Jakes. *Czech. J. Phys. B*, 38:1305–1316, 1988.

[JLS+11] M. J. N. Junk, W. Li, A. D. Schlütter, G. Wegner, H. W. Spiess, A. Zhang, and D. Hinderberger. *Journal of American Chemical Society*, 133:10832–10838, 2011.

[Jon24] J. E. Jones. *Proceedings of the Royal Society of London. Series A*, 106:441–462, 1924.

[Jon02] R. A. L. Jones. *Soft Condensed Matter*. Oxford University Press, 2002.

[KAA+14] K. Kyriakos, D. Aravopoulou, L. Augsbach, J. Sapper, S. Ottinger, C. Psylla, A. Aghebat Rafat, A. Benitez-Montoya, C. B. Miasnikova, Z. Di, A. Laschewsky, P. Müller-Buschbaum, and C. M. Papadakis. *Colloid Polym. Sci.*, 292:1757–1774, 2014.

[KATW06] P. Kujawa, AseyevAse., H. Tenhu, and F. M. Winnik. *Macromolecules*, 39:7686–7693, 2006.

[KKCR97] D.C. Kim, M.H. Kang, C.K. Choi, and J.Y. Ryu. *Journal of the Korean Physical Society*, 31:271–276, 1997.

[KMS82] J. T. Koberstein, B. Morra, and R. S. Stein. *J. Appl. Crystallogr.*, 13:34–45, 1982.

[KNM+05] H. Kogure, S. Nanami, Y. Masuda, Y. Toyama, and K. Kubota. *Colloid Polym. Sci.*, 283:1163, 2005.

[KPA+14] K. Kyriakos, M. Philipp, J. Adelsberger, S. Jaksch, A. V. Berezkin, D. M. Lugo, W. Richtering, I. Grillo, A. Miasnikova, A. Laschewsky, P. Müller-Buschbaum, and C. M. Papadakis. *Macromolecules*, 47:6867–6879, 2014.

[KT10] H. Kojima and F. Tanaka. *Macromolecules*, 43:5103–5113, 2010.

[KT12] H. Kojima and F. Tanaka. *Soft Matter*, 8:3010–3020, 2012.

[KTI+07] Y. Katsumoto, T. Tanaka, K. Ihara, M. Koyama, and Y. Ozaki. *J. Phys. Chem. B*, 111:12730, 2007.

[KU77] J. Kida and H. Uedaira. *J. Magn. Reson.*, 27:253–259, 1977.

[KVL90] N. Karger, T. Vardag, and H. Lüdemann. *J. Chem. Phys.*, 93(5):3437, 1990.

[LAM] Lamp, the large array manipulation program.

[LBS05] M. Liu, F. Bian, and F. Sheng. *Eur. Polym. J.*, 41:283–291, 2005.

[LC96] R. Lamanna and S. Cannistraro. *Chem. Phys.*, 213(1-3):95–110, 1996.

[LCH98] Y. Liu, S. H. Chen, and J. S. Huang. *Macromolecules*, 31:2236, 1998.

[LHL+10] X. Li, K. Hong, Y. Liu, C. Y. Shew, E. Liu, K. W. Herwig, G. S. Smith, J. Zhao, G. Zhang, S. Pispas, and W. R. Chen. *J. Chem. Phys.*, 133:144912, 2010.

[LHS+12] R. Luxenhofer, Y. Han, A. Schulz, J. Tong, Z. He, A. V. Kabanov, and R. Jordan. *Macromol. Rapid Commun.*, 33:1613–1631, 2012.

[LKS97] A. Laaksonen, P. G. Kusalik, and I. M. Svishchev. *Journal of Physical Chemistry*, 101(33):5910–5918, 1997.

[LLW+89] M.Y. Lin, H.M. Lindsay, D.A. Weitz, R.C. Ball, and R. Klein. *Nature*, 339:360–362, 1989.

[LSS+13] J. G. J. L. Lebouille, R. Stepanyan, J. J. M. Slot, M. A. Cohen Stuart, and R. Tuinier. *Colloids Surf., A*, 2013.

[Map00] R. E. Maples. *Petroleum Refinery Process Economics*. Pennwell Corp., May 2000.

[MBC+10] F. Mallamace, C. Branca, C. Corsaro, N. Leone, J. Spooren, E. H. Stanley, and S. H. Chen. *Journal of Physical Chemistry B*, 114:1870–1878, 2010.

[MC70] J. S. Murday and R. M. Cotts. *J. Chem. Phys.*, 53:4724, 1970.

[MEW74] D. Magde, E. L. Elson, and W. W. Webb. *Biopolymers*, 13:29–61, 1974.

[MFEM04] M. Miyazaki, A. Fujii, T. Ebata, and N. Mikami. *Science*, 304:1134–1137, 2004.

[MHI00] Y. Maeda, T. Higuchi, and I. Ikeda. *Langmuir*, 16:7503–7509, 2000.

[MHRR10] S. T. Moin, T. S. Hofer, B. R. Randolf, and B. M. Rode. *J. Comput. Chem.*, 32(5):886–892, 2010.

[Mil73] R. Mills. *J. Phys. Chem.*, 77(5):5–8, 1973.

[MK61] S. Z. Mikhail and W. R. Kimel. *Journal of Chemical Engineering Data*, 6:533–537, 1961.

[MKPB+12] A. Meier-Koll, V. Pipich, P. Busch, C. M. Papadakis, and P. Müller-Buschbaum. *Langmuir*, 28:8791–8798, 2012.

[ML12] A. Miasnikova and A. Laschewsky. *J. Polym. Sci., Part A: Polym. Chem.*, 50:3133–3323, 2012.

[MLDP+12] A. Miasnikova, A. Laschewsky, G. De Paoli, C. M. Papadakis, P. Müller-Buschbaum, and S. S. Funari. *Langmuir*, 28:4479–4490, 2012.

[MM14] R. D. Martin and D. V. Matyushov. *J. Chem. Phys.*, 141:22D501, 2014.

[MNDLR04] S. Moelbert, B. Normand, and P. De Los Rios. *Biophys. Chem.*, 112:45–57, 2004.

[MT88] E. S. Matsuo and T. Tanaka. *J. Chem. Phys.*, 89:1695–1703, 1988.

[MTV+96] N. Micali, S. Trusso, C. Vasi, D. Blaudez, and F. Mallamace. *Phys. Rev. E: Stat., Nonlinear, Soft Matter Phys.*, 54(2):1720–1724, 1996.

[NC02] N. Nath and A. Chilkoti. *Adv. Mater. (Weinheim, Ger.)*, 14(17):1243–1247, 2002.

[NMYM09] M. Nakada, K. Maruyama, O. Yamamuro, and M. Misawa. *J. Chem. Phys.*, 130:074503, 2009.

[NNH+07] A Nykänen, M Nuopponen, S P Hirvonen, M Rytelä, H Turunen, O amd Tenhu, R Mezzenga, O Ikkala, and J Ruokolainen. *Macromolecules*, 40:5827–5834, 2007.

[nob] The nobel prize in physics 1994. Web.

[NOM+06] M. Nakayama, T. Okano, T. Miyazaki, F. Kohori, K. Sakai, and M. Yokoyama. *J. Controlled Release*, 115(1):46–56, 2006.

[OP71] D. E. O'Reily and E. M. Peterson. *J. Chem. Phys.*, 55:2155, 1971.

[Orw77] R. A. Orwoll. *Rubber Chem. Technol.*, 50:451, 1977.

[OSKY09] N. Osaka, M. Shibayama, T. Kikuchi, and O. Yamamuro. *J. Phys. Chem. B*, 113:12870–12876, 2009.

[OT05] Y. Okada and F. Tanaka. *Macromolecules*, 38:4465–4471, 2005.

[OWT01] F. M. Ottaviani, S. H. Winnik, F. M.and Bosmann, and N. J. Turro. *Helv. Chim. Acta*, 84:2476–2492, 2001.

[OZ14] L. S. Ornstein and F. Zernicke. *Proc. Sect. Sci. K. Med. Akad. Wet.*, 17:793, 1914.

[PG12] T. A. Pascal and W. Goddard. *Journal of Physical Chemistry B*, 116(47):13905–12, 2012.

[PIA99] W. S. Price, H. Ide, and Y. Arata. *J. Phys. Chem. A*, 103:448–450, 1999.

[PIA03] W. S. Price, H. Ide, and Y. Arata. *J. Phys. Chem. A*, 107:4784–4789, 2003.

[PKRW14] C. M. Papadakis, P. Kosovan, W. Richtering, and D. Wöll. *Colloid Polym. Sci.*, 292(10):2399–2411, 2014.

[PKS+14] M. Philipp, K. Kyriakos, L. Silvi, W. Lohstroh, W. Petry, J. K. Krüger, C. M. Papadakis, and P. Müller-Buschbaum. *J. Phys. Chem.*, 118(15):4253–4260, 2014.

[PM13] D. D. Purkayastha and V. Madhurima. *J. Mol. Liq.*, 187:54–57, 2013.

[PMA+12] M Philipp, U Müller, R Aleksandrova, R. Sanctuary, P Müller-Buschbaum, and J K Krüger. *Soft Matter*, 8:11387–11395, 2012.

[PMJR+13] M Philipp, U Müller, R J Jimenez Rioboom, P Müller-Buschbaum, and J K Krüger. *Soft Matter*, 9:9887–9896, 2013.

[Por51] G. Porod. *Kolloid-Zeitschrift*, 124:83–114, 1951.

[PPM90] J.S. Pedersen, D. Posselt, and K. Mortensen. *J. Appl. Crystallogr.*, 23:321–333, 1990.

[PPM92] D. Posselt, J. S. Pedersen, and K. Mortensen. *J. Non-Cryst. Solids*, 145:128–132, 1992.

[PW77] K. Pratt and W. Wakeham. *J. Chem. Soc., Faraday Tras.*, 73:997–1002, 1977.

[Pyn90] R. Pynn. Chapter 2: Neutron scattering - a non destructive microscope for seeing inside matter. *Los Alamos Science*, 19:1–31, 1990.

[QSH11] J. Qvist, H. Schober, and B. Halle. *J. Chem. Phys.*, 134:1–20, 2011.

[RBS13] D. Roy, W. L. A. Brooks, and B. S. Sumerlin. *Chem. Soc. Rev.*, 47:7214–7243, 2013.

[RC03] M. Rubinstein and R. H. Colby. *Polymer Physics*. Oxford University Press, 2003.

[RSS01] W. B. Russel, D. Saville, and W. R. Schowalter. *Colloidal Dispersions*. Cambridge University Press, England, 2001.

[Rul71] W. Ruland. *J. Appl. Crystallogr.*, 4:70–73, 1971.

[Sam69] T. Sampson. *J. Chem. Phys.*, 51(12):5543, 1969.

[SBGU08] C. Smuda, S. Busch, G. Gemmecker, and T. Unruh. *Journal of Chemical Physics*, 129:014513, 2008.

[Sch82] P. W. Schmidt. *J. Appl. Crystallogr.*, 15:567–569, 1982.

[Sch92] H. G. Schild. *Prog. Polym. Sci.*, 17:163–249, 1992.

[Sch07] W. Schärtl. *Light Scattering from Polymer Solutions and Nanoparticle Dispersions*. Springer-Verlag, 2007.

[Sea92] V. F. Sears. *Neutron News*, 3(3):26–37, 1992.

[SF93] A. K. Soper and J. L. Finney. *Phys. Rev. Lett.*, 71(26):4346–4349, 1993.

[SHRR12] C. Scherzinger, O. Holderer, D. Richter, and W. Richtering. *Journal of Physical Chemistry Chemical Physics*, 14:2762–2768, 2012.

[SJC14] S. K. Sinha, M. Jana, and K. Chakraborty. *J. Chem. Phys.*, 141:22D502, 2014.

[SKZ+14] D. Schaeffel, A. Kreyes, Y. Zhao, K. Landfester, H. J. Butt, D. Crespy, and K. Koyonov. *ACS Macro Letters*, 3:428–432, 2014.

[SL] G. G. Simeoni and W. Lohstroh. http://www.mlz-garching.de/toftof. online.

[SLKR10] C. Scherzinger, P. Lindner, M. Keerl, and W. Richtering. *Macromolecules*, 43:6829–6833, 2010.

[SLS+12] R. Stepanyan, J. G. J. L. Lebouille, J. J. M. Slot, R. Tuinier, and M. A. Cohen Stuart. *Phys. Rev. Lett.*, 109:138301, 2012.

[SMT91] H. G. Schild, M. Muthukumar, and D. A. Tirell. *Macromolecules*, 24:948–952, 1991.

[Sol98] P. Sollich. *Phys. Rev. E: Stat., Nonlinear, Soft Matter Phys.*, 58(1):739–758, 1998.

[Sor11] C.M. Sorensen. *Aerosol Sci. Technol.*, 45(7):755–769, 2011.

[SRPL04] M. Stieger, W. Richtering, J. S. Pedersen, and P. Lindner. *J. Chem. Phys.*, 120:6197, 2004.

[SSB+14] C. Scherzinger, A. Schwarz, A. Bardow, K. Leonhard, and W. Richtering. *Current Opinion in Colloid & Interface Science*, 19:84–94, 2014.

[SSSI74] W. Schmatz, T. Springer, J. Schelten, and K. Ibel. *J. Appl. Crystallogr.*, 7:96–116, 1974.

[Sti80] F. H. Stillinger. *Science*, 209:4455, 1980.

[SW10] S. Sun and P. Wu. *Macromolecules*, 43:9501–9510, 2010.

[SYAM98] N. Shinyashiki, S. Yagihara, I. Arita, and S. Mashimo. *J. Phys. Chem. B*, 102:3249, 1998.

[TdlHAC+04] B. R. Twaites, C. de las Heras Alarcon, D. Cunliffe, M. Lavigne, S. Pennadam, J. R. Smith, D. C. Gorecki, and C. Alexander. *J. Controlled Release*, 97:551–566, 2004.

[TKKW11] F. Tanaka, T. Koga, I. Kaneda, and F. M. Winnik. *J. Phys.: Condens. Matter*, 23:284105, 2011.

[TKW08a] F. Tanaka, T. Koga, and F. M. Winnik. *Phys. Rev. Lett.*, 101:028302, 2008.

[TKW+08b] K. Troll, A. Kulkarni, W. Wang, C. Darko, A. M. Bivigou-Koumba, A. Laschewsky, P. Müller-Buschbaum, and C. M. Papadakis. *Colloid Polym. Sci.*, 286:1079–1092, 2008.

[TKXW11] F. Tanaka, H. Koga, T.and Kojima, N. Xue, and F. M. Winnik. *Macromolecules*, 44:2978–2989, 2011.

[TKY+06] Y Tsuda, A Kikuchi, M Yamato, G Chen, and T Okano. *Biochem. Biophys. Res. Commun.*, 348, 2006.

[UNP07] T. Unruh, J. Neuhaus, and W. Petry. *Nucl. Instrum. Methods Phys. Res., Sect. A*, 580:1414–1422, 2007.

[WÏ4] D. Wöll. *RSC Adv.*, 4:2447, 2014.

[WCR88] G. D. Wignall, D. K. Christen, and V. Ramakrishnan. *J. Appl. Crystallogr.*, 21:438–451, 1988.

[WHLS84] D.A. Weitz, J.S. Huang, M.Y. Lin, and J. Sung. *Phys. Rev. Lett.*, 53:1657–1660, 1984.

[WLZ04] C. Wu, W. Li, and X. X. Zhu. *Macromolecules*, 37:4989–4992, 2004.

[WOB+92] F. M. Winnik, F. M. Ottaviani, S. H. Bossmann, Garcia-Garibay M., and N. J. Turro. *Macromolecules*, 25:6007, 1992.

[Woo85] L. A. Woolf. *Pure Appl. Chem.*, 57(8):1083–1090, 1985.

[WQW98] X. Wang, X. Qiu, and C. Wu. *Macromolecules*, 31:2972–2976, 1998.

[WRV90] F. M. Winnik, H. Ringsdorf, and J. Venzmer. *Macromolecules*, 23:2415–2416, 1990.

[WSL+12] F. Wang, Y. Shi, S. Luo, Y. Chen, and J. Zhao. *Macromolecules*, 45:9196–9204, 2012.

[Wut12] J. Wuttke. *Scattering Methods for Condensed Matter Research: Towards Novel Applications at Future Sources*, chapter Quasielastic Scattering, page D7. Jülich Forschungszentrum GmbH, 2012.

[WZ95] C. Wu and S. Zhou. *Macromolecules*, 28:8381–8387, 1995.

[YAE94] H. Yamakawa, F. Abe, and Y. Einaga. *Macromolecules*, 27:5704, 1994.

[YLS+07] X. Ye, Y. Lu, L. Shen, Y. Ding, S. Liu, G. Zhang, and C. Wu. *Macromolecules*, 40:4750–4752, 2007.

[YV98] R. H. Yoon and S. Vivek. *J. Colloid Interface Sci.*, 204:179–186, 1998.

[ZAN+13] Q. Zhong, J. Adelsberger, M. A. Niedermeir, A. Golosova, A. M. Bivigou-Koumba, A. Laschewsky, S. S. Funari, C. M. Papadakis, and P. Müller-Buschbaum. *Colloid Polym. Sci.*, 291:1439–1451, 2013.

[ZCB13] A. Zaccone, J.J. Crassous, and M. Ballauff. *J. Chem. Phys.*, 138:104908, 2013.

[ZCBB11] A. Zaccone, J.J. Crassous, B. Beri, and M. Ballauff. *Phys. Rev. Lett.*, 107:168303, 2011.

[ZMR+13] Q. Zhong, E. Metwalli, M. Rawolle, G. Kaune, A. M. Bivigou-Koumba, A. Laschewsky, C. M. Papadakis, R. Cubitt, and P. Müller-Buschbaum. *Macromolecules*, 46:4069–4080, 2013.

[Zor12] R. Zorn. *Scattering Methods for Condensed Matter Research: Towards Novel Applications at Future Sources*, volume 33, chapter Correlation Functions Measured by Scattering Experiments, page A5. Jülich Forschungszentrum GmbH, 2012.

[ZT12] A. Zaccone and E. M. Terentjev. *Phys. Rev. Lett.*, 108:038302, 2012.

[ZW01] G. Zhang and C. Wu. *Journal of American Chemical Society*, 123:1376–1380, 2001.

List of publications

Publications related to the subject of the dissertation

- K. Kyriakos, M. Philipp, C. H. Lin, M. Dyakonova, N. Vishnevetskaya, I. Grillo, A. Zaccone, A. Miasnikova, A. Laschewsky, P. Müller-Buschbaum, C. M. Papadakis "Quantifying cononsolvent-mediated interactions in the aggregation of themoresponsive polymers", *submitted*
- K. Kyriakos, M. Philipp, J. Adelsberger, S. Jaksch, A. V. Berezkin, D. M. Lugo, W. Richtering, I. Grillo, A. Miasnikova, A. Laschewsky, P. Müller-Buschbaum, C. M. Papadakis "Cononsolvency of Water/Methanol Mixtures for PNIPAM and PS-*b*-PNIPAM: Pathway of Aggregate Formation Investigated Using Time-Resolved SANS", *Macromolecules*, vol. 47, pp. 6867-6879, 2014
- K. Kyriakos, D. Aravopoulou, L. Augsbach, J. Sapper, S. Ottinger, C. Psylla, A. Aghebat Rafat, C. A. Benitez Montoya, A. Miasnikova, Z. Di, A. Laschewsky, P. Müller-Buschbaum, C. M. Papadakis "Novel thermoresponsive block copolymers having different architectures - structural, rheological, thermal and dielectric investigations", *Colloid and Polymer Science*, vol. 292, pp. 1757-1774, 2014
- M. Philipp, K. Kyriakos, L. Silvi, W. Lohstroh, W. Petry, J. K. Krüger, C. M. Papadakis, P. Müller-Buschbaum "From Molecular Dehydration to Excess Volumes of Phase-Separating PNIPAM solutions", *Journal of Physical Chemistry B*, vol. 118, issue 15, pp. 4253-4260, 2014

Further publications

- K. Raftopoulos, S. Koutsoumpis, J. Malgorzata, J. Lewicki, K. Kyriakos, H. Mason, S. Harley, E. Hebda, C. M. Papadakis, K. Pielichowski, P. Pissis "Reduced phase separation, and slowing down of dynamics in polyurethanes with 3-dimensional POSS based crosslinking moieties", *under revision*

A. Eisele, K. Kyriakos, R. Bhandary, M. Schönhoff, C. M. Papadakis, B. Rieger "Structure and ionic conductivity of liquid crystals having propylene carbonate units", *Journal of Materials Chemistry A*, *accepted*, 2014 (doi: 10.1039/C4TA05401F)

- M. A. Dyakonova, N. Stavrouli, M. T. Popescu, K. Kyriakos, I. Grillo, M. Philipp, S. Jaksch, C. Tsitsilianis, C. M. Papadakis "Physical Hydrogels via Charge Driven Self-Organization of a Triblock Polyampholyte - Rheological and Structural Investigations", *Macromolecules*, vol. 47, issue 21, pp. 7561-7572, 2014
- J. Zhang, D. Posselt, D.-M. Smilgies, J. Perlich, K. Kyriakos, S. Jaksch, C. M Papadakis, "Lamellar Diblock Copolymer Thin Films during Solvent Vapor Annealing Studied by GISAXS: Different Behavior of Parallel and Perpendicular Lamellae", *Macromolecules*, vol. 47, issue 16, pp. 5711-5718, 2014
- J. Zhang, D. Posselt, D.-M. Smilgies, J. Perlich, K. Kyriakos, S. Jaksch, C. M Papadakis,"Complex macrophase-separated nanostructure induced by microphase separation in binary blends of lamellar diblock copolymer thin films", *Macromolecular Rapid Communications*, vol. 35, issue 18, pp. 1622-1629
- S. Jaksch, A. Schulz, K. Kyriakos, J. Zhang, I. Grillo, V. Pipich, R. Jordan, C. M. Papadakis "The collapse and aggregation of thermoresponsive poly(2-oxazoline) gradient copolymers: a time-resolved SANS study", *Colloid and Polymer Science*,vol. 292, issue 10, pp. 2413-2425, 2014

Conference talks

- K. Kyriakos, M. Philipp, C. H. Lin, M. Dyakonova, N. Vishnevetskaya, I. Grillo, A. Miasnikova, A. Laschewsky, P. Müller-Buschbaum, C. M. Papadakis, "Cononsolvency in P(S-*b*-NIPAM) in different solvent mixtures – a time-resolved SANS investigation", *8th International Symposium "Molecular Order and Mobility in Polymer Systems"*, St. Petersburg, Russia, 2-6 June 2014
- K. Kyriakos, M. Philipp, J. Adelsberger, S. Jaksch, I. Grillo, A. Miasnikova, A. Laschewsky, P. Müller-Buschbaum, C. M. Papadakis, "Cononsolvency in P(S-*b*-NIPAM) diblock copolymers- A time-resolved SANS study", *Third International Workshop SKIN 2014 Studying Kinetics with Neutrons*, Grenoble, France, 24-27 March 2014
- K. Kyriakos, M. Philipp, J. Adelsberger, S. Jaksch, I. Grillo, A. Miasnikova, A. Laschewsky, P. Müller-Buschbaum, C. M. Papadakis, "Cononsolvency in P(S-*b*-NIPAM) diblock copolymers- A time-resolved SANS study of the aggregation process", *DFG Frühjahrstagung*, Dresden, Germany, 30 Februar -4 April 2014

- K. Kyriakos, M. Philipp, J. Adelsberger, S. Jaksch, I. Grillo, A. Miasnikova, A. Laschewsky, P. Müller-Buschbaum, C. M. Papadakis, "Cononsolvency in P(S-*b*-NIPAM) diblock copolymers in aqueous solutions", *6th biannual science meeting of TUM (MLZ, E13, E21), HZG and JCNS*, Grainau, Germany, 10-13 June 2013
- K. Kyriakos, M. Philipp, J. Adelsberger, S. Jaksch, I. Grillo, A. Miasnikova, A. Laschewsky, P. Müller-Buschbaum, C. M. Papadakis, "Cononsolvency in P(S-*b*-NIPAM) diblock copolymers in aqueous solutions", *European Polymer Congress EPF 2013*, Pisa, Italy, 16-21 June 2013
- K. Kyriakos, S. Ottinger, C. Psylla, A. Miasnikova, A. Laschewsky, P. Müller-Buschbaum, C. M. Papadakis, "Novel thermoresponsive polymers in various architectures", *Fluorescence correlation spectroscopy in polymer science*, Munich, Germany, 10-11 October 2013

Conference poster presentations

- K. Kyriakos, S. Ottinger, C. Psylla, A. Miasnikova, A. Laschewsky, P. Müller-Buschbaum, C. M. Papadakis, "Novel thermoresponsive block copolymers of various architectures - a fluorescence correlation spectroscopy investigation of the micelle formation", *DFG Frühjahrstagung*, Dresden, Germany, 30 Feb - 4 April 2014
- K. Kyriakos, S. Ottinger, C. Psylla, A. Miasnikova, A. Laschewsky, P. Müller-Buschbaum, C. M. Papadakis, "Novel thermoresponsive polymers in various architectures", *DFG Frühjahrstagung*, Regensburg, Germany, 10-15 March 2014
- K. Kyriakos, M. Philipp, J. Adelsberger, S. Jaksch, I. Grillo, A. Miasnikova, A. Laschewsky, P. Müller-Buschbaum, C. M. Papadakis, "Cononsolvency of PNIPAM in water/methanol mixed solutions", *DFG Frühjahrstagung*, Regensburg, Germany, 10-15 March 2014
- K. Kyriakos, M. Philipp, J. Adelsberger, S. Jaksch, I. Grillo, A. Miasnikova, A. Laschewsky, P. Müller-Buschbaum, C. M. Papadakis, "Cononsolvency in aqueous solutions of P(S-*b*-NIPAM) diblock copolymers", *JCNS workshop 2012 'Trends and Perspectives in Neutron Scattering for Soft Matter and Biophysics'*, Tutzing, Germany, 8-11 October 2012
- K. Kyriakos, M. Philipp, J. Adelsberger, S. Jaksch, I. Grillo, A. Miasnikova, A. Laschewsky, P. Müller-Buschbaum, C. M. Papadakis, "Cononsolvency in aqueous solutions of P(S-*b*-NIPAM) diblock copolymers", *DFG Frühjahrstagung*, Berlin, Germany, 8-11 October 2012

Acknowledgments

The realization of this work would be impossible without the help, contribution and support of several people.

First of all, I would like to express my gratitude to Prof. Christine M. Papadakis, who gave me three and a half years ago the opportunity to undertake my doctoral studies in her group with such an interesting and challenging topic. Throughout this time she supported me, mentally and scientifically, and helped me to become a better scientist, as well as a better person. Her guidance was always vital for the evolution of the project and helped me a lot to regain focus at crucial crossroads of my work.

Furthermore, I want to thank Dr. Martine Philipp, with whom I had the invaluable opportunity to collaborate during our common project. The several chances that I had to discuss with her on many subjects, both project- and science-related, helped me a lot to understand better the essence of science. Her deep understanding of polymer physics contributed vastly in my attempts to enrich my knowledges.

Also I would like to thank Prof. Peter Müller-Buschbaum. The discussions that we shared, within the framework of our common projects, were very helpful and educational for me.

Special thanks must go to all the students that I collaborated with, either during their M.Sc. and B.Sc. theses or during their work in our chair. Lukas Augsbach, Sarah Ottinger, Kora-Lee Claude, Ali Aghebat Rafat, Christina Psylla, Che-Hung Lin thank you for your contribution to my work.

All members of the Soft Matter Physics Group, current and former, should also take their share of my gratitude: Dr. Joseph Adelsberger, Dr. Alessandro Seppe, Dr. Tillo Hoppe, Dr. Sebastian Jaksch, Dr. Jianqi Zhang, Margarita Dyakonova, Natalya Vishnevetskaya, Dr. Anatoly Berezkin, Dr. Kostas Raftopoulos thank you very much for the very nice working environment and for the beautiful moments.

In addition, I would like to thank all the other members of the Chair of Functional Materials for the productive working environment and the nice collaboration and daily communication.

An important part of this work was based on materials synthesized in the University of Potsdam. Therefore I would like thank Dr. Anna Miasnikova and Prof. André Laschewsky for their efforts on preparing such interesting and high quality polymers, as well as for the very fruitful collaboration in general.

I would like to acknowledge also the important contribution of all the beamline scientists and their work, without which it would be impossible to conduct the experimental part of this project. Namely, Dr. Isabelle Grillo from the D22 SANS instrument (ILL, Grenoble, France), Dr. Wiebke Lostroh and Luca Silvi from the TOFTOF direct spectrometer (MLZ, Garching), Dr. Zhenyu Di from the KWS-2 SANS instrument (MLZ, Garching), Dr. Olaf Holderer and Dr. Oxana Ivanova from the J-NSE instrument (MLZ, Garching).

Moreover the collaboration with several people from various groups, within common projects and fruitful discussions, helped me a lot to evolve the level of my work. Hence, I would like to thank Dr. Dersy M. Lugo and Prof. Walter Richtering (Lehrstuhl für Physikalische Chemie II, Institut für Physikalische Chemie, RWTH Aachen University), Prof. Martin Zacharias (Lehrstuhl für Theoretische Biophysik - Molekulardynamik, TUM) and Prof. Alessio Zaccone (Theory of Soft Matter, TUM). Special thanks I would like to say to all the members of the Dielectrics Group of NTUA and especially to Prof. Polykarpos Pissis, Prof. Apostolos Kyritsis, Dionysia Aravopoulou and Katerina Bikas for the very productive collaboration and the inspiring discussions.

A special gratitude I would like to express to the secretaries of our group, Susanna Fink and Marion Waletzki. They managed to make my everyday life much easier and helped a lot to stand against many bureaucratic challenges.

The financial support of this project from the DFG, within the framework of the SPP 1259 "Intelligent Hydrogels" (Pa771/4, Mu487/8 and La611/7), is also gratefully acknowledged.

My family was always the constant support and the solid basis on which I managed to build everything that I accomplished during my work. A simple "thank you" is to small to reveal the gratitude that I own to both my parents and my sister.

Above all I would like to thank Giouli, the person that stood by me, even in the most difficult and darkest times, without losing her faith to me not even for a moment. Without your support I could not succeed in my efforts. Σε ευχαριστώ για όλα.